Large-Scale Structure and Dissipation

Stage du D.E.A. d'Astrophysique et Techniques Spatiales
de l'Observatoire de Meudon,
Section d'Astrophysique de l'Observatoire de Paris
Directeur du stage:
Prof. Dr. Vincent Icke
Sterrewacht Leiden

Bernd MŰLLER-BIERL

Avril – June, 1993
2nd corrected edition

Preface

This work has been done as a colaborative student research project between the Observatory of Meudon, Astrophysical Department of the Observatory of Paris and the Observatory of Leiden. The work takes part of the astrophysical formation completed by the D.E.A. (Diplôme d'Études d'Astrophysique et Techniques Spatiales) of the Observatory of Meudon. The work has been done under the direction of Prof. Dr. Vincent Icke. I want to thank Vincent Icke for that I could do this work at and with him. I acknowledege the Leiden Observatory for I could use the computer fascillity. Finally, I want to thank Mme. Rocca-Volmerange for that I could do this stage at Leiden. I'm deeply indepted to my teachers in Paris, Freiburg and Konstanz.

Leiden, 1.7.1993
Bernd Műller-Bierl

Preface

Ce travail était fait comme projét de recherche collaborative entre l'observatoire de Meudon, département d'Astrophysique de l'observatoire de Paris et l'observatoire de Leiden. Le tavail fait partie de la formation pour l'Atrophysique, completé par le D.E.A. (Diplôme d'Études d'Astrophysique et Techniques Spatiales) de l'observatoire de Meudon. Ce travail était fait sous la direction de Monsieur le professeur, Vincent ICKE. Je voudrais remercier Vincent ICKE pour que j'ai pu faire ce travail chez et avec lui. Je reconnaisse l'observatoire de Leiden pour que j'ai pu utiliser son équipement des ordinateurs. Finalement, je voudrais remercier Mme. ROCCA-VOLMERANGE pour que j'ai pu faire ce stage à Leiden. Je suis obligé de remercier mes professeurs à Paris, Fribourg et Constance.

Leiden, 1.7.1993
Bernd MŰLLER-BIERL

Präambel

Diese Arbeit wurde als gemeindschaftliches Studentenforschungsprojekt zwischen der Sternwarte von Meudon, Astrophysikalische Abteilung der Sternwarte von Paris und der Sternwarte von Leiden durchgeführt. Die Arbeit hat Teil an der astrophysikalischen Ausbildung der Sternwarte von Meudon, welche durch das D.E.A. (Diplôme d'Études d'Astrophysique et Techniques Spatiales) abgeschlossen wird. Die Arbeit wurde unter der Leitung von Prof. Dr. Vincent Icke durchgeführt. Ich möchte Vincent Icke danken, daß ich diese Arbeit bei und mit Ihm habe machen können. Ich danke der Sternwarte von Leiden, für die Benutzung der Rechenanlage. Schließlich möchte ich Mme. Rocca-Volmerange danken, die mir ermöglichte, dieses Praktikum in Leiden zu machen. Ich danke insbesonders meinen Lehrern in Paris, Freiburg und Konstanz.

Leiden, 1.7.1993
Bernd Müller-Bierl

Contents

Chapter 1

Introduction

Ths work concerns a study of the difference between the large scale structure of the Universe and the properties of structures on smaller scales, down to the size of galaxies. Whereas large scale structure is totally unrelaxed, structure on smaller scales appears to be virialized. In the case of the Abell clusters, this can be understood as a consequence of gravitational effects. It has been shown that e.g. the cluster-cluster correlation function can be reproduced with a model based on pressure-free selfgravity [Wey89]. Bigger and smaller scales have not yet been encompassed by a single cosmogenesis.

The problem treated here was to see whether dissipative processes may provide an entrance. To do so, the effect of dynamical friction in an N-body model has been studied. Therefore the structures have been separated into four different topological features (voids, walls, filaments and nodes) with different geometric dilutions (r^0 for walls, r^{-1} for filaments and r^{-2} for nodes). Due to these geometrical effects, dissipative phenomena were found to be different in the three cases. One may suppose that these differences are due to the properties of the dark matter. Different core-sizes and internal velocity dispersions of galaxies were taken as parameters for dynamical friction. They could correspond e.g. to different halo sizes of brown dwarfs which are optically too red to have been remarked until now [1]

The work consists of the study of three dimensional self-gravitating motion of model galaxies with varying degrees of 'stickiness' in a background potential corresponding to each one of the three different geometric dilutions. To do so, pressure-free selfgravity was considered as a reasonable approximation for cosmic structure formation on a 100 Mpc scale.

The protogalactic clouds in the former Universe are assumed to behave like a stacking of expanding underdense regions as it follows from the "Bubble Theorem". Therefrom a mass distribution with the topological different constituents wall, filament and node evolves. We assumed for this work that galaxies form early, so dissipation can be due to dynamical friction between whole galaxies. An

[1] Maybe in the near future some light will be shed on this: It is planned within the Infrared Space Observatory to measure the accumulated radiation of a galactic halo of brown dwarfs [Lac90].

N-body code, suitable to investigate the flow of model-galaxies in different background potentials in a cubic structure with periodical boundary conditions has been developed and is described in the Appendix. The equations of motion have been solved by a differential equation solver algorithm of type Bulirsch-Stoer (cf. Press et al. [Pre86]). The selfgravity of the particles has been evaluated using a simple direct summation scheme. The results of the computations have been analyzed in phase-space in time and, to separate out numerical effects due to the N-body algorithm used, the energy and momentum behaviour of the particles has been investigated.

For different parameters of dissipation, the throughput of dissipation on the velocity distribution of the particles has been investigated.

The results of these computations may serve as input for one- dimensional calculations on the CMBR constraints obtained from the satellite COBE.

Chapter 2

Voids, Walls, Filaments and Nodes in the Universe

2.1 Brief Historical Intoduction

In the 18th. century, J.H. Lambert founded a hierarchic world model where systems of lower order are connected to higher order systems ad infinitum. We know today that there is a hierarchy in the Universe: Systems of first order are the planets and satellites, systems of second order are planets and stars, systems of 3rd order are the star clusters, those of 4th order are the galaxies. Systems of 5th order are the clusters of galaxies and systems of 6th order are the clusters of clusters of galaxies: the superclusters.

Whereas it appeared 20 years ago not yet as certain whether superclusters exist, today we know that they do. A review on superclusters and observational properties on large scale structure was written by Oort 1983 [Oor83]. For the aim of this work is to elucidate properties of large scale structure, we first recall the observational evidence for it.

More recently, a review [Bah88] has been written about the large-scale structure in the universe indicated by galaxy clusters. Whereas earlier observations gave evidence for galaxies to cluster on scales $\ll 20\ h^{-1}$ Mpc ($H_0 = h\,100\mathrm{kms}^{-1}\mathrm{Mpc}^{-1}$) whereas the universe on a larger scale ($\gg 20\ h^{-1}$ Mpc) seemed randomly distributed, observational evidence for structure on scales ~ 100 Mpc has been found. This large-scale structure is yet totally unrelaxed; It is taken to be a good tracer of the process of galaxy formation. Clusters on the scale $100\ h^{-1}$ Mpc are refered to as superclusters of clusters.

From galaxy redshift surveys, a netlike or "spongy" structure and voids to scales of $\sim 100\ h^{-1}$ Mpc have been revealed. Voids on these scales are reviewed by Rood [Roo88].

2.2 Different Topological Entities

The approach tried by this work is founded on the classification of the large-scale structure into geometric different entities, namely in voids, walls, filaments and nodes. The largest wall detected has a minimum extent of 60 h^{-1} Mpc $\times$ 170 h^{-1} Mpc [Gel89]. Filament structure has been found within the CfA redshift surveys (cf. e.g. [Huc83]) to be real while using a filament finding algorithm (minimal spanning tree) by Bhavsar et al. [Bha88].

Using a model for pressure-free selfgravitating formation of large-scale structure, the rich Abell clusters [Abe58] could be identified to be the nodes in an expanding cell-like structure [Wey89]. For a review on this so-called *Voronoi*-model [1] see Icke et al. [Ick91]. This model canonical implies the topological different structures walls, filaments and nodes. It is based on a theorem that states that the formation of structure on large scales can be understood from empty regions in space expanding pressure-free selfgravitating and thereby becoming more and more spherical ("Bubble-Theorem", Icke (1983)).

The Voronoi model allows to predict mass flow between the topological different ingredients wall, filament and node (cf. [Ick91b]). For the different geometric dilutions (r^0 for walls, r^{-1} for filaments and r^{-2} for nodes) can be characterisized in one dimension, the model is especially suitable for studying the formation of large scale structure in one dimension. This means that one can study with much higher precision than is possible with 3D N-body or gas-flow models, since the number of particles N needed to fill a 3D volume of size L increases with L^3, whereas the Poisson error due to statistical fluctuations decreases only with $\sqrt[3]{N}$. Finally this could permit to verify constraints on the CMBR found by COBE [Ben92] while studying different scenarios (in particular the 'explosion'-scenario [Ost88], the 'adhesion'-scenario [Sha89] or the pressure-free selfgravitating scenario [Pee80]).

However, the aim of this work lies well below the last mentioned items: In the following Sections we will see the effects of dynamical friction (see, e.g. [Tre84] and the Appendix) on the flow of model galaxies in the different canonical potentials of a Voronoi foam (wall, filament and node). Whether we are allowed to do so depends on the time scale on which galaxies are forming [Thu75, Ost75].

[1] Called after a mathematican who described this peculiar partition of space in the beginning of our century. Its elements (the Voronoi cells) are also known as Wigner-Seitz cells.

Chapter 3

Models for Walls, Nodes and Filaments

In this Section, first the formulae for the different potentials (wall, filament, node and the potential of the particles) are derived. Then the formulae and relations for the different energies involved are presented. Finally, the relation between the model units (dimensionless length scale $[l_u]$, dimensionless velocity scale $[v_u]$ and dimensionless time scale $[t_u]$) and physical units are outlined.

3.1 Potentials of Walls, Filaments and Nodes

The potentials of wall, filament, node and the potential of the particles all are determined (except for a constant) by the equation of Poisson:

$$\Delta\Phi = G\,\rho \tag{3.1}$$

where G is the gravitational constant, ρ is the mass density and Φ is the potential of a vectorfield

$$\mathbf{F} = -\nabla\Phi \tag{3.2}$$

A potential always exists if the force $\mathbf{F}$ is conservative which can be expressed by the curl of $\mathbf{F}$ to vanish:

$$\operatorname{curl}\mathbf{F} = 0 \tag{3.3}$$

The potential is well-defined for each point an depends only on its coordinates in space. It has units of an energy.

The Poisson equation also is called potential equation or static field equation and the theory of solving it is refered to as potential theory (cf. e.g. [Kel29]).

In certain symmetric configurations as it is the case for the potentials wall, filament and node we can solve Eq. 3.1 by the method of equipotential surfaces. The method of equipotential surfaces consists in the choice of an appropriate coordinate system and in the choice of so-called *Gaussian surfaces* around the

mass density distribution on which the vectorfield remains constant. The Poisson equation then can be solved by integrating it over the volume A included by the Gaussian surfaces as follows

$$\int_A \operatorname{div} \nabla\Phi \, d^3x = G \int_A \rho \, d^3x \tag{3.4}$$

using a theorem of Gauss [1] that in 3 dimensional euclidian space states that

$$\int_A \operatorname{div} \mathbf{F}(\mathbf{x}) \, d^3x = \int_{\partial A} \langle \mathbf{F}(\mathbf{x}), \hat{n} \rangle \, dS(\mathbf{x}) \tag{3.5}$$

where $\langle \, , \hat{n} \rangle$ denotes the oriented projection of the vectorfield $\mathbf{F}$ perpendicular to the surface ∂A of the volume A. Note that we have used in eq. 3.4 the operator identity $\Delta = \operatorname{div} \nabla$.

For an infinite wall of surface mass density Π perpendicular to $\hat{x}$ we can choose as Gaussian surface a box of size $L^2\rho_0$. We demand $L \gg \rho_0$ so that boundary effects can be neglected. Then we integrate Eq. 3.1 over the box in cartesian coordinates where we replace the divergence of the force according to Gauss's Theorem

$$\int_{\partial A} \langle \mathbf{F}(\mathbf{x}), \hat{x} \rangle \, dS(\mathbf{x}) = -G \, \Pi \, L^2 \tag{3.6}$$

where only the surfaces perpendicular to $\hat{x}$ contribute

$$2|\mathbf{F}|L^2 = -G \, \Pi \, L^2 \tag{3.7}$$

or, equivalently

$$F = -\frac{G \, \Pi}{2} \operatorname{sgn}(x) \tag{3.8}$$

where sgn denotes the sign-function.

The potential can be found by integrating over x to be

$$\Phi = \frac{G \, \Pi}{2} |x| \tag{3.9}$$

We thereby demanded the potential to vanish at $x = 0$. Introducing a softening length b to make the potential smooth we write:

$$\Phi_w = \frac{G \, \Pi}{2} \sqrt{x^2 + b^2} \tag{3.10}$$

Therefrom we derive the force field $\mathbf{F} = (F_x, F_y, F_z)$ of the softened potential:

$$\begin{aligned} F_x &= -\frac{G \, \Pi}{2} \frac{x}{\sqrt{x^2 + b^2}} \\ F_y &= 0 \\ F_z &= 0 \end{aligned} \tag{3.11}$$

[1] Also called Divergence Theorem or Green's Theorem.

For the infinitely elongated filaments of line mass density Ξ along $\hat{z}$ we use a cylinder of length L and radius ρ_0 as Gaussian surface. We again demand that $L \gg \rho_0$ so that we neglect boundary effects. Integration of Eq. 3.1 in cylindrial coordinates using Gauss's Theorem gives

$$2\pi\rho_0 L\,|\mathbf{F}| = -G\,\Xi\,L \tag{3.12}$$

or, equivalently

$$F = \frac{G\,\Xi}{2\pi\rho_0} \tag{3.13}$$

which we integrate in cylindrial coordinates introducing a softening length b

$$\Phi_f = \frac{G\,\Xi}{2\pi} \ln\sqrt{x^2+y^2+b^2} \tag{3.14}$$

where we have changed to cartesian coordinates by $\rho_0^2 = x^2 + y^2$. We demanded the potential to be equal to 1 on the surface [2]. For the vectorfield, we derive

$$F_x = -\frac{G\,\Xi}{2\pi}\frac{x}{\sqrt{x^2+y^2+b^2}} \tag{3.15}$$

$$F_y = -\frac{G\,\Xi}{2\pi}\frac{y}{\sqrt{x^2+y^2+b^2}} \tag{3.16}$$

$$F_z = 0 \tag{3.17}$$

The node as well as the potentials of the particles are modelled by a point mass. The corresponding Gaussian surfaces are the spheres centered at the point mass. We integrate the Poisson equation in spherical coordinates by means of Gauss's Theorem to

$$4\pi r^2\,|\mathbf{F}| = -G\,M \tag{3.18}$$

or, equivalently

$$F = -\frac{G\,M}{4\pi r^2} \tag{3.19}$$

Integrated in spherical coordinates and softened by a softening length b we obtain the potential of Plummer spheres which is in cartesian coordinates ($r = \sqrt{x^2+y^2+z^2}$) given by

$$\Phi_n = -\frac{G\,M}{4\pi}\frac{1}{\sqrt{x^2+y^2+z^2+b^2}} \tag{3.20}$$

where we demand the potential to vanish at infinity. For the vectorfield we derive

[2] The surface consisting of all points where a quadratic form $ux^2+vy^2+wz^2+b$ vanishes is also refered to as *quadric* or *hypersurface of 2nd order*. It here exists only for $b < 1$ and consists of a cylinder of radius b.

$$F_x = \frac{x\,G\,M}{4\pi\left(x^2+y^2+z^2+b^2\right)^{3/2}} \tag{3.21}$$

$$F_y = \frac{y\,G\,M}{4\pi\left(x^2+y^2+z^2+b^2\right)^{3/2}} \tag{3.22}$$

$$F_z = \frac{z\,G\,M}{4\pi\left(x^2+y^2+z^2+b^2\right)^{3/2}} \tag{3.23}$$

3.2 Energy, Dissipation and Momentum

The equations of motion for each particle are directly obtained by summing over the forces due to the central potential (wall, filament or node) and over the contibutions of all other particles attributing a dissipational term

$$\mathbf{F}_d = m\,\frac{d\mathbf{v}}{dt} = -\eta\,m\,\mathbf{v} \tag{3.24}$$

with the viscosity between two particles ('galaxies') defined by

$$\begin{aligned}\eta_{12} &= 16/3\pi^2 \log\Lambda\, G^2 m_1 m_2 \left(\delta_1^2\delta_2^2\right)^{-3/2}\left(\sigma_1^2\sigma_2^2\right)^{-3/2} \times \\ &\quad \times \exp - \left(\frac{R^2}{\delta_1^2+\delta_2^2} + \frac{V^2}{\sigma_1^2+\sigma_2^2}\right)\end{aligned} \tag{3.25}$$

where we will assume equal masses of the particles $m = m_1 = m_2$, identical core sizes $\delta = \delta_1 = \delta_2$ and identical internal velocity dispersions $\sigma = \sigma_1 = \sigma_2$. The strength of the viscosity is scaled by the *Coulomb logarithm* $\log\Lambda$. The viscosity depends exponentially on the distance R between the particles in location space and on their distance V in velocity space. The justification for this equation can be found in the Appendix.

The total energy E of our system is given by the kinetic energy of the N particles

$$E_k = \sum_{i=1}^{N} \frac{m_{(i)} v_i^{\,2}}{2} \tag{3.26}$$

and by the potential energy of the particles according to the central potential (wall, filament or node)

$$E_p = \sum_{i=1}^{N} \Phi_{w,f,n}(\mathbf{x}_i) \tag{3.27}$$

and by the *self-energy* which we define to be the field energy due to the gravitational field of the particles. We obtain it by summing the contributions of each particle to the potential field of the sample

$$
\begin{aligned}
E_s &= -\frac{G}{2}\sum_{k=1}^{N}\sum_{j\neq k=1}^{N}\frac{m_{(k)}m_{(j)}}{\sqrt{r_{kj}^2+b^2}} \\
&= -G\sum_{j<k}\frac{m_{(k)}m_{(j)}}{\sqrt{r_{kj}^2+b^2}}
\end{aligned}
\tag{3.28}
$$

Hence we write

$$E = E_k + E_p + E_s \tag{3.29}$$

where E_p has to be evaluated for wall, filament or node respectively.

The total energy would only be conserved in a conservative system, that is without the dissipational term 3.24. It is therefore useful to define a differential dissipational energy as

$$dE_d = \mathbf{F}_d d\mathbf{x} \tag{3.30}$$

where $\mathbf{F}_d$ is the dissipational force 3.24 and $d\mathbf{x}$ denotes the line-element. In the numerical model $d\mathbf{x}$ is linked to the global time step so that it is not infinitesimal. One may expect that as long as the dissipational energy does not change over magnitudes, Eq. 3.30 will give a good estimate of the energy being lost due to dissipation.

We now can define a quantity

$$E' = E_k + E_p + E_s + \int_{t_0}^{t} dE_d(t) \tag{3.31}$$

which is conserved in time as long as the dissipational energy changes moderately.

We calculate a kinetic temperature T from the arithmetic velocity mean $\bar{v}$ according to

$$T = \frac{\pi}{8}\frac{m}{k}\,\bar{v}^{\,2} \tag{3.32}$$

In case of a maxwellian velocity distribution, T actually defines the thermodynamic temperature of the particles. Apart from constant factors, Eq. 3.32 is a direct consequence of the equipartition theorem $kT \propto \bar{v}^{\,2}$. Since we are not interested in constant factors, we set the Boltzmann constant $k = 1$. Near equilibrium, we expect that T will steadily decrease corresponding to the dissipational loss of energy. The temperature so defined is by definition correlated to the kinetic energy. Note that, in case of a maxwellian velocity distribution, the correlation is 1. In case of a non-maxwellian distribution, the correlation will differ from 1, even if the deviation is not expected to be large.

We further are interested in the conserved quantities linear momentum

$$
\begin{aligned}
\mathbf{P} &= \sum_{i=1}^{N} m_{(i)}\mathbf{v}_i \\
P &= |\mathbf{P}|
\end{aligned}
\tag{3.33}
$$

and angular momentum

$$\begin{aligned} \mathbf{L} &= \sum_{i=1}^{N} r_i \times m_{(i)} \mathbf{v}_i \\ L &= |\mathbf{L}| \end{aligned} \tag{3.34}$$

to verify the algorithms' reliability and to separate out numerical effects. A useful tool to study the energy diagrams will be the relations between potential energy and kinetic energy after the particles have set into thermal equilibrium. Those can be derived from the theorem for the virial of Clausius [Gol87]

$$\langle T \rangle = -\frac{1}{2} \langle \sum_{i=1}^{N} \mathbf{F}_i \mathbf{r}_i \rangle \tag{3.35}$$

which holds for periodic motion where $\langle\ \rangle$ denotes the temporal mean over one period and for ergodic motion where the temporal mean has to be taken over a sufficiently large time.

In the case of forces derived from a potential Eq. 3.35 can be written

$$\langle T \rangle = \frac{1}{2} \langle \sum_{i=1}^{N} \nabla \Phi_i \, \mathbf{r}_i \rangle \tag{3.36}$$

which we evaluate for the potential of the wall to be

$$\begin{aligned} \langle T \rangle &= \frac{G\,\Pi}{4} \langle \frac{x\,\partial \sqrt{x^2 + b^2}}{\partial x} \rangle \\ &= \frac{(G\,\Pi)^2}{8} \langle \frac{x^2}{\Phi_w} \rangle \end{aligned} \tag{3.37}$$

Note that Eq. 3.37 is proportional to $\langle x \rangle$. This expresses that the mean kinetic energy of the particles increases with the mean distance of their trajectories from the wall.

For the potential of the filament we obtain

$$\begin{aligned} \langle T \rangle &= \frac{G\,\Xi}{4\pi} \langle \frac{x\,\partial \ln \sqrt{x^2 + y^2 + b^2}}{\partial x} + \frac{y\,\partial \ln \sqrt{x^2 + y^2 + b^2}}{\partial y} \rangle \\ &= \frac{G\,\Xi}{4\pi} \frac{1}{1 + \langle \frac{b^2}{x^2 + y^2} \rangle} \end{aligned} \tag{3.38}$$

so that, if we suppose the temporal mean $\langle b^2 (x^2 + y^2)^{-1} \rangle$ to be small compared to 1, the kinetic energy in a logarithmic potential is found to be independent of the potential energy. Especially all initial velocity distributions are "virialized" in respect to the logarithmic potential[3].

[3] But not to the potential of the selfgravitating particles.

For the node potential and the potential of the particles we obtain

$$\begin{aligned}\langle T\rangle = -\frac{G\,M}{8\pi} \quad & \langle \frac{\partial}{\partial x}\left(\frac{x}{\sqrt{x^2+y^2+z^2+b^2}}\right) \\ & + \frac{\partial}{\partial y}\left(\frac{y}{\sqrt{x^2+y^2+z^2+b^2}}\right) \\ & + \frac{\partial}{\partial z}\left(\frac{z}{\sqrt{x^2+y^2+z^2+b^2}}\right)\rangle \\ = -\frac{1}{2}\langle\Phi_n\rangle \quad & \frac{1}{1+\langle\frac{b^2}{x^2+y^2+z^2}\rangle}\end{aligned} \tag{3.39}$$

which is the virial theorem for Plummer spheres. If we suppose the temporal mean $\langle b^2(x^2+y^2+z^2)^{-1}\rangle$ to be small compared to 1, Eq. 3.39 reduces to the virial theorem for an r^{-1} potential:

$$\langle T\rangle = -\frac{1}{2}\langle\Phi\rangle \tag{3.40}$$

For the sake of self-consistency, we have used for the softening length b of the particles the core size of the galaxies δ in all 100 and 1000 particle experiments. Thereby the softening length of the filament potential and node potential has been set to 1, whereas in the case of the wall potential a softening (smoothing) length of size 10^{-2} has been introduced.

3.3 Scaling

The scaling has been done for the "high attracting" potential experiments with 1000 particles as follows: If we suppose the size of the cube used within the numerical model to be 100 Mpc, we obtain for the dimensionless coordinates running from -50...50 as relation between the length units:

$$1 \text{ dimensionless length unit } [l_u] \equiv 1Mpc \tag{3.41}$$

A given galaxy has size δ and mass m, therefore its internal velocity dispersion $\sigma = \sqrt{\langle v^2\rangle}$ obeys approximately the relation

$$\langle v^2\rangle = \frac{G\,M}{\delta} \tag{3.42}$$

with G as gravitational constant, m as mass of the galaxy and $\langle\ \rangle$ denoting the ensemble mean of the velocities. If δ were the gravitational radius [Bin87], Eq. 3.42 would hold exactly as a consequence of the virial theorem 3.40.

If $x = 1$ corresponds to 1 Mpc, then

$\delta = 1$	is a 100 kpc halo	("big")
$\delta = 0.1$	is a 10 kpc halo	("medium")
$\delta = 0.01$	is a 1 kpc halo	("small")

(3.43)

According to Eq. 3.42 we can calculate the corresponding velocity dispersions to be

$$\begin{array}{ll} \sigma = 3.2 & \text{for big halos} \\ \sigma = 10 & \text{for medium halos} \\ \sigma = 32 & \text{for small halos} \end{array} \tag{3.44}$$

We extend these definitions to

$$\begin{array}{lll} \delta = 0.1 & \sigma = \left\{ \begin{array}{ll} 1 & \text{"big"} \\ 3.2 & \text{"medium"} \\ 10 & \text{"small"} \end{array} \right. & \\ \delta = 0.01 & \sigma = \left\{ \begin{array}{l} 3.2 \\ 10 \\ 32 \end{array} \right. & \\ \delta = 0.001 & \sigma = \left\{ \begin{array}{l} 10 \\ 32 \\ 100 \end{array} \right. & \end{array} \tag{3.45}$$

where we have introduced small, medium and big internal velocity dispersions which we have expressed in dimensional velocity units $[v_u]$.

Because our particle density is much less than the density n of galaxies in a real cluster, we would underestimate the mean free path of a particle while determining the size of a model galaxy correspondant to the size of the cube. We therefore correct for the particle density:

$$n = \frac{N}{L^3} \tag{3.46}$$

where L denotes the size of the structure and N denotes the number of particles.

We do this correction while introducing a second length scale λ

$$\lambda = L\, N^{-1/3} \tag{3.47}$$

to describe the particle density. In a 100 Mpc structure, we may expect 10^6 galaxies, whereas we use only 10^3 galaxies in our model. We correct by

$$\lambda \rightarrow \lambda \left(\frac{10^6}{10^3} \right)^{1/3} = 10 \times \lambda \tag{3.48}$$

so that, where we used $\delta = 0.1$, we correct for the second length scale to $\delta = 1$ by

$$
\begin{array}{lll}
\delta = 1 & \text{“big”} & \sigma = \left\{ \begin{array}{ll} 1 & \text{“big”} \\ 3.2 & \text{“medium”} \\ 10 & \text{“small”} \end{array} \right. \\
\delta = 0.1 & \text{“medium”} & \sigma = \left\{ \begin{array}{l} 3.2 \\ 10 \\ 32 \end{array} \right. \\
\delta = 0.01 & \text{“small”} & \sigma = \left\{ \begin{array}{l} 10 \\ 32 \\ 100 \end{array} \right.
\end{array}
\tag{3.49}
$$

A galaxy velocity dispersion of 250 $km\,s^{-1}$ (which is about equal the velocity of a typical star [Egg62]) hence corresponds to 10 units $[t_u]$ (medium):

$$
1 \text{ dimensionless velocity unit } [v_u] \equiv 25 km\,s^{-1} \tag{3.50}
$$

We estimate the velocity dispersion σ in a cluster of size 3 Mpc consisting of 10 galaxies to be 3 times ($\approx \sqrt{10}\times$) as large, that is 30 units $[v_u]$. We therefrom obtain a timescale by evaluating

$$
\sqrt{\frac{G\,M}{\delta}} \left[\frac{x_u}{t_u} \right] = 30[v_u] \tag{3.51}
$$

to

$$
\begin{aligned}
1 \text{ dimensionless time unit } [t_u] &= \frac{\sqrt{\frac{10}{3}}\,[x_u]}{30[v_u]} \\
&\approx \frac{1}{16}\,\frac{[x_u]}{[v_u]} \\
&= \frac{1}{16}\,\frac{1Mpc}{25km\,s^{-1}} \\
&\approx \frac{1}{16}\,\frac{1Mpc}{\frac{1}{40}\,\frac{1Mpc}{1Gyr}} \\
&= 2.5\,Gyr
\end{aligned}
\tag{3.52}
$$

In all diagrams, 1 dimensionless time unit $[t_u]$ correponds to 10 units on the time axis, for the time step size was 0.1 for all calculations. Therefore, according to the scaling the time runs from 0 to 10 Gyr for all calculations (except for the program tests in the Appendix).

Chapter 4

Flow of Particles in the Models

In this Chapter, the experiments performed with 1, 10, 100 and with 1000 particles are described.

4.1 Experiments with One Particle

First we want to consider the motion of a single particle in phase-space in the three geometrically different dilutions (wall, filament and node) respectively. The Figures 1...3 show the flow of a single particle, started with initial zero velocity from (1,0,0) (cartesian coordinates). The location x is plotted versus the velocity vx. Equal spacings between points in the diagrams correpond to equal times for the particle to pass from one point to the other. Note that the velocity axis scale for the three potentials differs; For the filament potential, near the singularity of the potential the highest velocities appear. The maximal velocity of the particle in a wall potential is a factor 2 higher than that in a node potential, but is still at least 10 times less high than the maximal velocity in a filament potential.

The diagrams for the node potential and for the filament potential were calculated with each 200 steps in time (of size 0.1). For the node potential, 120 steps in time (size 0.1) were calculated. Thereby the calculation of the particle motion in the wall potential has been done over one period, in the filament potential over 8 periods and in the node potential over 3 periods. We therefrom conclude, that the velocity mean of particle flow without dissipation in the respective potentials is largest for the filament potential, less high for the node potential and lowest for the wall potential. The relaxation time therefore should be expected to be shortest for the filament potential, higher for the node potential and most high for the wall potential. In the experiments with randomly distributed initially "frozen" start of particles, we will see that this expecation is not fulfilled due to momentum creation effects dependent on the interaction of the particles in phase-space: Higher velocities will lead to a higher

amount of momentum created, therefore the relaxation time will be found to be highest for the filament potential.

For the filament potential, a subset of points lies in a low velocity region (namely points far from the potential). Also for the wall potential, the points elongate in velocity space only linear in location space from the region of low velocity to the region of high velocity towards the center of the potential. We therefrom expect in the case of the filament potential and the wall potential that a subset of the particles will be nearly at rest.

Dissipation decreasing with the velocity difference between two particle orbits will work most effectively in the outer regions of the filament potential, whereas near the inner regions the energy loss due to dissipation will decrease (for particles separated only by a small amount in location space according to Fig. 2 differ in the inner regions by a large amount in velocity space). The particles therefore will be slowed down in the outer regions of a filament potential more effectively than in the inner regions, leaving their orbits they would have had without dissipation while approaching the potential. Therefrom we expect the particle orbits to be found attracted by the filament potential, whereas in the case of the wall and node potential the distribution of particles in space is expected to be more smoothed out. As we will see, the filament potential actually tends to attract the orbits of particles .

The Figures 1...3 have been calculated with a potential strength equal to one particle mass unit [*pmu*] and with a softening length of 10^{-12}, choosen 6 magnitudes larger than the minimal substepsize (10^{-18}) permitted.

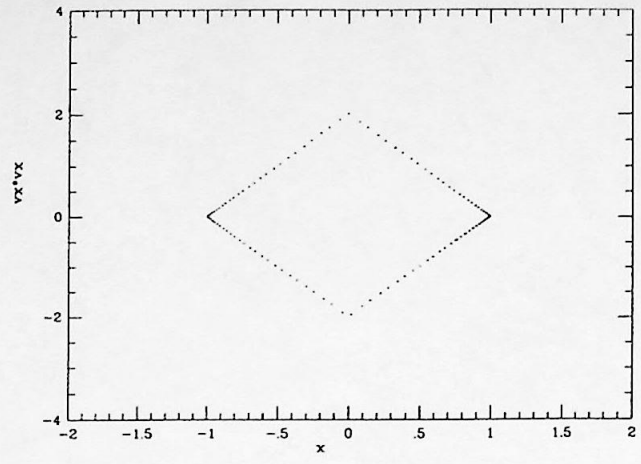

Fig. 1

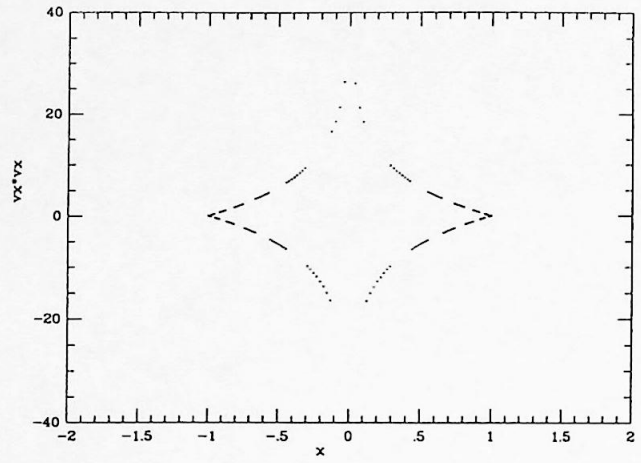

Fig. 2

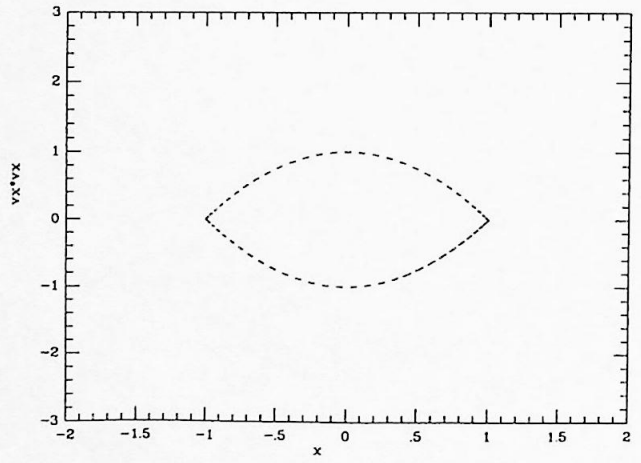

Fig. 3

Figures 1...3: Single particle flow in the potentials wall (top), filament (center) and node (bottom).

4.2 Experiments with 10, 100 and 1000 Particles

When we want to do calculations with more than one particle, we must care for the momentum creation effects as they were already found by Aarseth in the early days of N-body experiments [Aar62].

A common device to suppress these effects is to introduce a softening length b to put away the singularity in the center of the particle potential: This length has to be chosen large enough for the momentum creation effects to be reduced to an acceptable degree (cf. the "collision"-experiments in the Appendix). The force-law thereby is only slightly changed at large distances. One obtains the so-called Plummer-sphere potentials, which can be thought of as a model for an agglomeration of particles, representing stars or clusters of stars or galaxies. Notably, a bound agglomeration of particles would show, if it were spherically symmetric, *exactly* the potential of a point mass outside its boundaries. So the common argument as given above to justify the choice of the Plummer sphere potential is to be taken as an approximation [1].

First calculations were done with a softening length just large enough to permit the algorithm to overcome singularities. This has been in the cases of single particle experiments sufficient to reproduce the trajectories well (cf. Figs. 1...3). In the case of a filament potential of 1 pmu surrounded by 10 particles, the momentum creation effects found by Aarseth have been directly observed: The Figure 4 is taken from a visualisation of the particles in time; Each particle is represented by 20 events in time (i.e. it positions at 20 succeeding timesteps). The particles in the center are orbiting while the two lines leaving to the sides represent two particles, leaving at same time and in oposite direction. Close interaction of particles in the orbits round the potential seems to lead to such "pair-creations". Hence here the occupation of orbits round the filament decays in time.

[1] For we do not exactly know where the galaxies discontinue, we wont worry much about this approximation.

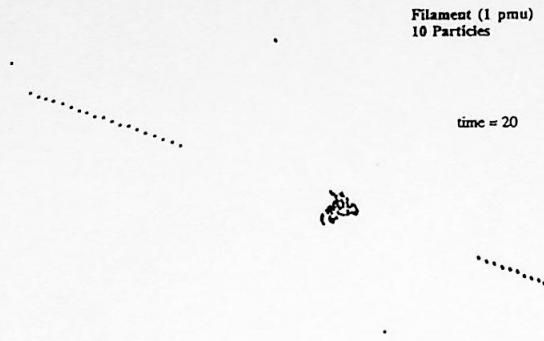

Fig. 4

Fig. 4: Decay of orbits round a filament potential due to momentum creation.

The momentum creation implies creation of kinetic energy, as it can be seen in the Figs. 5 and 6 for a wall potential of strength 1000 pmu. The energy increases stepwise, as in the case of the filament where every increment was due to an decay of two orbits, also in this case where the sample size has been much larger (100 particles).

The same energy diagram for a ten times weaker potential is shown on the left side (for 10 particles). The visualisation in time has shown that the particles were running along the wall. The energy of the oscillating particles (in the wall potential) and the additionnal oscillating kinetic energy (gain due to to momentum creation and loss due to dissipation) superposes to the beats apparent in the total energy and in the kinetic energy.

Figs. 5 and 6: Not-softened particles in a wall potential.

Fig. 5

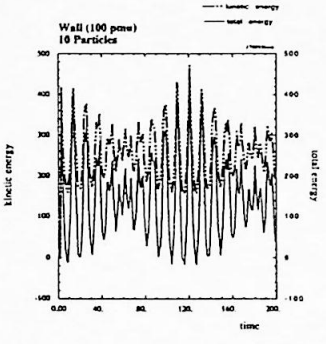

Fig. 6

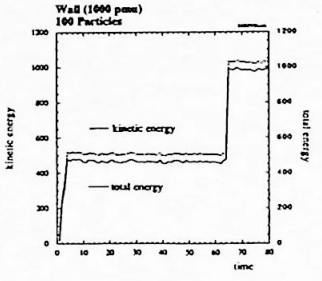

First experiments with 10 particles, softened by a length 10^{-18} (which is absolutely insufficient to suppress momentum creation and only helps the algorithm not to get stuck in singularities), were performed for a node potential of strength 10 × the particles size total mass units ("high attracting" potential strength) and for a node potential of strength 1/10 × the particles size total mass units ("low attracting" potential strength) and are shown in Figs. 7...9: The traces of 10 particles in location space show how these particles, started frozen (initial velocities all zero) in an initial cube of size 2, leave the start region with an evident high amount of kinetic energy which cannot be explained only by exchange of potential (self-) energy between the particles. In the case of the low-attracting node (with a mass of 1 particle mass unit) in Fig. 8 they leave completely the inner potential region, whereas in the case of the high-attracting node (100 pmu in Fig. 7 some of them rest in orbits round the potential of the node. However, shape and size of these orbits indicate that the particles have more energy than they should have according to energy conservation.

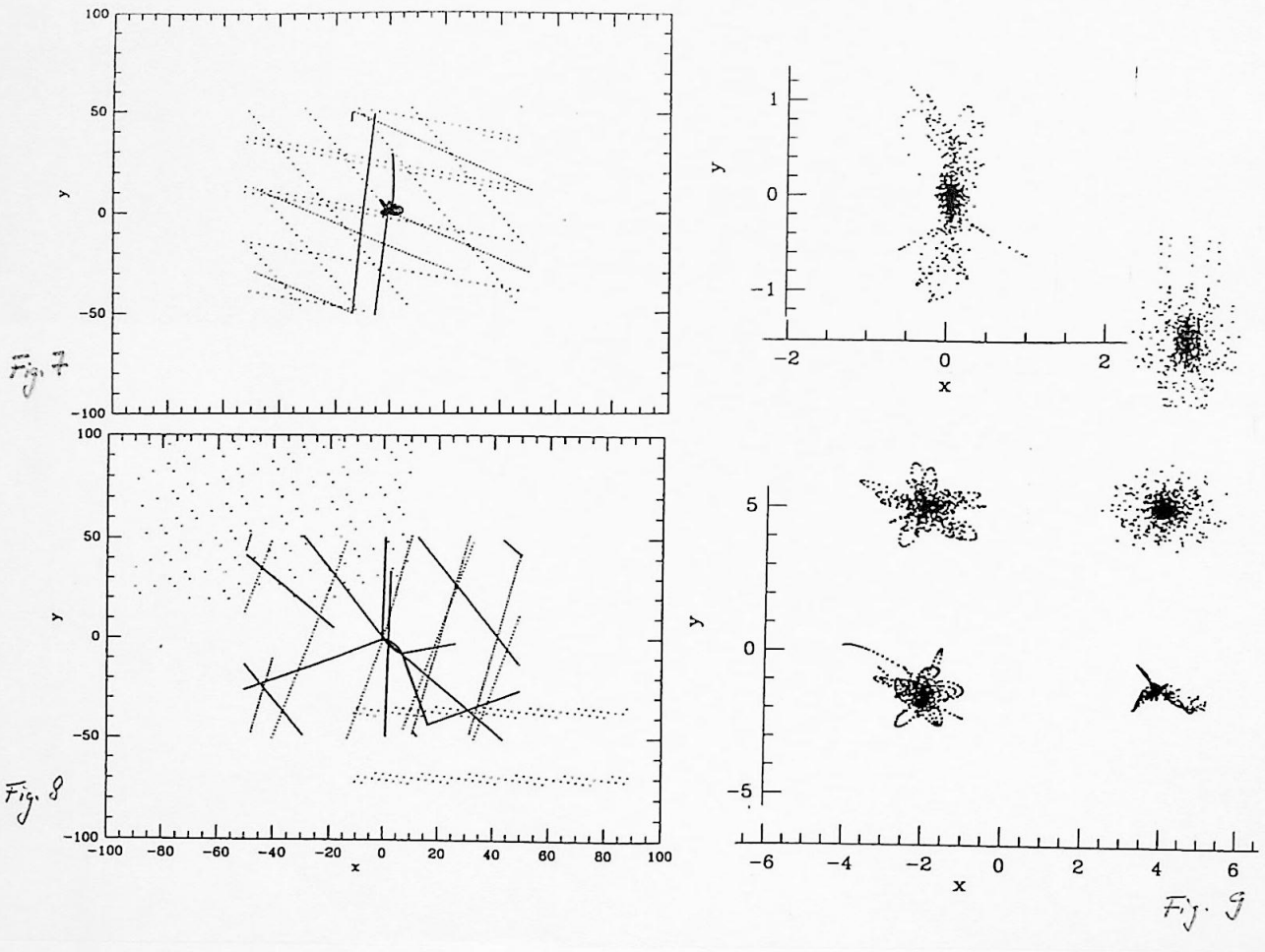

Figs. 7...9: Experiments with 10 particles in "high-attracting" and in "low-attracting" potentials.

After the particles have been softened with a length $b = 1$, the experiments have been repeated for "high attracting" (100 pmu) and "low attracting" (1 pmu) potentials. Fig. 9 shows the "low attracting" experiments on the left side and the "high attracting" experiments on the right side. The dots again represent all events (i.e. the positions in space at all times) for 80 equal timesteps. The wall potential (first row) shows scattering effects (especially for the high attracting potential). This scattering has been due to the non-smoothness of the wall potential. The trajectories of the particles in the potentials are all strongly affected by momentum creation. Because the momentum is no more stepwise but rather adiabatically enhanced (the mean kinetic energy for comparable experiments did not show discontinuities), the effect is (almost) not visible in the shape of the trajectories. However, the scattered points round the high attracting filament potential (second row) and node potential (third row) indicate that scattering in velocity space (momentum creation) occurs.

First I have wondered whether the scatter pattern might be due to bad determination of the trajectories of the particles. Therefore I have examined whether a tree code would do better in determining the trajectories. The answer in case of evaluation of the particle interaction only all global time steps was no as shown in the Appendix.

As it was noticed by Aarseth, the individual encounter effects decrease with N due to the forces acting on a single particle becoming more and more determined by the effective potential rather than by its nearest neighbours with increasing sample size. In an effective potential of all particles, the number of collisions (or close encounters) will be lower, momentum creation therefore will be less evident than in experiments with only a few particles.

We point out that the momentum creation is truly numerical and has nothing to do with the modified force-law (due to softening), since the conservation of momentum follows from the translational symmetry (Galilei-invariance) [2] in euclidian space and does therefore not depend on the explicit form of the force-law.

Experiments with softened particles have been performed with sample sizes of 100 particles. The particles were started "frozen" (kinetic temperature $T = 0$) equally distributed in a starting cube of size 2. The results are shown in Figs. 10...12. Kinetic energy, potential energy and self-energy have been calculated and are shown in the right side of the location space diagrams (respectively below, for the node). As definition for the total energy, the sum of kinetic, potential and self-energy has been used. The self-energy of the system decreases strongly during the first few time-steps. The kinetic energy thereby hardly is affected. Afterwards, the self-energy increases in time. This is due to numerical adiabatic momentum creation. I call it 'adiabatic' because it seems not to affect the kinetic energy of the sample. The node still shows pair creation effects. These effects now do not come from the forces becoming singular – for they all have been softened – but from an (for small distances) ill defined vector of unity.

After this imperfection was removed, the calculations have been done another time: The calculated trajectories (all events and 40 time-steps) are shown in the second column of Figs. 13...15: They hardly differ from the Figs. 10...12. Only the node has become a bit more quiet. But one must realize that the initial starting cube (where the particles have been started "frozen") has had a size of 2, whereas the apparent trajectories fill a much larger region in space.

[2] After a theorem by Emilie Noether

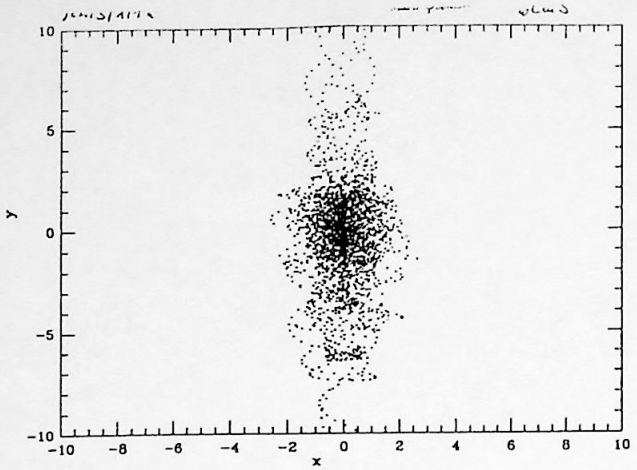

Fig 10

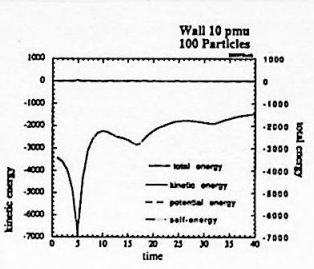

Fig. 10b

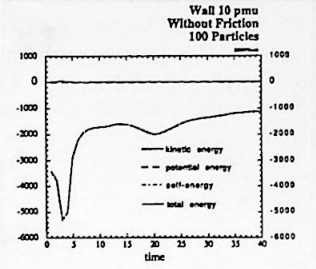

Fig 10c

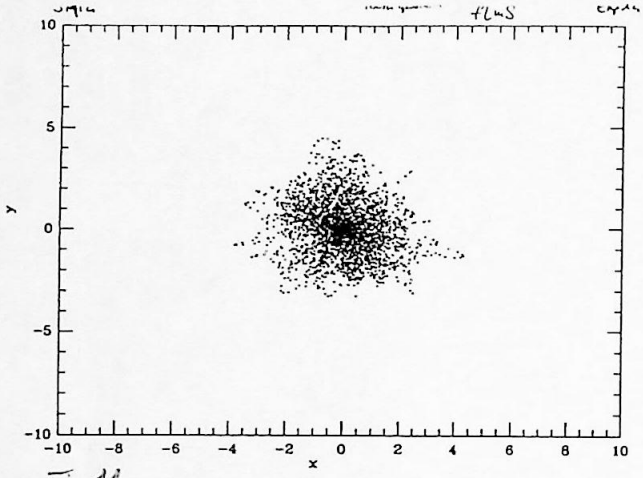

Fig. 11

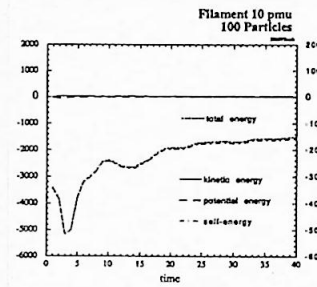

Fig. 11b

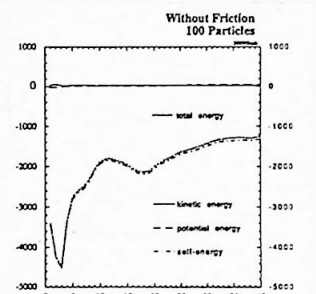

Fig 11c

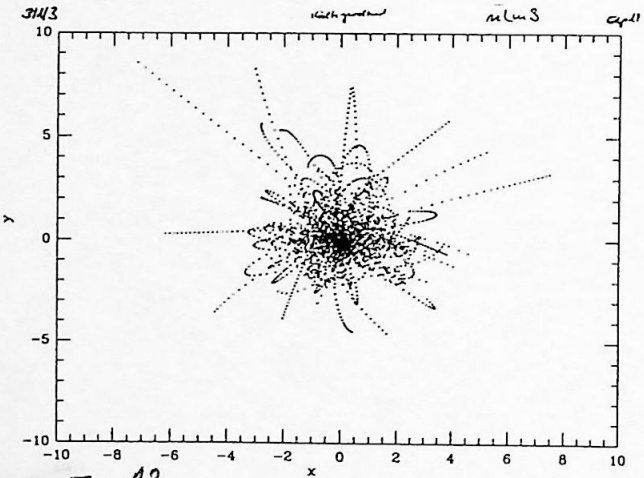

Fig. 12a

Figs. 10...12:
Experiments with 100 particles and ill defined vectors of unity. Particles in the wall potential are shown on top, particles in the filament potential are shown in the center and particles in the node potential are shown at the bottom of the page.

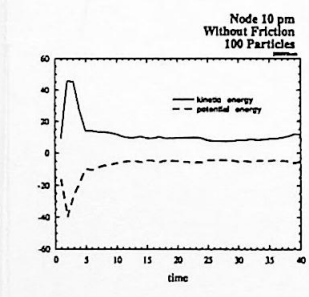

Fig 12b

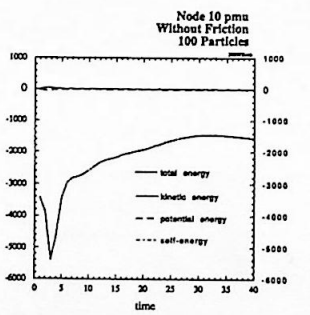

Fig 12c

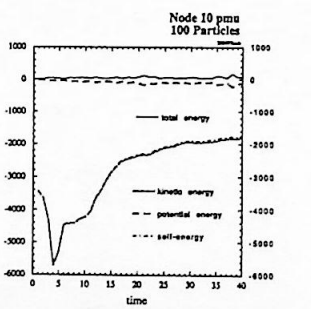

Fig 12d

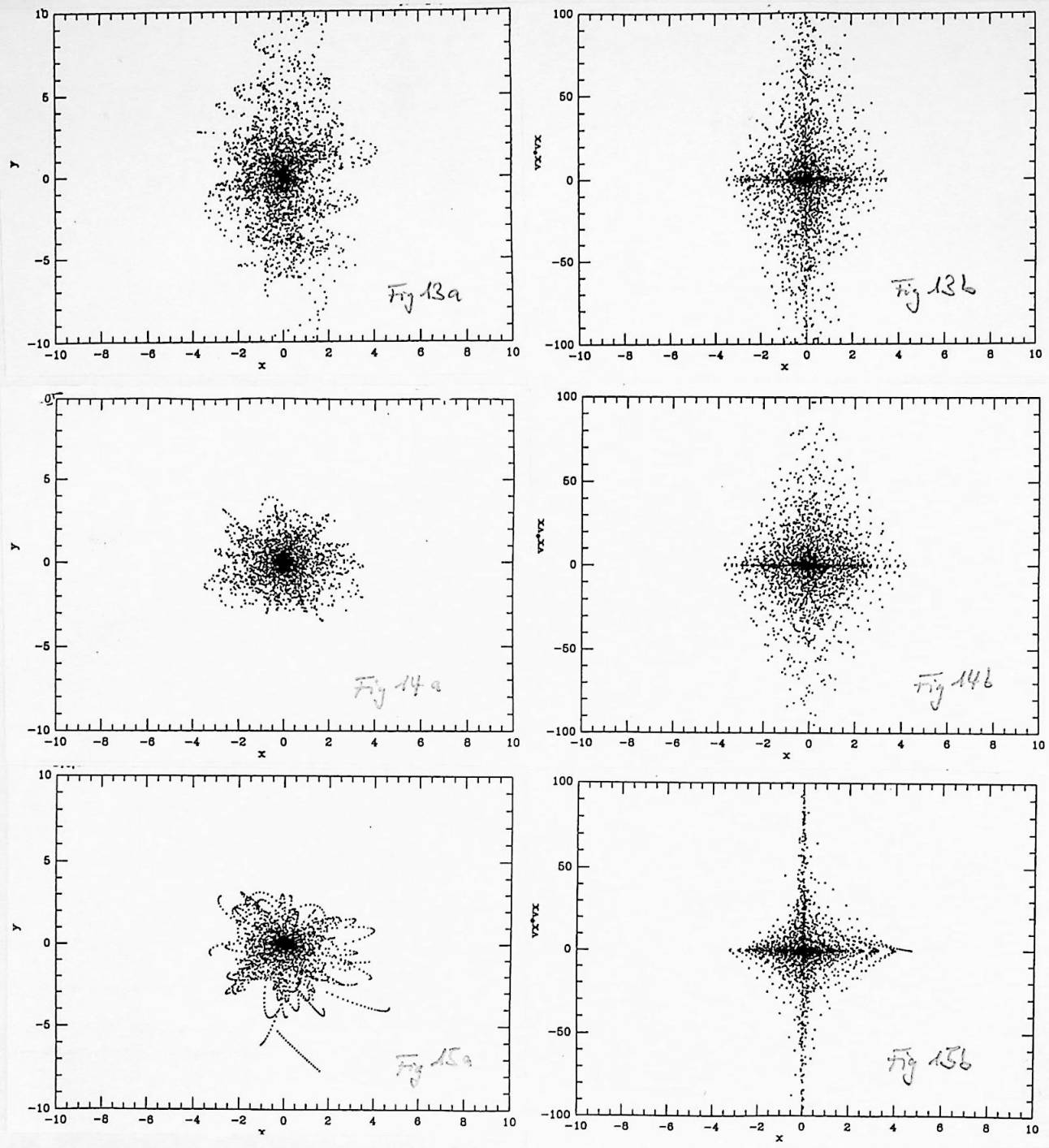

Figs. 13...15: Experiments with 100 particles and well defined vectors of unity. Again the flow in the wall potential is shown on top, the flow in the filament potential is shown in the center and the flow in the node potential is shown on the bottom of the page. On the left side, the location space diagrams are shown; On the right side, the diagrams in location-velocity space are shown. They all hardly differ from each other what indicates, that still numerical effects are dominating the flow of particles.

From the previous experiments has been concluded that not only the potentials of the particles, but also the potentials (wall, filament and node) are to be smoothed, to suppress effectively the momentum creation effects. Since in the case of the wall potential it is not evident (the wall potential is nowhere singular), the effect of a not-smoothed wall potential has been investigated separately and the result is shown in the Appendix.

The Figs. 16...21 show the cumulative distribution of particles for all times, i.e. for T=1...40, where one unit corresponds to 0.1 dimensionless time unit $[t_u]$ (= 250 Myr, cf. Section 3.3). The distributions can be interpreted to represent the probability to find a particle in a given volume within the dimensionless time 0...4 (0...10 Gyr) within the different geometrical dilutions (wall, filament, node).

The first and second column show the distribution calculated for dissipational flow (core size $\delta = 1$, internal velocity distribution $\sigma = 1$), whereof the second column is a magnification of the first column. The third and fourth column show the same calculations performed for dissipationless flow. The magnification is not set equal for each diagram, but set to the "most interesting" interior of the corresponding diagrams to the left.

The particles all have been started frozen (kinetic temperature $T = 0$) from an random equal distribution in an initial cube of size 2. The potential strength has been "low attracting" in comparision to the self-attraction of the particles. Therefore the calculations represent a superposition of the collapse and the characteristic flow of the particles in the respective background potential (wall, filament, or node).

The effect of the different geometric dilutions is nevertheless visible, in particular the different "stickiness" of particles inside the potentials is manifested by the different patterns as they are, in case with dissipation, elongated along the wall potential, consisting of an asymmetric arrangement of dots in case of the filament potential and consisting of an asymmetric agglomeration of particles in the case of the node potential.

The apparent asymmetry in the case of the node potential can be explained by the potential field energy of all particles brought to the center being about 10 times higher than the potential field energy due to the node potential itself. In the calculations without dissipation, the central region almost remains empty.

The flow of particles has been studied in 3D-space in time within two different resolutions (whole volume and magnification of the center). In the following I describe the observation which I have made in case of the "low attracting" experiments with 100 particles:

Wall The particles collapse to the center, forming an overdense region from which they escape mainly in y and z direction. Afterwards they oscillate mainly singular. The number of free flowing particles has decreased. The magnification shows: The collapse takes place in two "pulses". The particles approach closer in the second pulse than in the first. A part of the particles forms a dense region during the second pulse and continues collapsing. Particles coming near this collapse center rush after.

Wall Without Dissipation The particles collapse rapidly. A part of them

gets dispersed in the x direction. Afterwards, the particles escape explosion--like in all directions. The magnification shows: During the collapse, for a very short period, two centers of increased density form. The particles rapidly escape from these regions leaving empty space. They move very fast in consequence (high kinetic energy).

Filament The collapse takes place in at least four pulses. A considerable amount of the particles vanishes in the center. The magnification shows that in the central region a collapse center is forming, into which the particles disappear.

Filament Without Dissipation The particles collapse, where the pulses are clearly weaker (hardly noticeable) in comparision with the pulses described above. The magnification shows that very early an agglomeration of particles near the center forms. By further succession of particles an overdense ring around the potential forms. The particles in the center finally escape, whereas immedately others rush after. A collapse center does not appear. The kinetic energy is only slightly enhanced in comparision to the flux in the wall potential.

Node The particles rapidly collapse into the center where they form a spherical overdense region. Afterwards, the center of the spherical overdense region becomes more and more empty. Thereby a part of the particles is thrown out, but not very far. The particles recollapse to a smaller, denser sphere and therefrom collapse very fast into a point, as the magnification has shown.

Node Without Dissipation The particles again collapse to a sphere, the center of which is becoming more and more empty. The sphere finally contracts while throwing out particles, finally expands while kinetic energy increases. The magnification shows that, after an initial agglomeration of particles has been dissolved, the center of the potential rests of same particle density than its surroundings.

This observational study can be interpreted as the flow of particles being dominated by the collapse of the selfgravitating sample dominating the flow in the respective background potential (wall, filament , node). A large amount of momentum has been created as can be seen from the energy and momentum diagrams (Figs. 22...27). As momentum, the absolute (scalar) values have been used in the Figures. In all cases of potentials (wall, filament, node), the self-energy increases much faster without than with dissipation. For the self-energy is a measure of the mean density of particles near the potential this shows that, whereas with dissipation several "pulsations" of the particles have occurred, the particles without dissipation after an initial collapse have been diluted over a comparatively large region. Kinetic and self-energy are anticorrelated, as is demanded from by virial theorem of the potentials of the particles. This is compatible with the potential of the particles dominating the contribution of gravitational energy from the central potential. The conclusion that the potentials of the particles dominate the flux in these experiments can be further

supported by comparing the energy diagrams (Figs. 22...24) with the energy diagrams in case of the pure collapse (Figs. 34). The momentum diagrams (figs. 25...27) show the increase of momentum being correlated with the pulsations. In case of dissipation, the creation of momentum is partially canceled by the dissipational loss of energy.

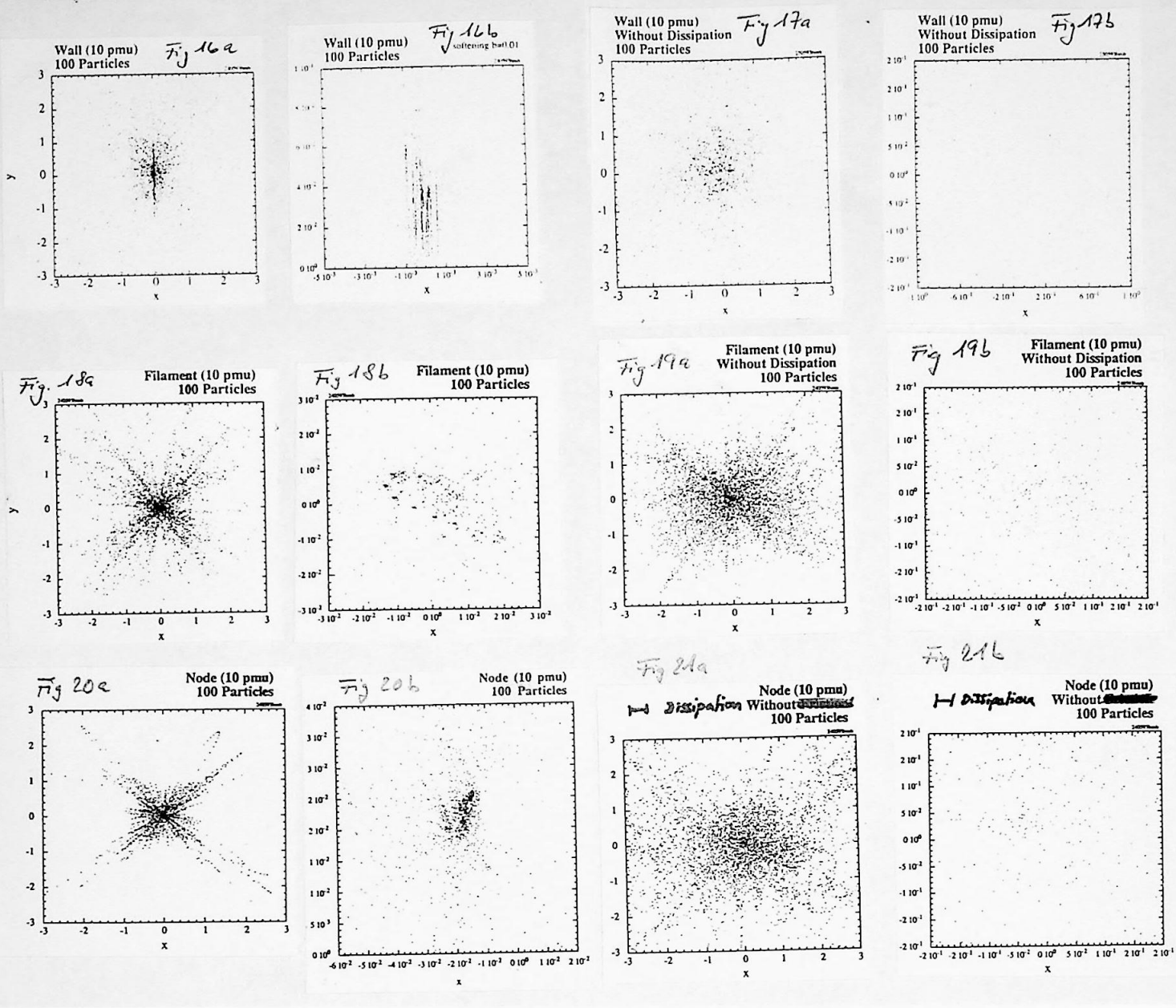

Figs. 16...21: 100 particle experiments with and without dissipation. The different distributions of points are interpreted in the text.

Figs. 22...24: Energy diagrams to the 100 particle experiments with and without dissipation.

Fig 2.2 a

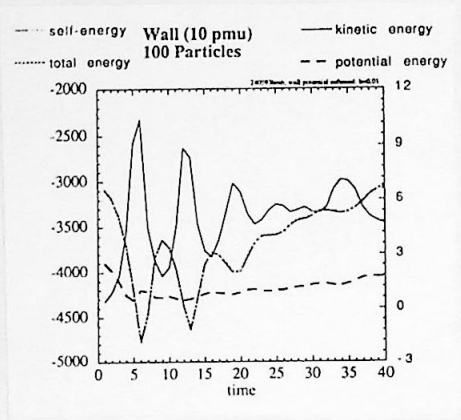

Fig 2.2 b

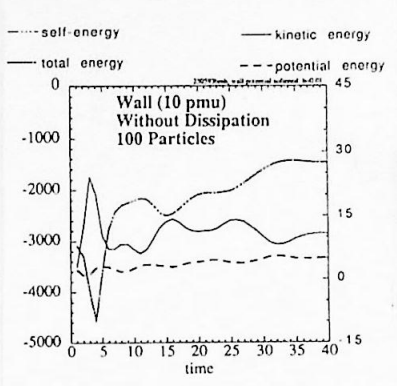

Fig. 2.3 a

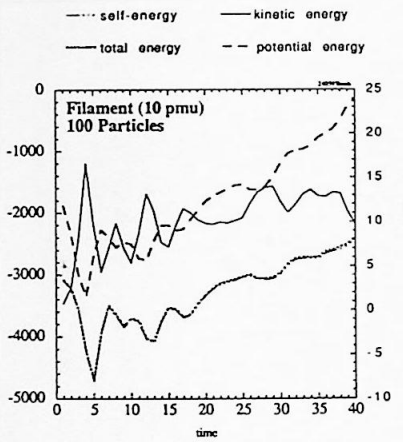

Fig. 2.3 b

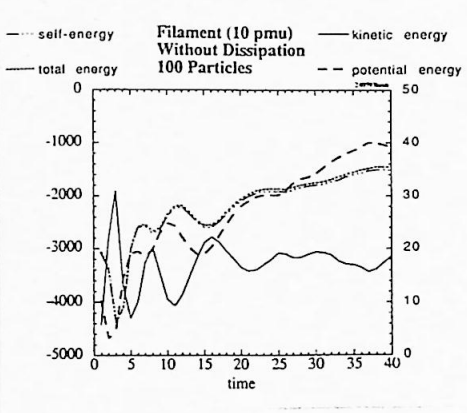

Fig. 2.4 a

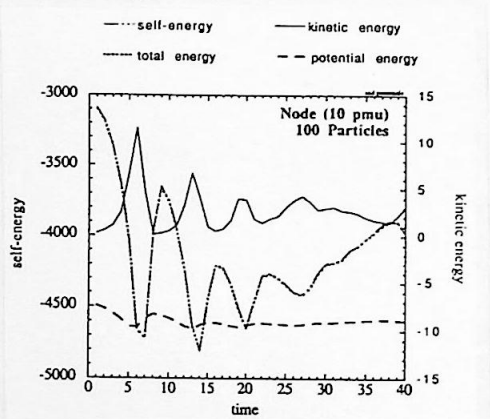

Fig. 2.4 b

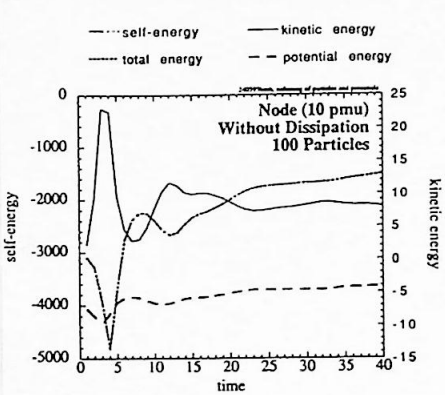

Fig 25a

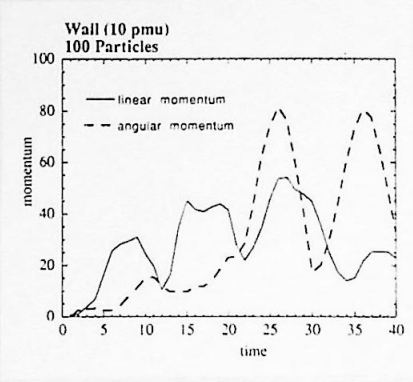

Fig 25b

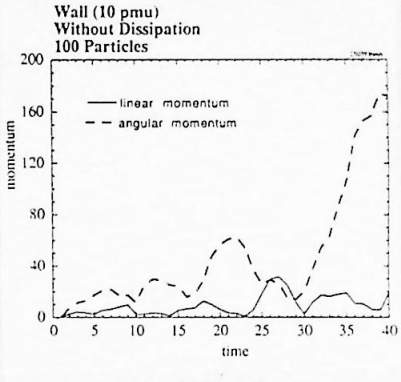

Fig 26a

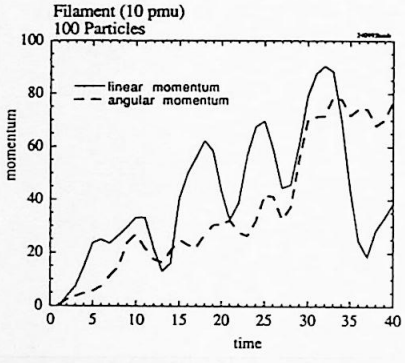

Fig. 26b

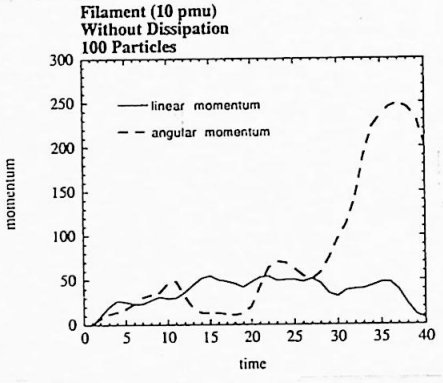

Fig. 27a

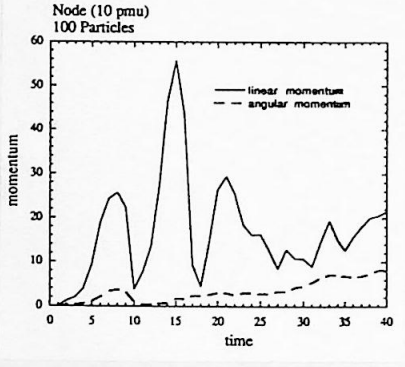

Fig. 27b

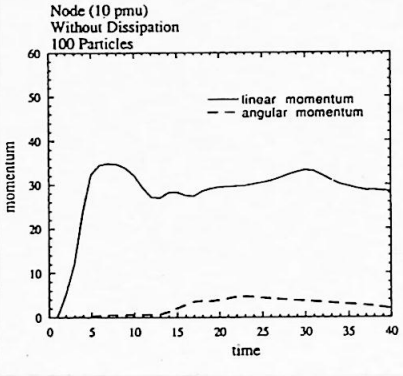

Figs. 25...27: Momentum diagrams to the 100 particle experiments with and without dissipation.

The same experiments (100 particles, started "frozen" from an initial cube of size 2, randomly equally distributed) have also been performed for "high attracting" potentials (1000 pmu) with dissipation ($\delta = 1$, $\sigma = 1$) and without dissipation. The results are shown in Figs. 28...38.

The characteristics of the different geometric dilutions appear stronger as in the case of the "low attracting" calculations. The filament potential attracts clearly higher (Fig. 29a.) than the wall potential (Fig. 28a.) and the node potential (Fig. 30a.). This has been predicted already from the Figs. 1...3. For wall and filament potential, as it has been the case in the low attracting calculations, again it is found that without dissipation the particles distribute over a rather larger area (Figs. 28b. and 29b.). In case of the node (Figs. 30), apparently no difference between the diagrams with and without dissipation in location space is seen [3].

The energy diagrams (Figs. 31...33) are clearly distinct from the pure collapse case (Figs. 34) in contrary to the "low attracting" calculations: The kinetic energy in the case of the wall potential (Fig. 31.) and in the case of the filament potential (Fig. 32.) is no more anticorrelated to the self-energy of the particles. The self-energy still increases in time due to the effect of momentum creation (Figs. 31...33). The effect of dissipation is not as clearly distinct with and without dissipation as was the case in the diagrams for the "low attracting" calculations, but still a difference is visible. In the case of the wall potential, after 20 timesteps (2 dimensionless time units) a quasiperiodic motion sets in. For the filament potential the pulsations due to the initial collapse of the particles also have strongly diminished after 20 timesteps; The energy increase due to momentum creation is higher than for the wall potential. A comparatively high energy gain but a very short period of initial collapse is shown from the diagrams for the node potential (Figs. 33).

The kinetic energy in case of the wall potential is anticorrelated to the potential energy as is demanded by the virial theorem for the wall. The kinetic energy for the filament potential is about constant as is demanded by the virial theorem for the filament. The kinetic energy for the node in case without dissipation obeys the virial theorem for the node. This indicates, that the flow of particles now is due to the background potentials (wall, filament, node) rather than to the potentials of the particles themselves.

If we compare the kinetic energy with and without dissipation, we find for the wall potential that the fluctuations and amplitude of the energy both decrease with dissipation (note the different axis scales of the Figs. 31a. and b.). For the filament potential, we find that dissipation decreases both fluctuations and amplitude of the kinetic energy. In the case of the node potential the amplitude is hardly affected but the fluctuations still are smoothed out by dissipation. We conclude that dissipation smooths out velocity fields and, in case of filaments

[3] I admit that this looks as if the Figures both come from the calculation without dissipation. Unfortunately the data files were lost due to lack of disk space: To verify this assumption would mean to repeat the calculations which, for the lack of time, has not been possible. However, the observations in 3D-space described below are consistent with the the statement that the apparence of the node in location space does not differ (or at least very few).

and walls, cools the flow of particles. In the case of the node potential, instead of cooling the particle flow, the particles collapse adiabatically while maintaining their kinetic temperature.

The momentum diagrams (figs. 35...37) show that momentum creation is damped by dissipation from a factor ~ 2 (node, Figs. 37) to a factor ~ 3 (filament, Figs. 36). This is contrary to the dissipational effect in the case of selfgravitating collapse shown in Figs. 38: In case of the pure collapse, the momentum creation is increased by dissipation insted of decreased (cf. the remark to the collapse experiments in the Appendix).

Again, as in the case of the "low attracting" potentials, the flow of particles has been studied in 3D space in time and was observed in the case of the "high attracting" experiments to be as follows:

Wall The particles collapse rapidly to the center. A ring of enhanced particle density forms. Therefrom the particles are thrown out along the wall. A part of them is thrown out in x-direction (perpendicular to the wall). The magnification shows that the density fluctuates several times (about 5 times), whereby the particles posses high kinetic energy.

Wall Without Dissipation The particles first collapse, then they are thrown out from the center. In the interior of the evolving "shell" the particles again form an overdense center, where the density is less high as before. The magnification shows in the interior a modestly enhanced temperature.

Filament The particles rapidly stream to the center. Some of them are thrown out very early. A spherical overdense region with highly overdense core is forming. The particles stream from the shell to the core. Shortly thereafter, the core throws out particles. Those do not reach the outer region of the now fragmented shell. They recollapse to the interior. The magnification shows that in the interior a collapse center is forming, to which the particles move.

Filament Without Dissipation First, a spherical overdense region is forming. This region is slowly expanding and finally dillutes. The particles gain strongly energy. The magnification shows that there is no collapse center in the interior.

Node The particles form a spherical overdense region. This region pulsates while throwing out particles from its outer regions. The magnification shows a collapse center which is rapidly forming, capturing particles.

Node Without Dissipation The particles contract and expand at once. The kinetic energy is increasing steadily, until a large cloud of rapidly moving particles is forming. The magnification shows, that no collapse center has been formed in the interior.

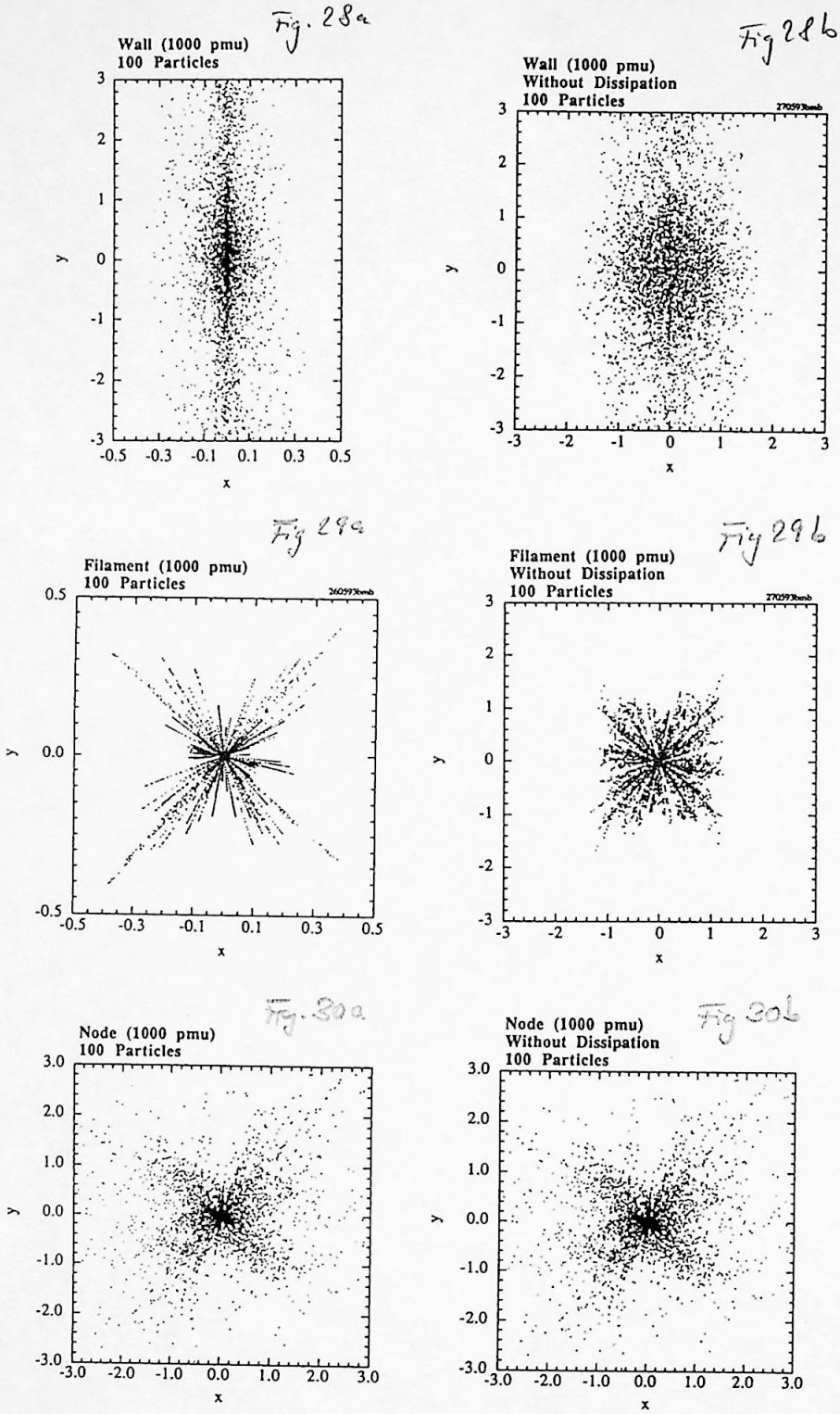

Figs. 28 . . . 30: 100 particle experiments in "high attracting" potentials with (to the left) and without (to the right) dissipation.

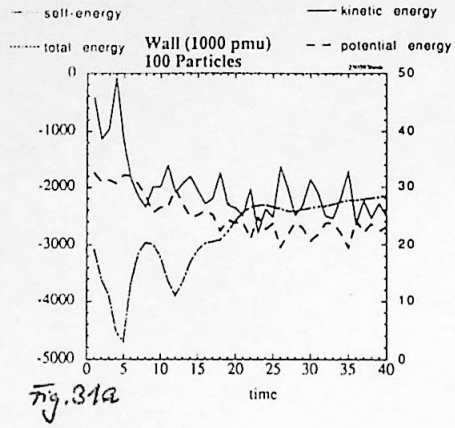

Fig. 31a

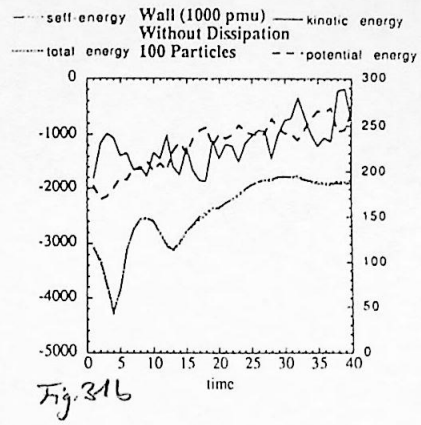

Fig. 31b

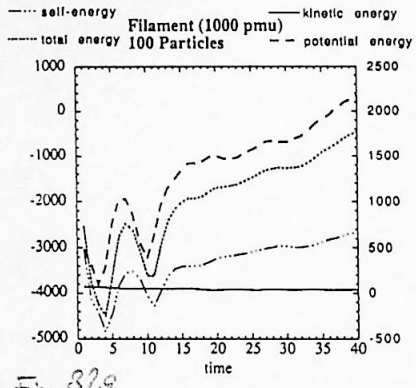

Fig. 32a

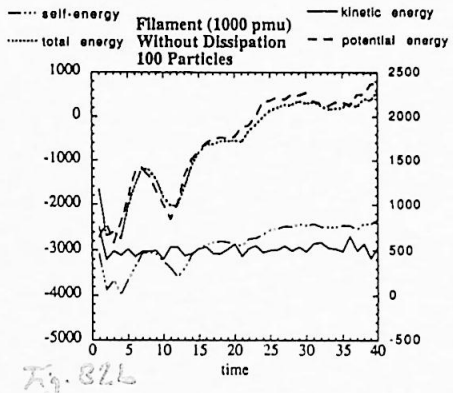

Fig. 32b

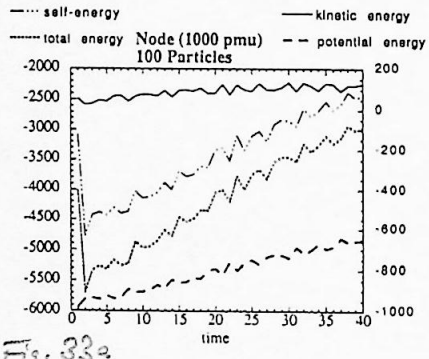

Fig. 33a

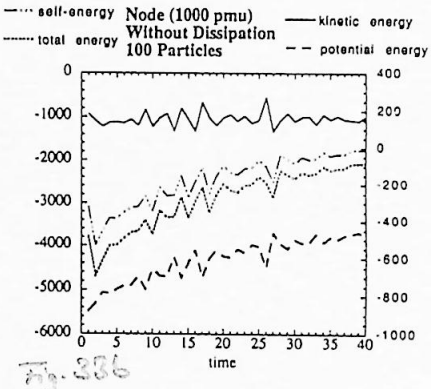

Fig. 33b

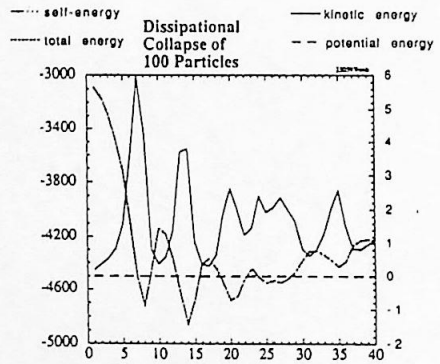

Fig. 34a

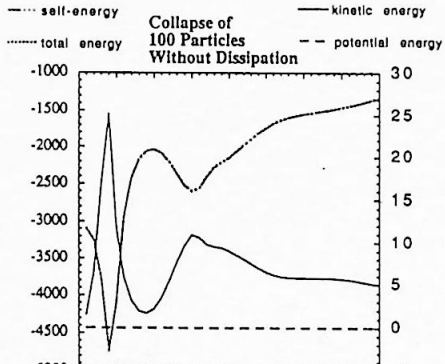

Fig 34b

Figs. 31...34: Energy diagrams to the 100 particle experiments in "high attracting" potentials with (to the left) and without (to the right) dissipation.

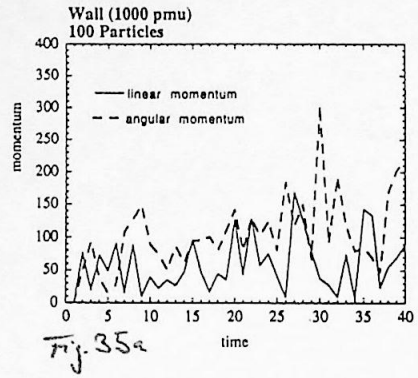

Fig. 35a

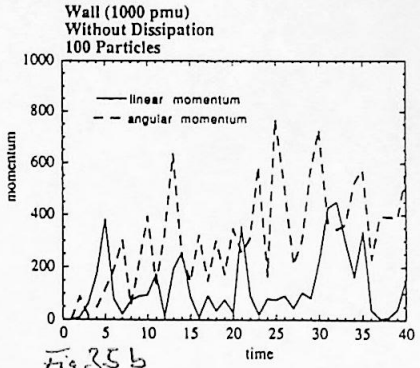

Fig 35 b

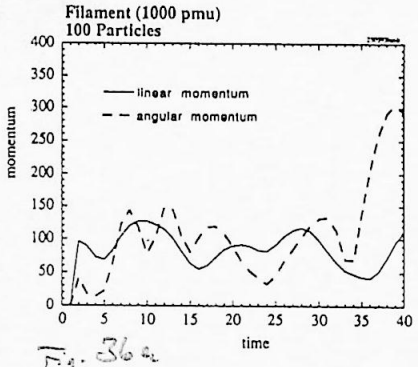

Fig. 36a

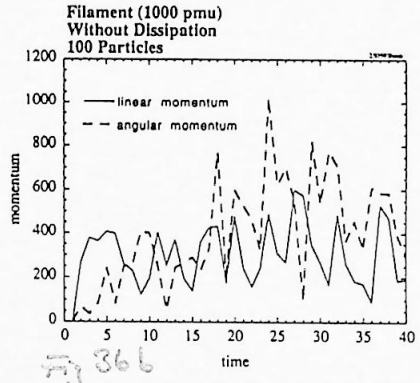

Fig 36 b

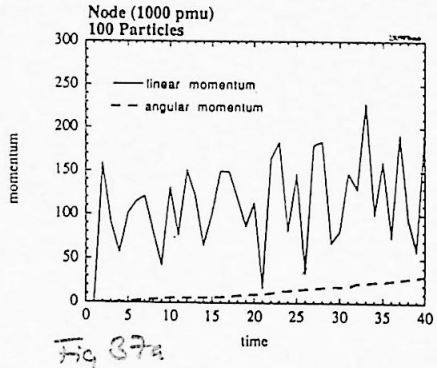

Fig 37a

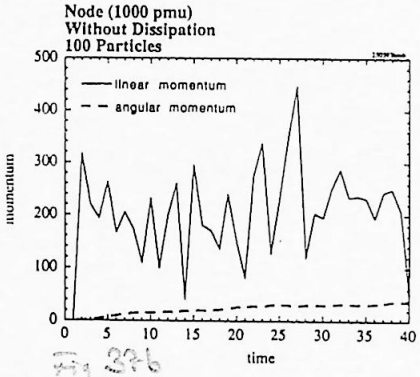

Fig 37b

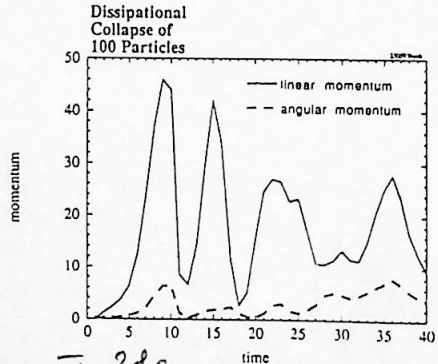

Fig 38a

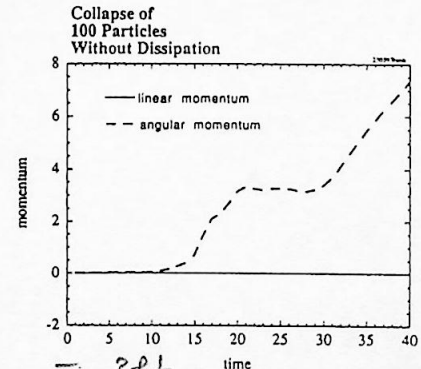

Fig. 38b

Figs. 35...38: Momentum diagrams to the 100 particle experiments in "high attracting" potentials with (to the left) and without (to the right) dissipation.

One of the aims of these experiments is to investigate the effect of dissipation in the different potentials (wall, filament, node) on velocity fields, i.e. the velocity distribution of the particles, a sufficently high number of particles to obtain good statistics is needed. Moreover, as already mentioned to motivate the 100 particle experiments, the number of close encounters between particles is expected to decrease with their total number. The effect of momentum creation therefore can be expected to decrease. For these two reasons, experiments with sample sizes of 1000 particles were performed. In these experiments, the energy loss due to dissipation has been calculated for each timestep (cf. Section 3.2). Experiments with 100 particles are the magnitude limit where direct summation is an effective way of doing N-body calculations. Other techniques (Fourier, Mesh-Code, SPH) then become more effective. For a review on N-body techniques see [Sel87].

A third reason favouring 100 particle experiments concerns the necessity (to obtain "realistic" conditions) to choose the size of the initial starting cube equal to the size of the cube representing the large scale structure. While doing so, in the experiments with 1000 particles the periodic boundary conditions for the first time became effective, suppressing the collapse situation in favour of the background potentials.

The particles again have been started randomly equally distributed (now over a volume of size 100) with initially zero temperature. The velocity distribution has been analyzed for each timestep by multi-channel analysis. Because the initial starting region has increased by a factor 50^3 in comparision to the low attracting experiments whereas the number of particles has only increased by a factor of 10, the dissipational effects were found to be much less dominant in the diagrams. Shown again are the energy diagrams (Figs. 39...41), the momentum diagrams (Figs. 43...45) and, additionally, the velocity distributions at $T = 10$ and $T = 40$ (Figs. 46...48) for wall (top), filament (center) and node (bottom) potential. Further, the energy diagrams for the pure collapse of 1000 particles are shown in the last row of the energy diagrams (Figs. 42).

Both wall and filament potentials show initial pulsations due to the frozen start of the particles. Kinetic and potential energy are anticorrelated due to the virial theorem for the wall in the case of the wall potential and due to the virial theorem for the particles (for the virial of the filament does not contribute) in the case of the filament potential. The energy diagrams for node and collapse are hardly distinguishable. There, the particles collapse in several steps. The kinetic energy therefore increases steadily, as does the differential energy loss due to dissipation. The kinetic energy loss thereby is totally independent from the potential energy. For these diagrams as for the previous ones, the total energy has been calculated as sum of kinetic, potential and self-energy.

The momentum diagrams (Figs. 43...45) again show that dissipation can compensate for momentum creation. Whereas in the cases of the wall and filament potentials the effect of dissipation is hardly noticeable (for the particles are 10 times more far away from each other than in the 100 particles experiments), in the case of the node potential, dissipation smooths out the singular increments of linear momentum linked to the stepwise decrease of self-energy (Figs. 41 and 45).

In all cases, a kinetic temperature of the particles has been calculated (cf. Section 3.2). As the kinetic energy does, it shows that the flow of particles in a wall potential and in a filament potential is strongly perturbed by the pulsations coming from the "frozen" start (Figs. 43 and 44). In the case of the node, the behaviour is clearly unrelaxed: The particles in the node are becoming "hotter" in time (figs. 45).

As it can also seen from the velocity distributions: None of the particle flows reaches thermodynamic equilibrium (LTE) [4] as can be seen from the Figs. 46...48: None of the final velocity distribution (T=40) is maxwellian. The velocity diagrams (Figs. 46...48) later have been replaced by the greyscale plots Figs. 57...59. We will come to them in the next and last experiments.

[4] For the cases with dissipation, thermal equilibrium of course cannot strictly be attained. Since the timescale of dissipational energy loss is assumed to be large, we nevertheless expect an "adiabatic" approach of LTE, i.e. where on small timescales in comparison to the dissipational timescale the flow is almost thermodynamic.

Figs. 39...42: Energy diagrams to the 1000 particle experiments in "low attracting" potentials with (to the left) and without (to the right) dissipation.

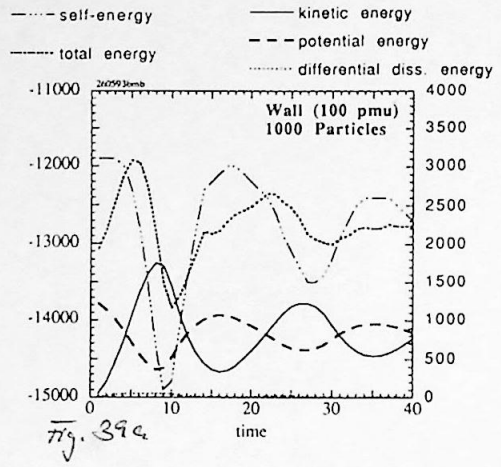

Fig. 39a

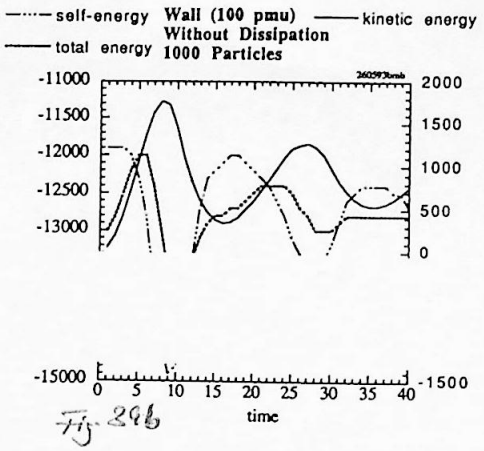

Fig. 39b

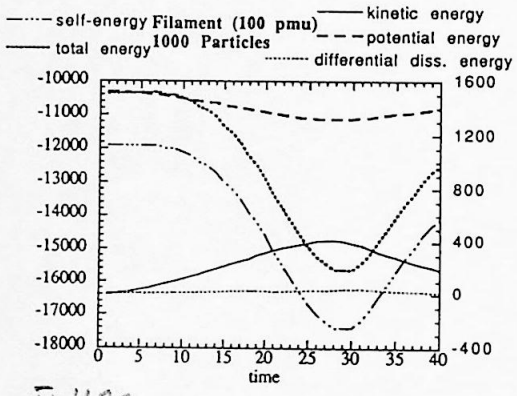

Fig. 40a

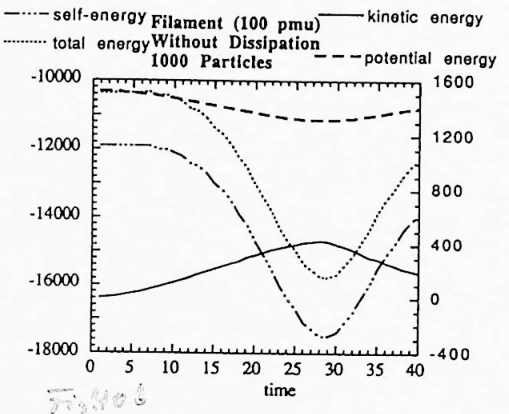

Fig. 40b

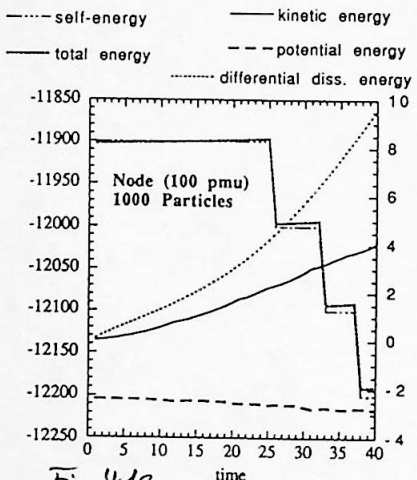

Fig. 41a

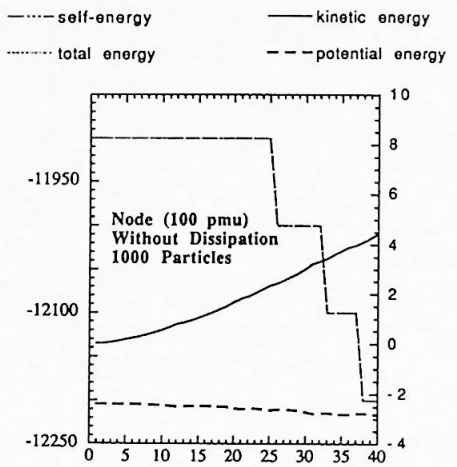

Fig. 41b

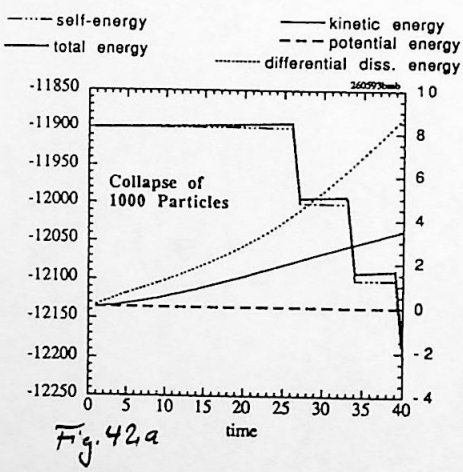

Fig. 42a

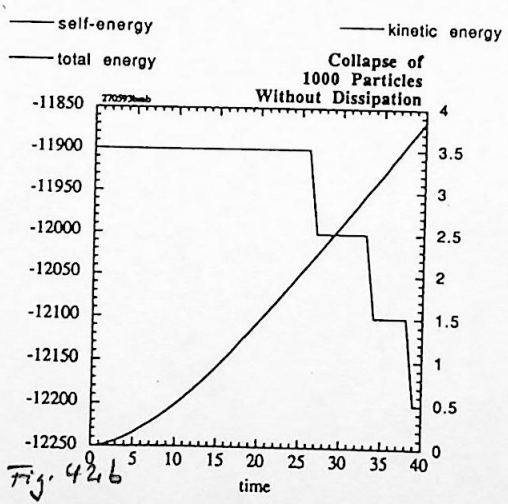

Fig. 42b

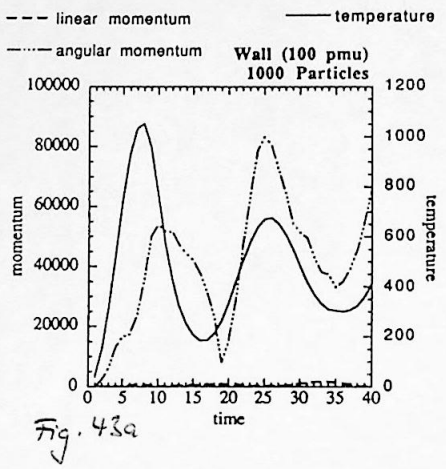

Fig. 43a

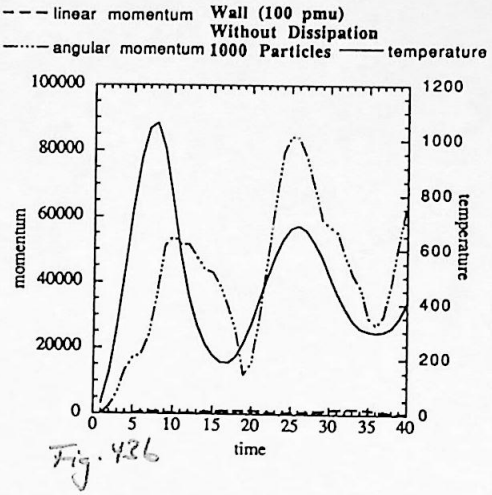

Fig. 43b

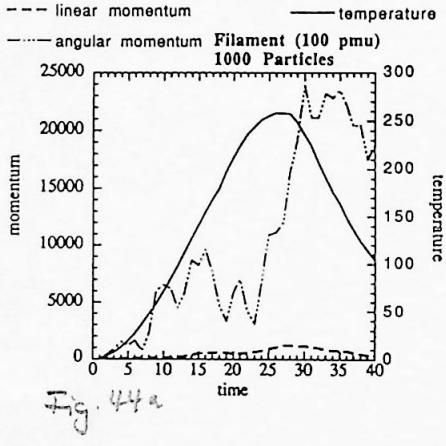

Fig. 44a

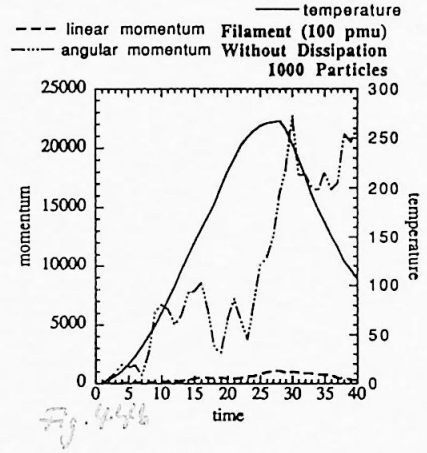

Fig. 44b

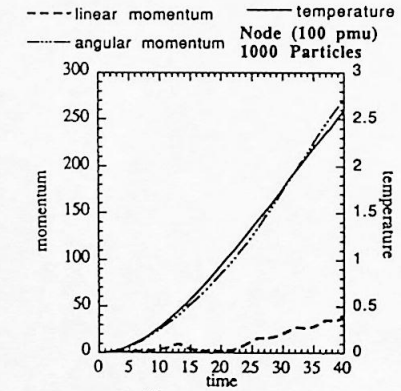

Fig 45a

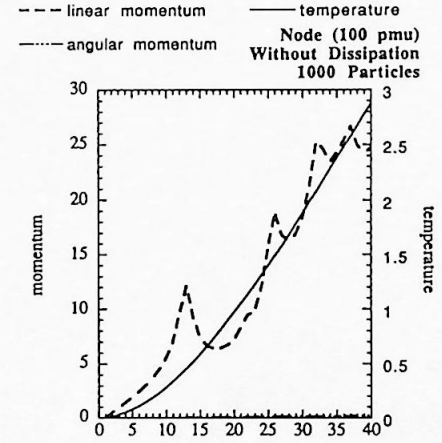

Fig 45b

Figs. 43...45: Momentum diagrams to the 1000 particle experiments in "low attracting" potentials with (to the left) and without (to the right) dissipation.

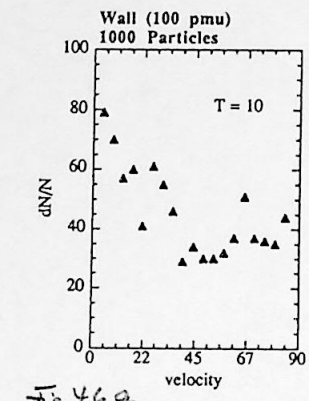

Fig 46a

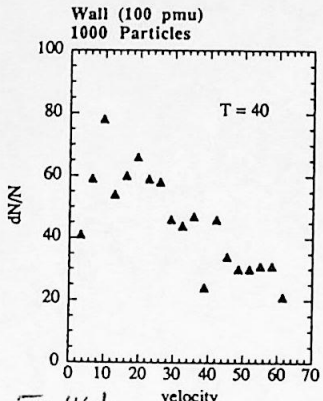

Fig 46b

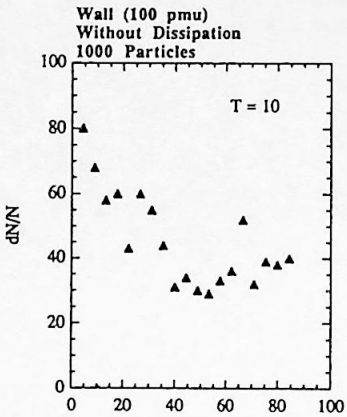

Fig 46c

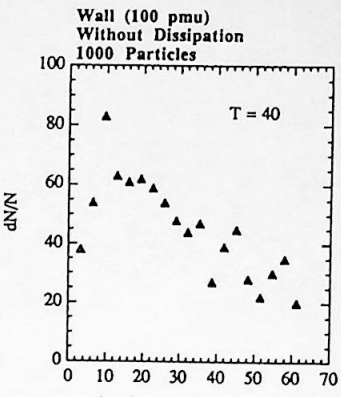

Fig 46d

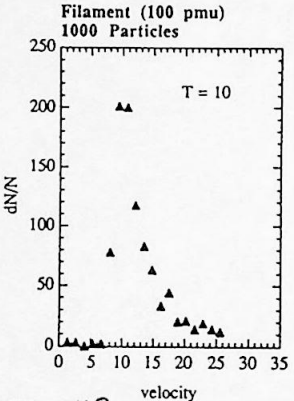

Fig. 47a

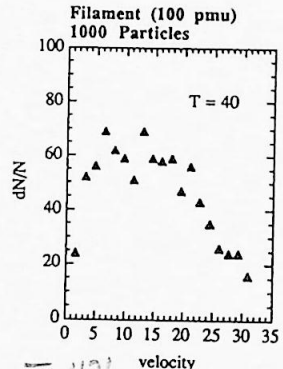

Fig 47b.

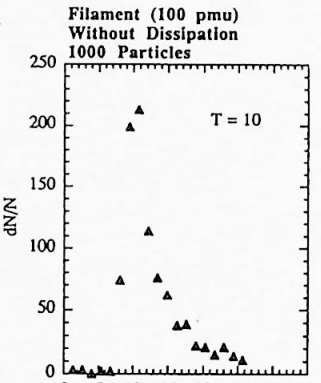

Fig 47c

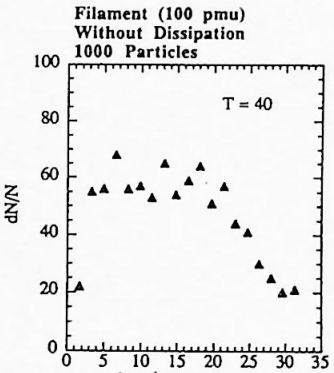

Fig 47d

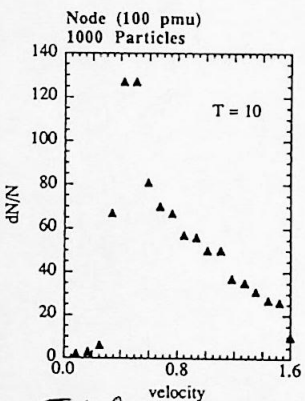

Fig 48a

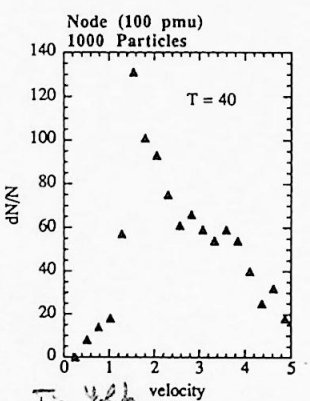

Fig. 48b

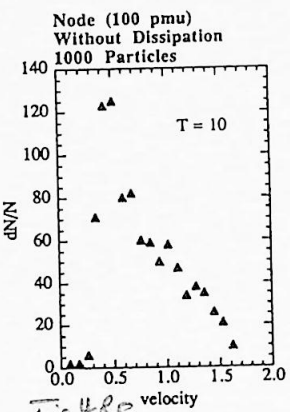

Fig 48c

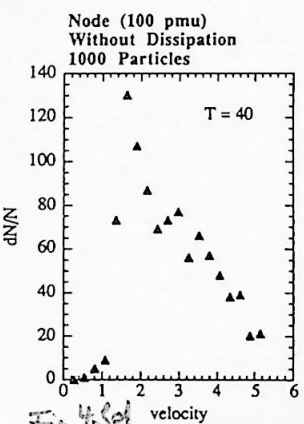

Fig 48d

Figs. ~~39~~ 46 ... ~~42~~ 48: Velocity distribution diagrams to the 1000 particle experiments in "low attracting" potentials with (to the left, 2 columns) and without (to the right, 2 columns) dissipation.

The last experiments

Fig. 49

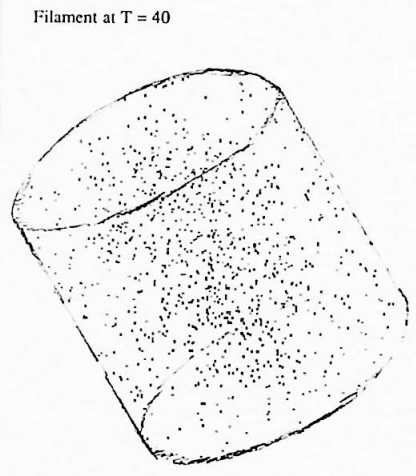

Fig. 49: Distribution of 1000 particles at the end of the calculation of trajectories in a high attracting filament potential. The particles distribute in a cylinder round the filament due to the peculiar dissipation mechanism for the filament described within Fig. 2. The Figure is taken from a 3D visualization of the particle distribution at T=40 (10 Gyr).

4.3 Experiments with 1000 Particles for Different Dissipational Parameters

First 'realistic' experiments with dissipation scaled to galactic halo core sizes (δ) and galactic internal velocity dispersions (σ) have been performed using "high-attracting" potentials to maximize the effects of the geometrically different dilutions (wall, filament and node) versus the selfgravity of the particles. 1000 particles have been started "frozen" (kinetic temperature T=0), equally randomly distributed over a cube of size 100 dimensionless length units (100 Mpc) for different dissipational parmeters (δ, σ). During the calculations, the velocity distribution has been analyzed using multichannel analysis (within 10 channels) and the dissipational energy loss at each time step has been estimated. The total energy for these calculations has been defined as sum of kinetic, potential, self- and cumulative dissipational energy as outlined in Section 3.2.

For the periodic boundary conditions favour the background potentials in comparison to the potentials of the particles, the results are expected to distinguish even more clearly between the different potentials than in the case of the 100 particle experiments.

Depending on the parameters core size δ and internal velocity dispersion σ of the particles, effects already observed in the previous experiments were found.

First consider the three energy diagrams (Figs. 50a to c) for large-core sized galaxies in a background node potential. For low internal velocity dispersion ($\sigma = 1$), dissipation leads to a stepwise increase of the total energy without affecting the kinetic energy ('adiabatic energy increase'). This is assumed to be due to an overestimation of the energy lost by dissipation. For medium internal velocity dispersion ($\sigma = 3.2$), the total energy remains constant, as is expected by its definition. For high internal velocity dispersion ($\sigma = 10$), the total energy even decreases. This is assumed to be due to an underestimation of the energy lost by dissipation. Evidentally, the estimator for the dissipational energy loss does not work well in all cases. The particles are "cooled" by dissipation as can be seen while comparing the kinetic and potential energy in respect to the virial theorem for the node (which is the same, apart from the softening length, as the virial theorem for the potentials of the particles).

Within these experiments, the positions of the particles in phase space at the end of the calculations (T=10 Gyr) have been stored and are shown within the Figs. 51...53. The Figures (51...53) all correspond to calculations with medium core size ($\delta = 0.1$) and medium internal velocity disperion ($\sigma = 10$). But first consider the corresponding momentum diagrams (Figs. 51a....53a.): In the case of the wall potential, the kinetic temperature shows a stochastic process with slightly negative drift (which might indicate dissipation, but is barely present.). The initial "frozen" start has only brief influence on the motion of particles in a wall. The axis scale for the temperature had to be chosen more than 10 times higher than the scale height for the filament potential and even 10^4 times higher than for the node potential. In the case of the filament potential, from the temperature behaviour two contractions of the particles can be deduced. Each contraction therefore is represented by an increase of the kinetic temperature due to the virial theorem of the potentials of the particles (for the filaments

do not contribute to the virial). In the case of the node potential, the kinetic temperature gets two times stepwise enhanced. In between these enhancements, a steady increase with slope dependent on the absolute temperature (cf. Fig. 42a.) is found which indicates a collapse of the particles.

The distribution in location space is clearly more concentrated in the case of the filament potential, as it was argued from the single particle experiments (Fig. 2). The diagrams in location-velocity space represent well the particle flow found in the one particle experiments, studied in Figs. 1...3: The flow in the wall consists of a superposition of different single-particle orbits; The same holds true for the particle flow in the filament. A part of the sample is at rest, distributed overall in the filament (with a slight enhancement towards the center) and modestly attracted by the wall in case of the wall potential. This is not necessarily due to dissipation, since the particle flow, as found from from Figs. 1 and 2, is expected to have naturally a subset of particles nearly at rest. The node potential flow again consists of sinusoidal trajectories which due to the gravitational and dissipational interaction superpose to an excitation of period $L/2$ where $L = 100$ is the size of the considered volume. A part of the particles is at rest. From a dissipational collapse in which the particles finally get stuck at the center one would attend that the particles concentrate in the location-velocity diagram near the center; This is not the case. This again is in total agreement with the location space diagram, where no enhanced density near the center is found [5]. We therefrom conclude that dynamical friction in background potentials is to be expected to influence the flow of particles on large scales, in a different way for each of the different potentials wall, filament and node.

The Fig. 53d. shows that the strong enhancement of the kinetic temperature can be understood as a large scattering of the particles in velocity space (momentum creation); Therefore the kinetic temperature (as well as the kinetic energy) should be interpreted cautiously.

Figs. 54...56 show the energy diagrams for the different potentials wall (Figs. 54), filament (Figs. 55) and node (Figs. 56) for increasing internal velocity dispersion (top to down) and decreasing core size (left to right). In case of the wall potential, the diagrams hardly differ. Only in case of low velocity dispersion and high core size (Figs. 54a.b.d.e.) is dissipational loss of energy due to the "frozen start" visible from the diagrams. In the case of the filament potential, for low internal velocity dispersions and high core sizes (Figs. 55a. and b.), overestimation of the dissipational loss of energy leads to an increase of the total energy over a large timescale. The "bump" found at ($T \approx 10$) is due to biased estimation of the dissipational energy loss. This is not too astonishing in the case of the filament potential, for we have supposed for the estimate of the dissipational energy to work well, the dissipational loss should not exceed magnitudes over one timestep (cf. Section 3.2). This condition is least fulfilled in case of the filament potential. The bump just represents this deficiency of the estimator during the initial collapse. Kinetic and potential energy again

[5] As in the case of the filament potential and wall potential, this does not prove that there is no collapse center, since from the 3D investigations it has been seen that such a collapse center can have the size of a single point

are found anticorrelated according to the virial theorem of the potential of the particles (and for the virial of the filament does not contribute).

The first column of the node potential diagrams was already discussed within Figs. 50. It is show here to a different axis scale, compatible with the other energy diagrams for the node potential. For small and medium core sizes, stepwise increase of kinetic energy can be seen in the diagrams. Since the potential energy is unaffected by this, we suppose this increase to be due to scattering of particles in velocity space (momentum creation). The temperature shown in Fig. 53a. corresponds to the cinetic energy behaviour shown in the center (Fig. 56c.). Neither temperature nor kinetic energy therefore can be taken as a reliable indicator for the global behaviour of the velocity dispersion, which is our next interest.

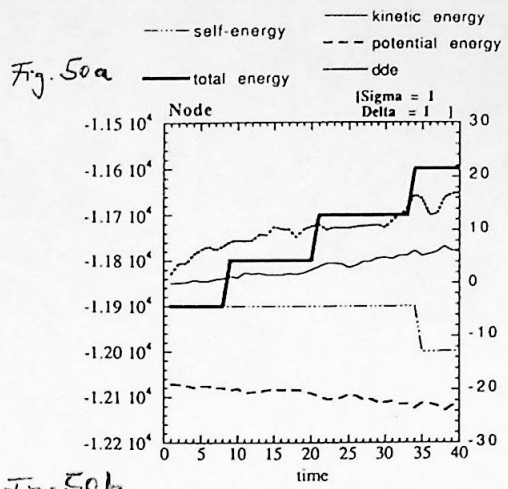

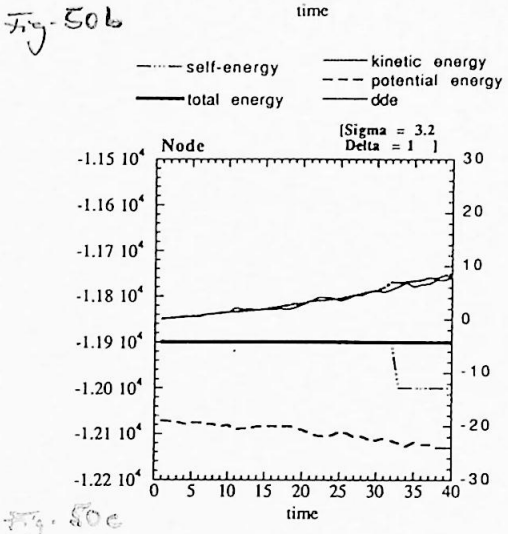

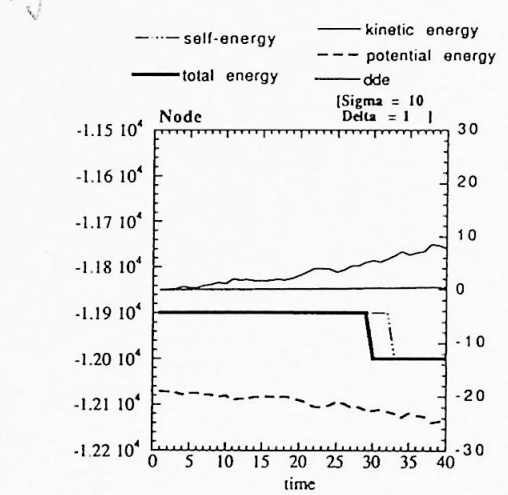

Figs. 50: Energy diagrams to the 1000 particle "high attracting" experiments:
Different effects on the dissipational estimate

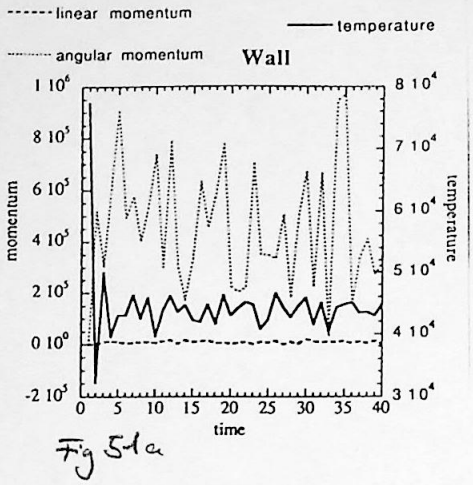

Fig 51a

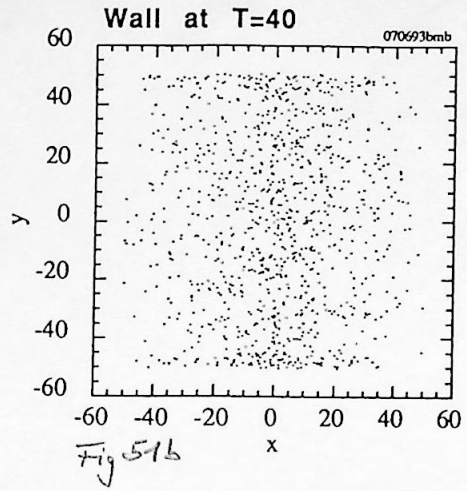

Fig 51b

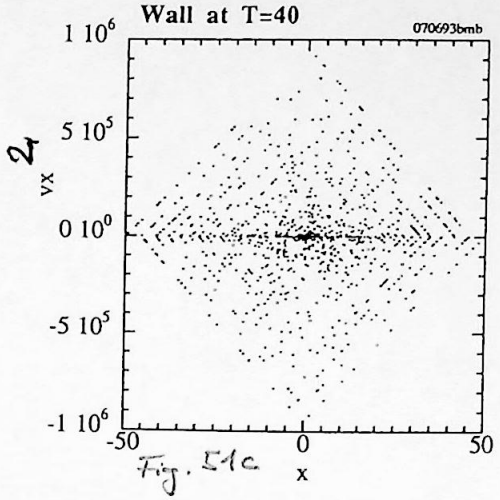

Fig. 51c

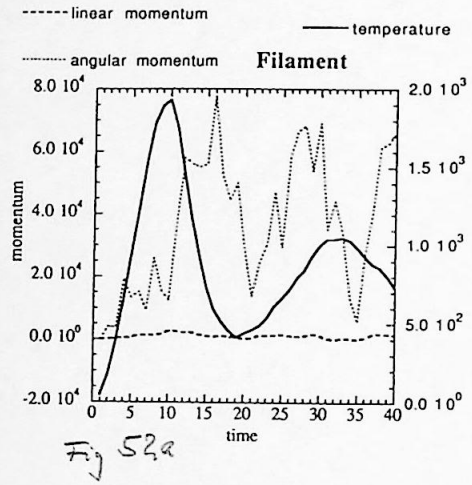

Fig 52a

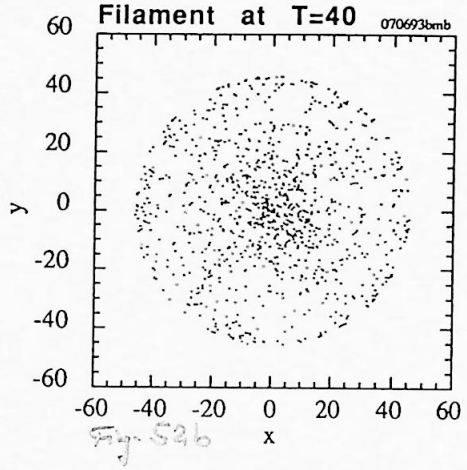

Fig 52b

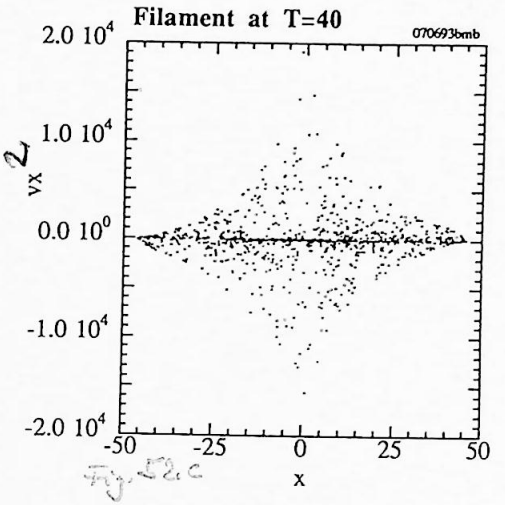

Fig 52c

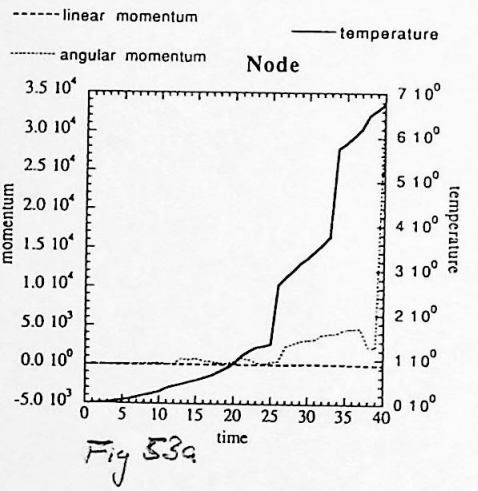

Fig 53a

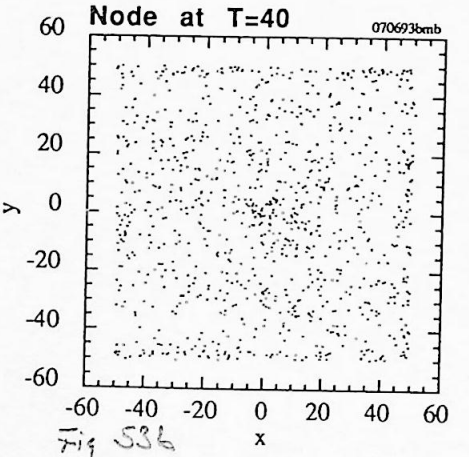

Fig 53b

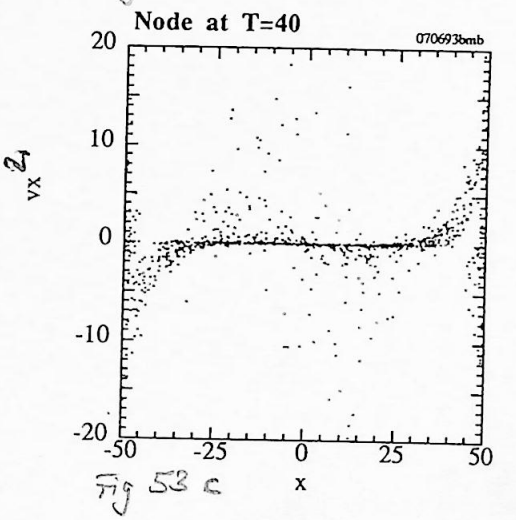

Fig 53 c

Figs. 51...53: Momentum and Phase Space diagrams to the 1000 particle "high attracting" experiments:
Wall, Filament and Node

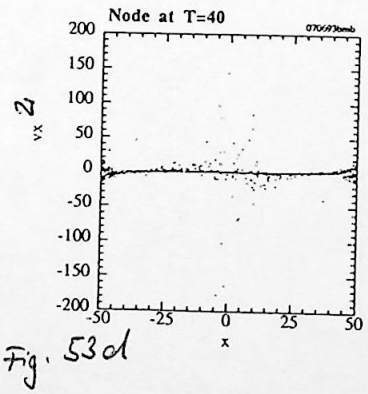

Fig. 53d

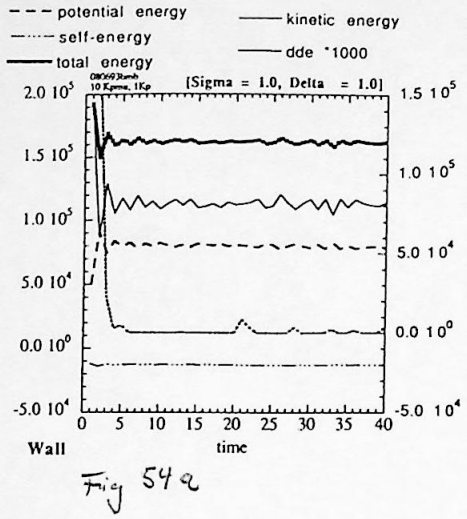

Fig 54a

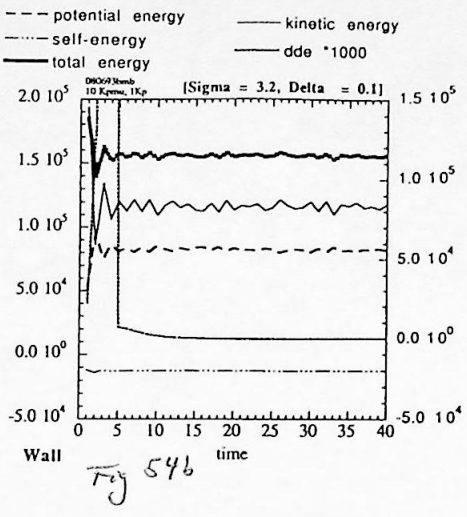

Fig 54b

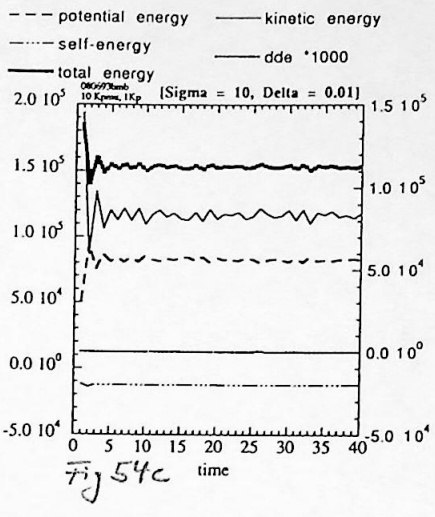

Fig 54c

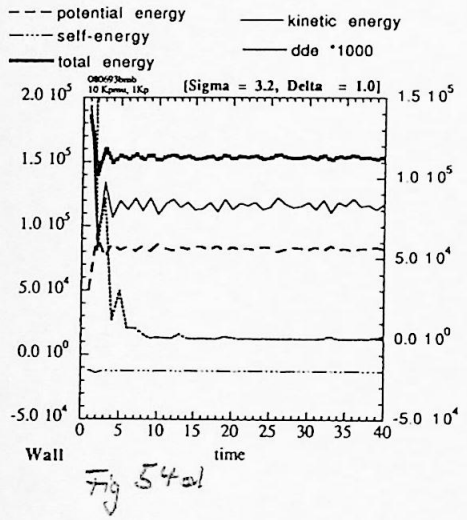

Fig 54d

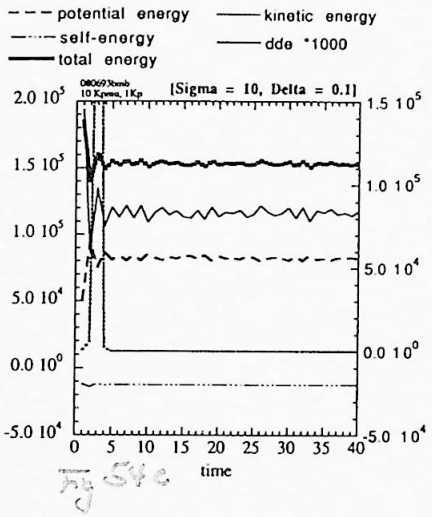

Fig 54e

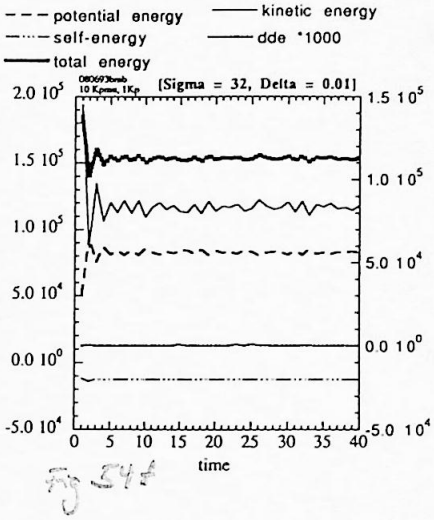

Fig 54f

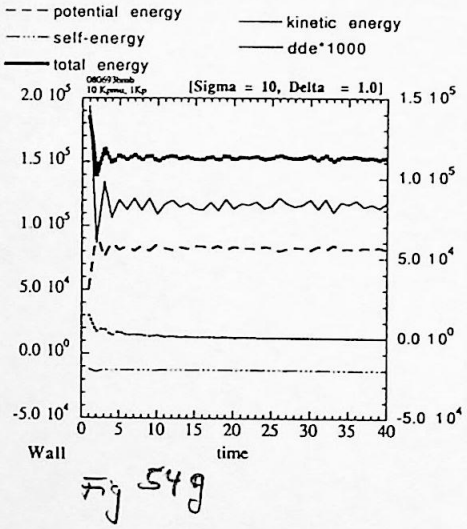

Fig 54g

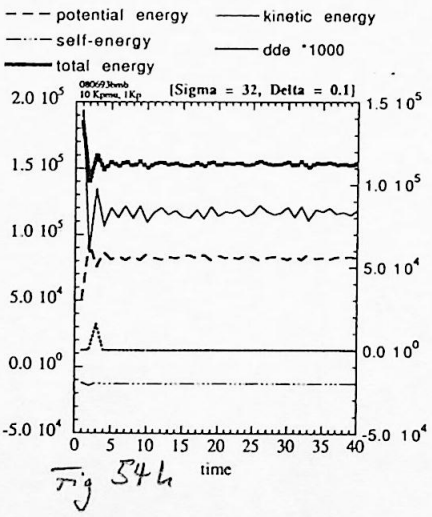

Fig 54h

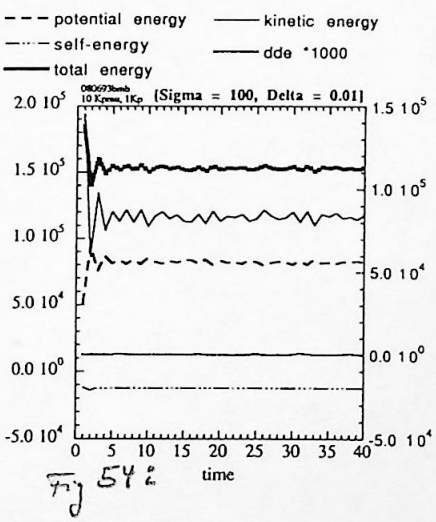

Fig 54i

Figs. 54: Energy diagrams to the 1000 particle "high attracting" experiments:
The Wall

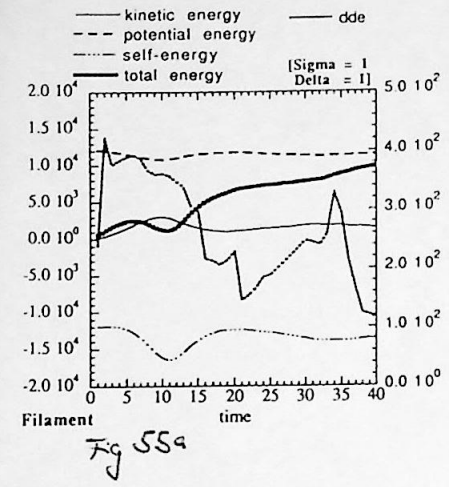

Fig 55a

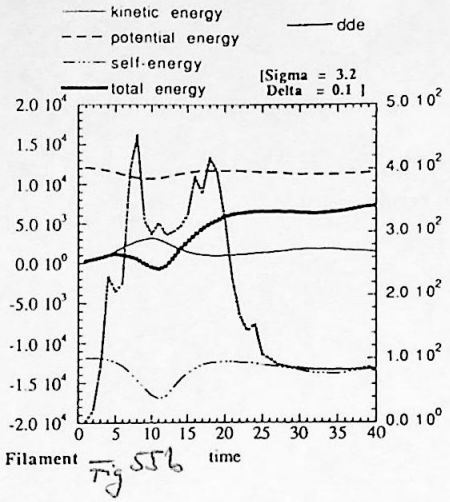

Fig 55b

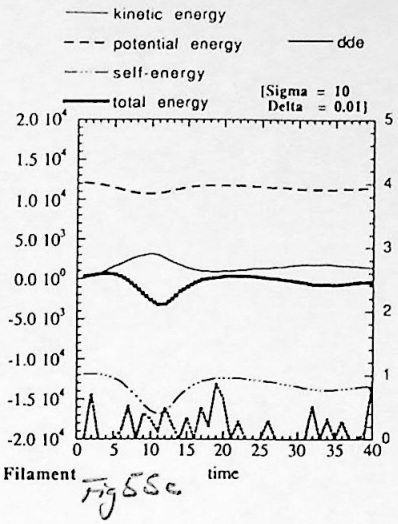

Fig 55c

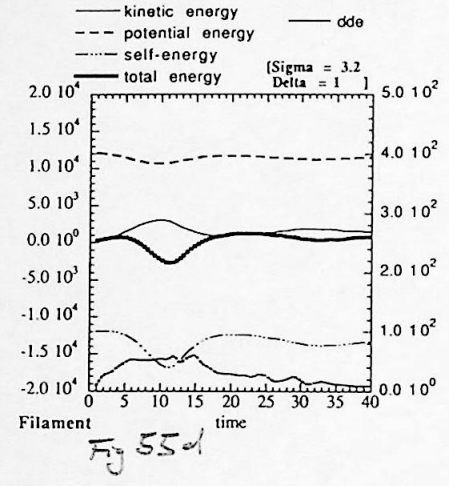

Fig 55d

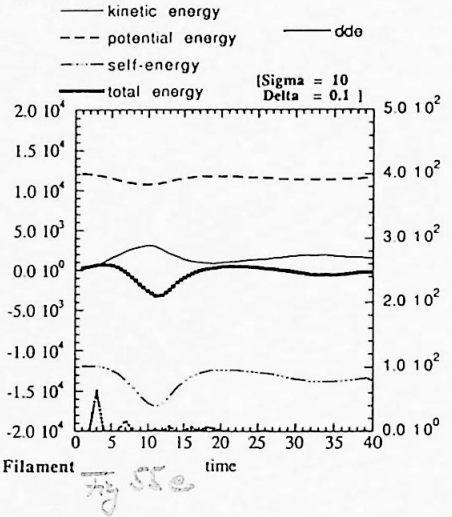

Fig 55e

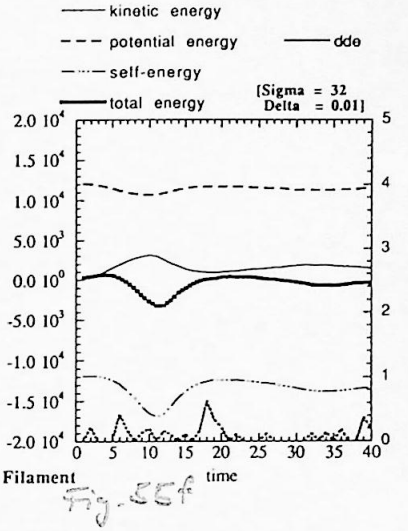

Fig 55f

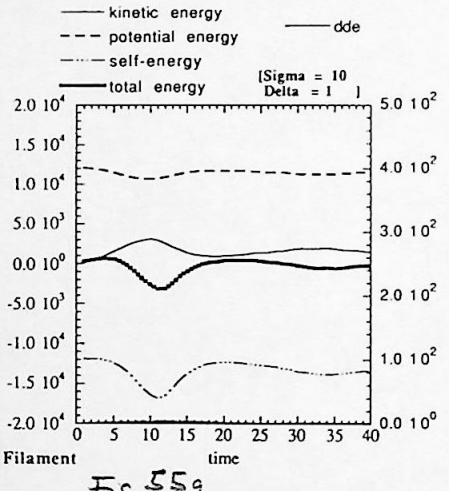

Fig 55g

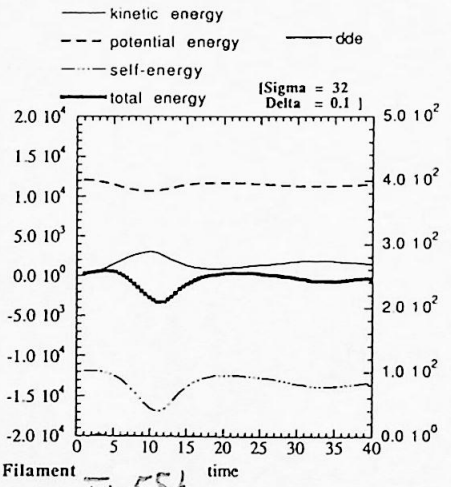

Fig 55h

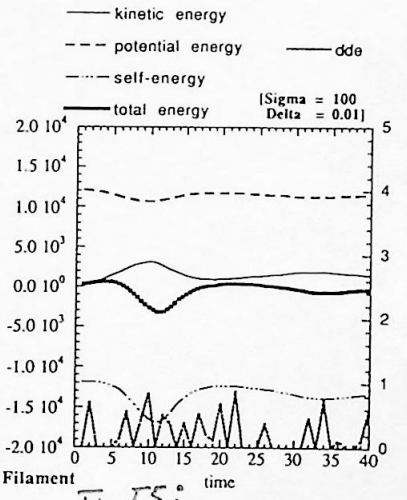

Fig 55i

Figs. 55: Energy diagrams to the 1000 particle "high attracting" experiments:
The Filament

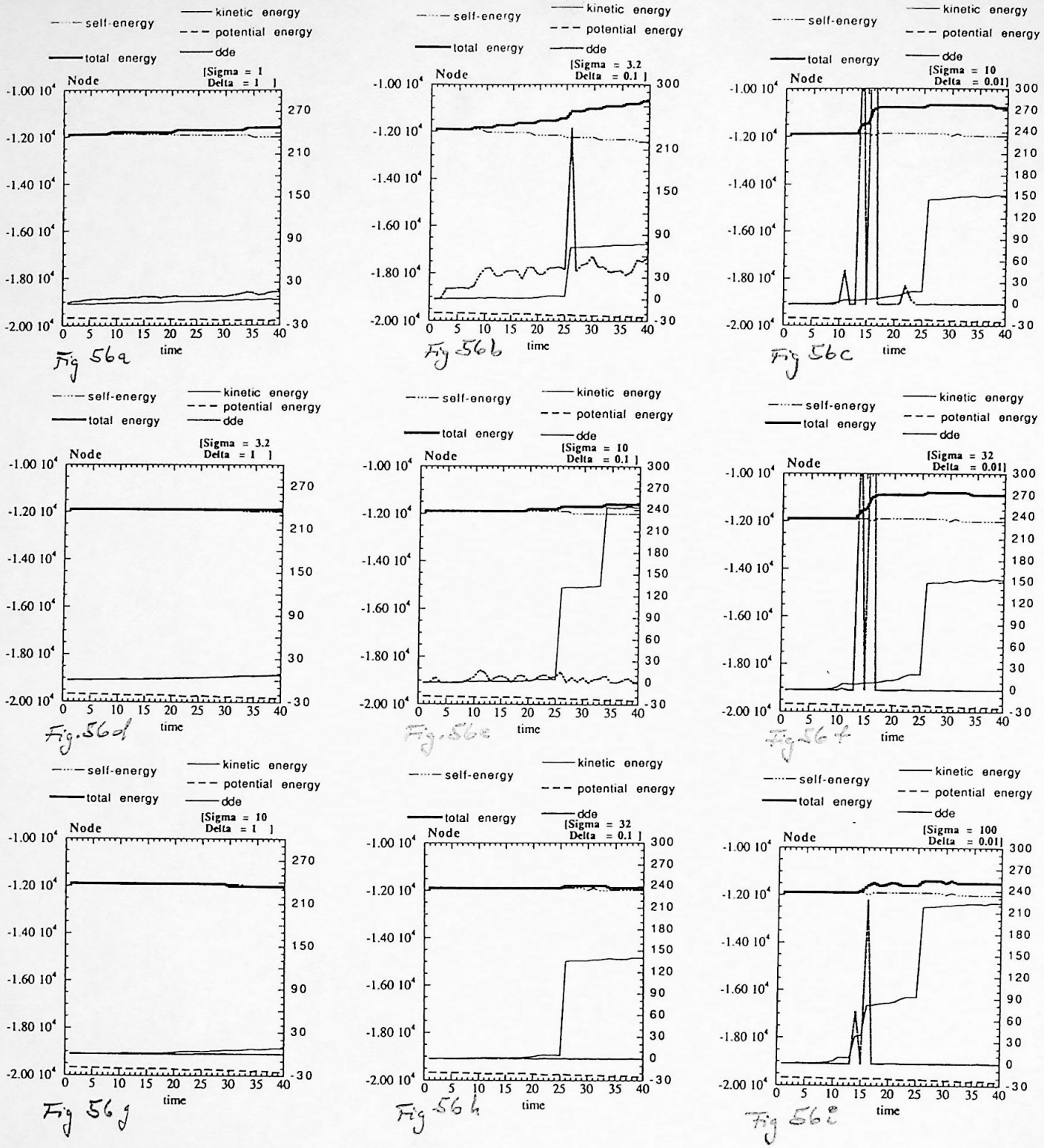

Figs. 56: Energy diagrams to the 1000 particle "high attracting" experiments:
The Node

The velocity distributions corresponding to the flow of particles in the different potentials are shown in Figs. 57...59 for the wall potential (Figs. 57), the filament potential (Figs. 58) and for the node potential (Figs. 59) arranged to decreasing internal velocity dispersion (from left to right) and decreasing core size (from top to bottom). Horizontally, the velocity axis runs from $1...500$ $[v_u]$ in the case of the wall potential, from $1...100$ $[v_u]$ in the case of the filament potential and from $1...5$ $[v_u]$ in the case of the node potential. Recall that one dimensionless velocity unit $[v_u]$ was scaled to 25 km s^{-1}. So the diagrams represent velocity distributions up to 12500 km s^{-1} for walls, up to 2500 km s^{-1} for filaments, and up to 125 km s^{-1} for nodes in the Universe.

The diagrams have been performed while two times applying a box-smooth procedure (which smoothes over a box of given size cf. Appendix) and a applying a contour-fill procedure afterwards. The number of particles found in a channel of the discretised velocity distribution is represented by a greyshade scale. Each second contour line is labeled with its actual number of particles that is represented by the enclosing contour. The white regions represent more than 120 particles per channel. Therefrom the greyshade goes down by a number of 30 particles per channel per shade-increment.

The plots in case of the wall potential do hardly differ from each other. The bright islands appearing periodically indicate the underlying stochastic process which was already concluded from the temperature behaviour. In the plots for the filament potential, the two pulses coming from the starting conditions can be resolved in time in velocity space. The second pulse can be seen as due to the reexpansion of the particles, as it was already observed in the 3D investigations within the 100 particle experiments. The different dynamical friction parameters core size and internal velocity dispersion hardly affect the shape of the flow.

This does entirely change in case of the node potential: There, the particles are found to be decelerated in time depending on the dissipational parameters core size and internal velocity dispersion. From the diagrams we conclude that the velocity distribution is more peaked near zero in case of low core size and high internal velocity dispersion than in case of high core size and low internal velocity dispersion. So, if one would observe on a large scale in a background node potential a relatively high amount of galaxies with low propper velocity against the background moving sample, therefrom a rather low core size [6] and high internal velocity dispersion of the individual galaxies could be expected.

[6] E.g. few or no brown dwarfs distributed in the halo.

Figs. 57: Velocity distribution greyscale plots to the 1000 particle "high attracting" experiments:
The Wall

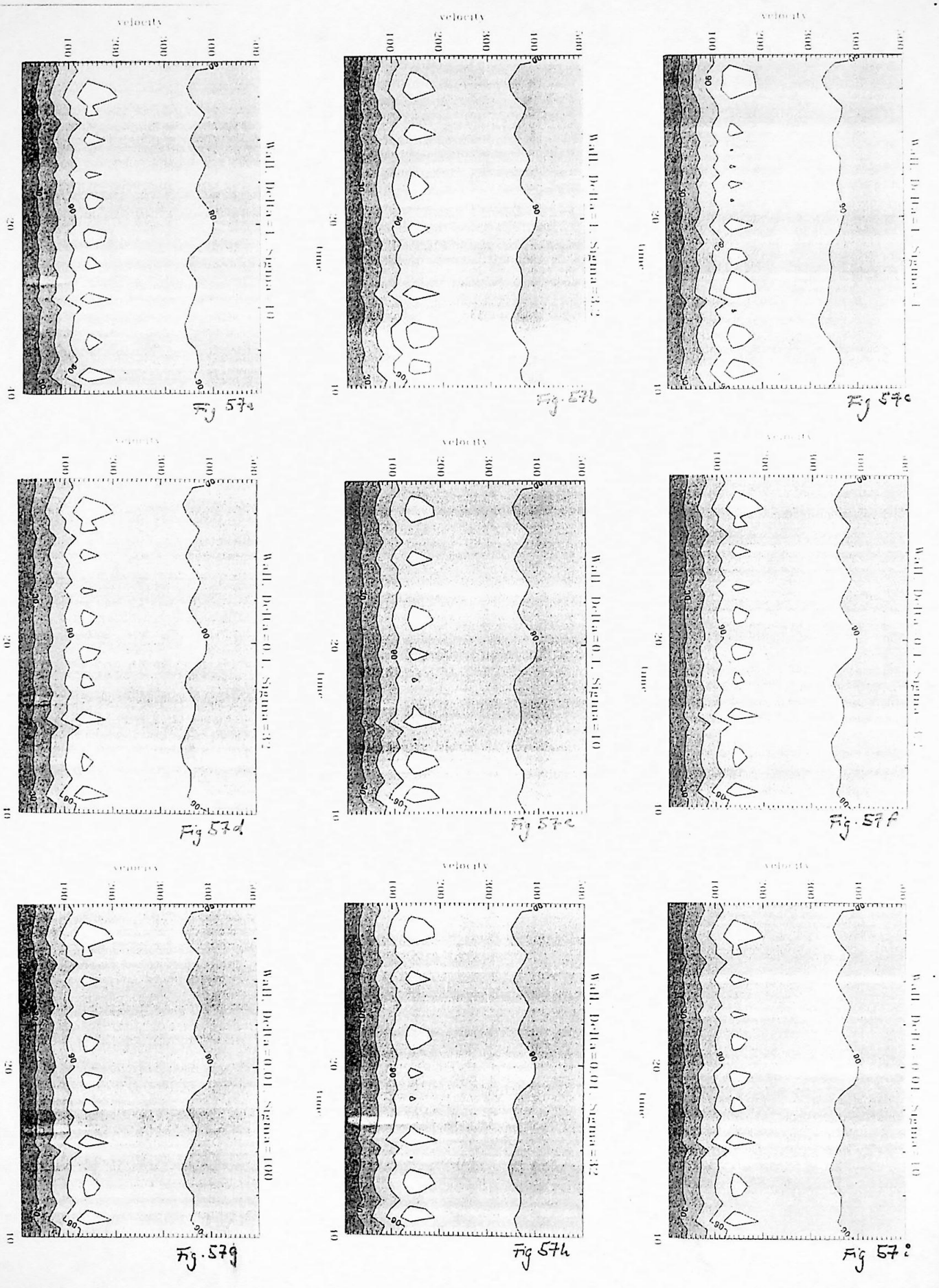

Figs. 58: Velocity distribution greyscale plots to the 1000 particle "high attracting" experiments:
The Filament

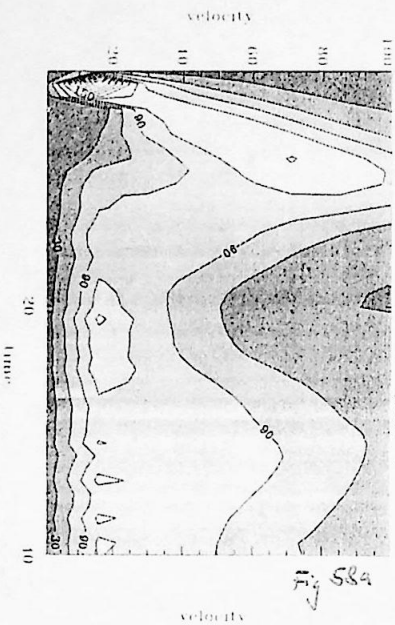

Fig 58a

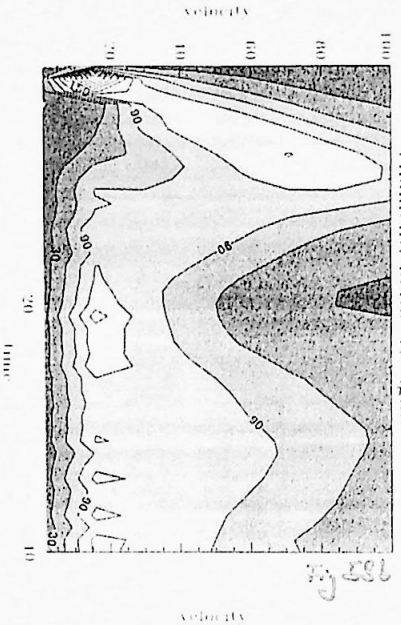

Fig 58b

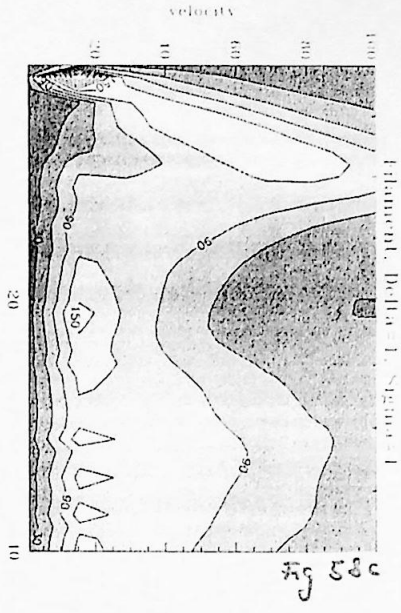

Fig 58c

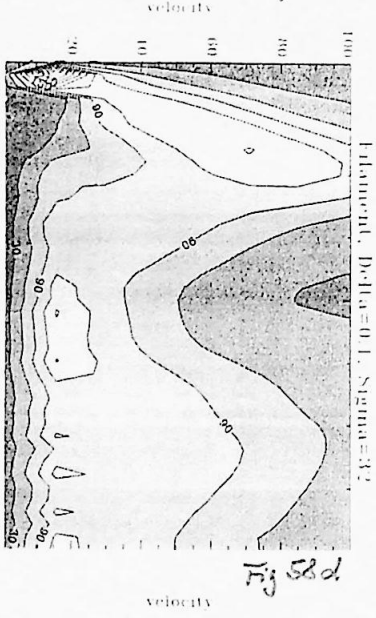

Fig 58d

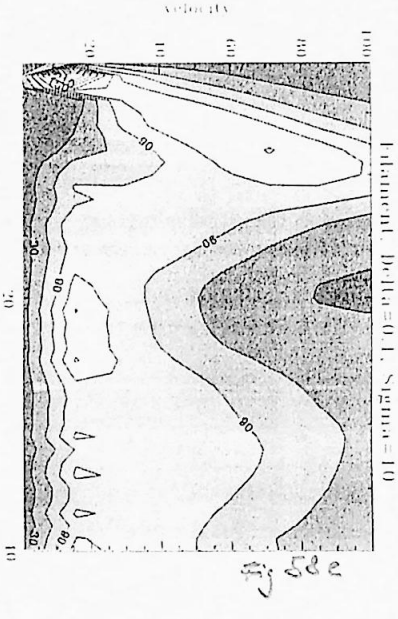

Fig 58e

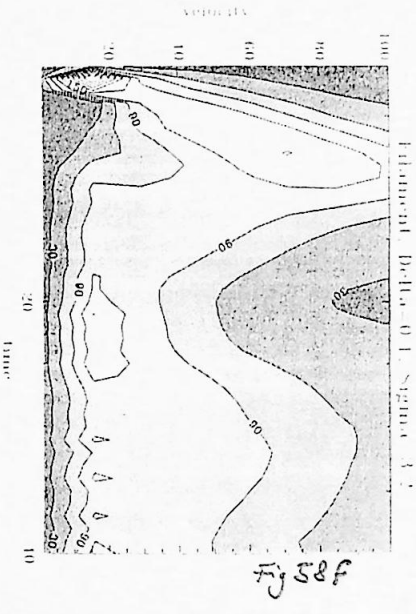

Fig 58f

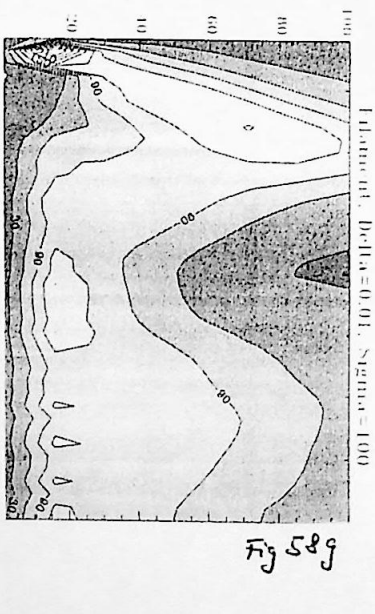

Fig 58g

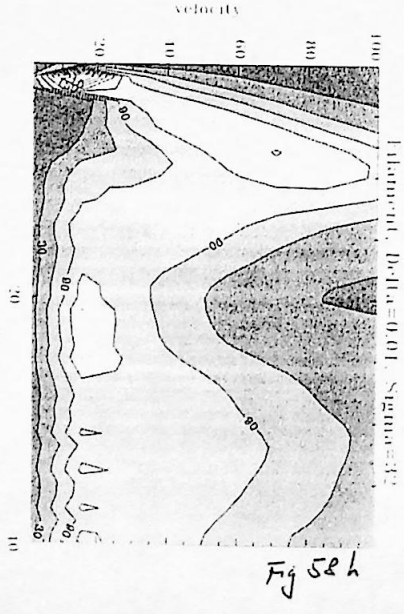

Fig 58h

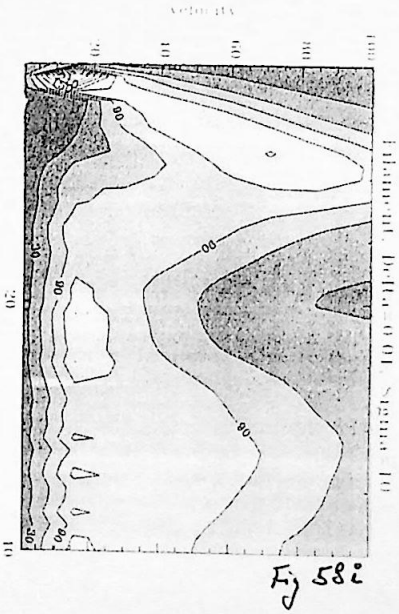

Fig 58i

Figs. 59: Velocity distribution greyscale plots to the 1000 particle "high attracting" experiments:
The Node

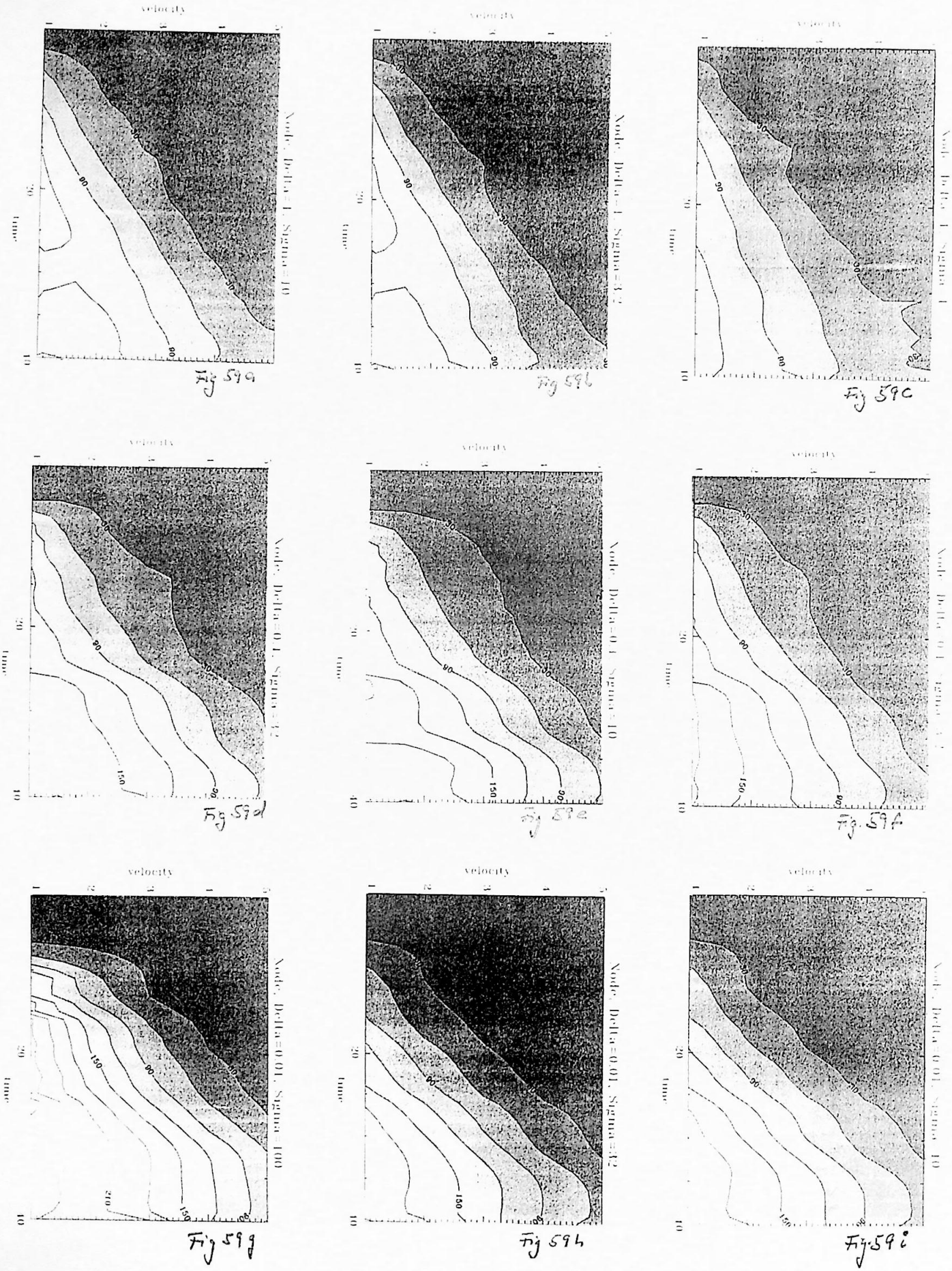

It would still rest a lot of improvements to do for these experiments, until one could also go into more sophisticated investigations while studying the effect of a time varying force-law [Dam90] on the velocity distribution of galaxies in our Universe.

Chapter 5

Summary of the Results and Outlook

5.1 Summary of the Results

The three dimensional motion of model galaxies with varying degrees of "stickiness" in topologically different background potentials has been studied. This has been done using an N-body code which therefore has had to be developed and tested.

The results of the computations have been analyzed in phase-space, 3 dimensional in time and, to separate out numerical effects due to the N-body algorithm used, the energy and momentum behaviour of the flow of the particles has been investigated:

1. In the case of dissipation, the creation of momentum in N-body direct summation codes was found to be partially canceled by the dissipational loss of energy. Within the N-body model, the dissipation therefore has to be regarded as process in competition with momentum creation.
2. We concluded from the phase space analysis that dynamical friction in background potentials is expected to influence the flow of particles on large scales, in a different way for each of the different potentials (wall, filament and node) correspondant to the linear dependency of kinetic energy in the case of a particle approaching the wall, the exponential dependency of the kinetic energy in the case of a particle approaching the filament and the sinusoidual dependency of the kinetic energy in the case of a particle approaching the node potential.
3. From the fluctuation and the drift on the kinetic energy behaviour in case of the 100 particle experiments we conclude that dissipation smooths out velocity fields and, in the case of filaments and walls, cools the flow of particles.

4. Filament potentials were found to attract orbits of particles more strongly than wall potentials or node potentials.
5. From the velocity distributions of particle flow for different dissipational parameters (core size and internal velocity dispersion of galaxies) we concluded that dissipational effects are most likely to be seen in background node potentials as they are the clusters of clusters of galaxies on the scale considered (100 Mpc). There we predicted for especially for low core sizes and high internal velocity distributions of galaxies a comparatively high amount of galaxies to move only slow in comparison to the background.

In a more comprehensed form, the resulting figures had to be reduced to just the last ones which show the main conclusions most clearly. However, since this work as a stage is not ment to be published, I have shown more figures than one ordinary should.

5.2 Outlook

One severe problem still is the large amount of energy created. For the lack of time it has not yet been investigated (despite of this being an absolute fundamental test) whether the creation of energy can totally be explained by momentum creation. Within the planet experiments the energy creation did not appear as severe but within the 100 particle experiments the effect of energy creation must be expected to perturbe the trajectories of the particles strongly. As already emphasized, the accurate determinition of the trajectories is of high importance for an accurate determination of the energy lost by dissipation. The investigation of energy creation is still under way.

The results of these computations may serve as input on future one-dimensional calculations on the CMBR constraints obtained from the satellite COBE.

Oh ! chez moi, dit le petit prince, ce n'est pas très intéressant, c'est tout petit. J'ai trois volcans. Deux volcans en activité, et un volcan éteint. Mais on ne sait jamais.
– On ne sait jamais, dit le géographe.

Appendix A

Data Creation and Analysis

A.1 Description of the N-body code

An N-body code has been written to allow the calculation of particle trajectories in a background potential, including dynamical friction. The code consists mainly of two algorithms: The Bulirsch-Stoer algorithm and the algorithm to evaluate the forces acting on the particles.

To solve the equations of motion of model-galaxies in a given potential, the Bulirsch-Stoer algorithm [Pre86] has been used . This algorithm introduces two different steps in the independent variable (the time): A global timestep, which has been chosen to be 0.1 dimensionless time units (250 Myr) and a substep dependend on the error criterion of the algorithm. The error criterion has been used as set to default by Press et al. with the algorithm constants EPS = 10^{-8}, HMIN = 10^{-18} and H1 = 10^{-12} (double precision). For a description of the error criterion and the algorithm constants see Press et al.

The evaluation of the forces acting between the particles has been done by a simple direct-summation procedure. Also the dynamical friction has been evaluated in direct summation once for each global timestep.

The Bulirsch-Stoer algorithm first has been tested in one dimension for one particle, using different potentials (r^2, r, $\log r$ and r^{-1}) and including friction linear in velocity. Then it has been expanded to do the calculation of 3 dimensional trajectories of N particles.

The Bulirsch-Stoer method is described in detail by Press et al. [Pre86]. It is based on an extrapolation of the step size in the independent variable (the time) to zero, therefore is promised to convert "lead to gold" (after Press et al.). The behaviour of the algorithm nevertheless has been tested in the case of more simple experiments. The tests also are described in this Appendix.

The N-body code has been written in FORTRAN 77 and has been executed on the SUN workstations of Leiden Observatory. Input parameters (constants for the Bulirsch-Stoer algorithm, friction parameters, initial condition parameters and output formatting parameters) have been provided using parameter files

which in turn allowed reliable documentation of the experiments: All output of the program has been stored together with the corresponding input parameter file, so every program run could be examined with respect to the parameters actually used.

As initial conditions for the experiments, a starting cube and a temperature of the galaxies has been set. In all experiments shown in this work, the initial temperature has been set to zero ("frozen" start). However, the program provides an initial maxwellian velocity distribution using the Box-Műller procedure [Hon90] which generates Gaussian distributed random numbers by coordinate transformation (cf. source code) from equally distributed random numbers. The initial locations all have been equally distributed. As randomizer, RAN1 from [Pre86] has been used. This procedure allows controlled and machine-independent randomizing, which means that every program run has been reproducible and did only depend on the input parameters. The trajectories of galaxies have been restricted to periodic boundary conditions. These were taken in account as well as for the calculation of the trajectories as for the evaluation of the viscosity term as for the evaluation of the gravitational forces acting between the particles. The complete phase space information, i.e. the velocity distribution of the particles, a kinetic temperature, momenta, the mean kinetic and potential energy, the self-energy and the differential dissipational energy and algorithm-control variables have been evaluated for each global time step of the algorithm and were written into Ascii-files, dependend on the experiments performed.

A.2 The Source Code

In the following, for the sake of verifiability, the source-code is presented. Additionally, a typical standard input parameter file is appended at the end.

```
      program ls
*=============================================================
*     Large Scale Structure and Dissipation                  *
*     (c)1993 Bernd Mueller-Bierl                            *
*=============================================================
*     options                                                *
*     f77 -xld -C ls.for creates a test version              *
*     f77 -r8 ls.for     creates the double-precission version
*=============================================================
*     The program reads data from the parameterfile <set.par>*
*     and executes an N-Body calculation.                    *
*=============================================================
*     if icVal in the parameter list is .GT. 0, the first icVal
*     galaxies are given initial locations and velocities from
*     the file <ic.par>
*
*     Output is written on:
*
*         <ens.dat>: rows with  x,y,z of positions
*         describes the position in Gamma space
*                                        NGAL rows/sweep
*          <ps.dat>: rows with  x,v_x*v_x,y,v_y*v_y
*                                        NGAL rows/sweep
*        <vdis.dat>: rows with  v_abs  #galaxies
*         velocity dispersion (not normalized)
*                                        canal rows/sweep
*          <enj.dat>: rows with  E_kin, E_pot, EpotSG, Edis, Etot,
*                                LinMom, AngMom, Temp
*         energy and momentum bilance
*                                        1  row/sweep
*         <dump.dat>: rows with  NOK, NBAD, ADDRS
*                  contains the Bulirsch-Stoer algorithms' efficiency
*                  and the viscosity force for each galaxy and timestep
*                  comments to program-stop are written here
*                                        NGAL rows/sweep
      implicit logical(A-Z)
*                                        latest revision: 28.5.93
      Integer NVAR, NMAX, MAXGAL, NGAL
*             NVAR:   Number ODEqs.
*             NMAX:   max. Number ODEqs.
*             NGAL:   Number of Particles (Galaxies)
*             MAXGAL: max. Number of Particles
*          WARNUNG: Diese Zahlen stehen als Konstanten in
*          fast allen Unterprogrammen und dienen dort der
*          Felddimensionierung.
      Integer canal
*             number of channels for the velocity analysis
      Integer Gal
*             running index of galaxies
      Real SigmaG, DeltaG, Lambda, Rcutof
*             friction parameter of galaxies
      Real Rcut2, SGs2
*             Cutof: parameter for selfgravitation
*             SGs2 : parameter for softening
      Real    Tstart, Temp
*             Tstart: initial kinetic temperature of the galaxies
*             Temp:   kinetic temperature of the galaxies
      Integer NX2
*             NX2 describes the number of equal time steps
*             (sweeps) of length  Delta = X2-X1
      Integer icVal
*             describes the number of initial conditions
*             which are defined by the file ic.par
*             all other galaxies are set according to SETICD
      Real b2(5)
*             softening parameter for the potentials
      Parameter(NVAR=12,NMAX=12,MAXGAL=1000)
      Integer KMAX,KOUNT,NNOK,NOK(MAXGAL),NNBAD,NBAD(MAXGAL),IDUM
      Integer I,ios
*             NOK:  Number of sucessful steps
*             NBAD: Number of unsucessful steps
```



```
*                   for the GAL'th Galaxie
*             IDUM: initialisation of the randomizer
*             ios:  IO error flag
      Real    Edis, Tdis
*             Edis: Energy lost by Dissipation (evaluated each sweep)
*             Tdis: cummulative energy lost by Dissipation
      Real    DXSAV, XP(200), YP(10,200), Ystart(NVAR), Yold(NVAR)
*             see Press et al.
      Real    Yens(NVAR,MAXGAL)
*             ensemble of galaxies
      Real    ADDRS(MAXGAL),ADD3RS(3,MAXGAL)
*             add right side: viscosity parameter of the GAL'th galaxie
*             rsp. the gravitational force acting on it
*             (to be added to the right side of the eqs. of motion)
      Real    PS2D(4,MAXGAL),VDIS(2,20),MEpot,MEkin,EpotSG
      Real    LinMom, AngMom
*             PS2D:   projected phases space
*             VDIS:   velocity distribution
*             MEpot:  potential energy due to potential
*             EpotSG: selfgravity (potential) energy of particles
*             MEkin:  kinetic energy
*             LinMom, AngMom: linear and angular momenta
      Real    X1,X2,Delta,EPS,H1,HMIN
*             see Press et al. (Delta=X2-X1)
      Real    size, Icube(3,4), mGal
*             size:  size of the cube in Megaparsec
*             Icube: size and shape of starting cube (or whatever):
*                    (*,1)eq.(0,0,0)
*                    (*,2)eq.(1,0,0)
*                    (*,3)eq.(0,1,0)
*                    (*,4)eq.(0,0,1)
*             mGal:  mass of a galaxie (all set to one)
      Real Pot(5)
*             strength of potentials 1..5
      External DERIVS, BSSTEP, ODEINT, RZEXTR, MMID, RAN1
*             see Press et al.
      External SETICD, TIMEST, BVK, FRICT, ENBIL, VELDIS, PROPHS
*             sind beschrieben in Report 2
      External IDEENS, IDSTAR, RDIN, WROUT,ICIN
*            IDEENS: identify ensemble: loads Ystart for ODEINT
*            IDSTAR: ist Umkehrfunktion von IDEENS
*            RDIN:   liest Parameter fuer den Programmlauf ein
*            WROUT:  Ausgabe der Daten
*            ICIN:   Setzen von Anfangsbedingungen aus file ic.par
      COMMON /PATH/ KMAX,KOUNT,DXSAV,XP,YP
*             Protokollblock fuer Bulirsch-Stoer
*            NMAX,NVAR,MAXGAL
*             Felddimensionierungsargumente s.Konstantendeklarationen
      COMMON /POS/ Yens
*             Position des Ensembles im Phasenraum
      COMMON /FDIS/ ADDRS
      COMMON /RS/ GAL,NGAL,Pot
*             Reibungskonstanten und aktuelle Galaxie
      COMMON /GRAV/ ADD3RS
*             Selfgravitational forces
      COMMON /SOFT/ b2(5)
*             Softening parameters
      COMMON /MOM/ LinMom, AngMom
      COMMON /ESG/ EpotSG
      call RDIN(X1,X2,NX2,EPS,H1,HMIN,Tstart,SigmaG,DeltaG,
     *Lambda,mGal,Rcutof,Rcut2,IDUM,size,Icube,NGAL,icVal,Pot,b2,
     *canal)
           KMAX  = 0      !  kein Protokoll fuer Bulirsch-Stoer
           DXSAV = 0.0
           Delta = X2-X1  !  Schrittintervall
      call SETICD(Tstart,Yens,IDUM,size,Icube,mGal,NGAL)
      if (icVal.GT.0) call ICIN(icVal,NGAL)
      open(UNIT=1,ERR=13,IOSTAT=ios,File='ens.dat',STATUS='UNKNOWN')
      If (ios.GT.0) Pause 'Error opening <ens.dat>'
      open(UNIT=2,ERR=13,IOSTAT=ios,File='ps.dat',STATUS='UNKNOWN')
      If (ios.GT.0) Pause 'Error opening <ps.dat>'
```

```
      open(UNIT=3,ERR=13,IOSTAT=ios,File='vdis.dat',STATUS='UNKNOWN')
      If (ios.GT.0) Pause 'Error opening <vdis.dat>'
      open(UNIT=4,ERR=13,IOSTAT=ios,File='enj.dat',STATUS='UNKNOWN')
      If (ios.GT.0) Pause 'Error opening <enj.dat>'
      open(UNIT=5,ERR=13,IOSTAT=ios,File='dump.dat',STATUS='UNKNOWN')
      If (ios.GT.0) Pause 'Error opening <dump.dat>'
*       Fehlerabfang:
      GOTO 23
13      Pause 'Error while opening outputfile'
      GOTO 23
19      Pause 'Error while closing outputfile'
23    Continue
*                       Start der Hauptschleife (Main Loop)
*           WARNUNG: Debug Anweisungen duerfen PAUSE jetzt nicht
*                    mehr verwenden, da Files offen sind !
      Tdis=0
      Do 100 I=1,NX2
*                      aeussere Hauptschleife (Outer Main Loop):
D     Print *, 'sweep: ',I
*       this PRINT shows the sweep No.on which ls is running actually
      call BVK(size,Yens,NGAL)
      SGs2= DeltaG*DeltaG
      call SELFGR(mGal,Rcut2,size,SGs2)
*                                  SGs2 softenes selfgravitation
      call FRICT(SigmaG,DeltaG,mGal,Lambda,Rcutof,size)
      Edis=0
      Do 60 GAL = 1,NGAL
*                       innere Hauptschleife (Inner Main Loop):
*                       NGAL Schritte entsprechen einem "sweep"
*                       durch den Phasenraum
      Call IDEENS(Ystart,GAL)
      Call STORE(Ystart,Yold)
      Call Odeint(Ystart,NVAR,X1,X2,EPS,H1,HMIN,NNOK,NNBAD,DERIVS,
     *BSSTEP)
      Call WFRICT(Edis,Tdis,Ystart,Yold)
      Call IDSTAR(Ystart,GAL)
      NOK(GAL)=NNOK
      NBAD(GAL)=NNBAD
*                      recall that Ystart(2) contains the derivative
*                      and Ystart(1) the value at X2
60    Continue
*                      Ende der inneren Hauptschleife
      call ENBIL(MEpot,MEkin,mGal)
      call VELDIS(VDIS,Temp,mGal,canal)
      call PROPHS(PS2D,NGAL)
      call WROUT(Yens,PS2D,VDIS,canal,
     *     MEpot,MEkin,Edis,Tdis,NOK,NBAD,Temp,I,NX2)
      call TIMEST(Delta,X1,X2)
100   Continue
*                     aeussere Haupschleife beended
      close(UNIT=1,ERR=19,STATUS='UNKNOWN')
      close(UNIT=2,ERR=19,STATUS='UNKNOWN')
      close(UNIT=3,ERR=19,STATUS='UNKNOWN')
      close(UNIT=4,ERR=19,STATUS='UNKNOWN')
      close(UNIT=5,ERR=19,STATUS='UNKNOWN')
      END
*                      fin

      SUBROUTINE DERIVS(X,Y,DYDX)

*     - Applied each time step
*     - Wertet die recht Seite der ODEqs. aus; entspricht also der
*     Ableitung von Y and der Stelle X
*     - Note that Y(1)=x, Y(5)=y, Y(9)=z, DY(i)DX= Y(i+1)

      Implicit logical(A-Z)
      Integer NMAX,NVAR,MAXGAL,NGAL,GAL
      Parameter(NVAR=12,NMAX=12,MAXGAL=1000)
      Real DYDX(NMAX),Y(NMAX),X,ADDRS(MAXGAL),ADD3RS(3,MAXGAL)
      Real b2(5),Pot(5),G, FpotX,FpotY,FpotZ,NN4,pi
      Parameter(G=1.,pi=3.14159265)
```



```
      COMMON /FDIS/ ADDRS
      COMMON /RS/ GAL,NGAL,Pot
      COMMON /GRAV/ ADD3RS
      COMMON /SOFT/ b2(5)
      If (ADDRS(GAL).LT.0.) Then
       Print*, 'Friction accelerates (negative)!'
       call MYSTOP
      Endif
      NN4= SQRT(Y(1)*Y(1)+Y(5)*Y(5)+Y(9)*Y(9)+b2(4))

      FpotX= -Pot(1)*Y(1)-
     *G*Pot(2)*Y(1)/SQRT(Y(1)*Y(1)+b2(2))-
     *G/pi*Pot(3)*Y(1)/(Y(1)*Y(1)+Y(5)*Y(5)+b2(3))-
     *Y(1)*G/4/pi*Pot(4)/NN4/NN4/NN4

      FpotY= -Pot(1)*Y(5)-
     *G/pi*Pot(3)*Y(5)/(Y(1)*Y(1)+Y(5)*Y(5)+b2(3))-
     *Y(5)*G/4/pi*Pot(4)/NN4/NN4/NN4

      FpotZ= -Pot(1)*Y(9)-
     *Y(9)*G/4/pi*Pot(4)/NN4/NN4/NN4

*      x-Koordinate
      DYDX(1) =     Y(2)
      DYDX(2) =     FpotX-ADDRS(GAL)*Y(2) +ADD3RS(1,GAL)
*      y-Koordinate
      DYDX(5) =     Y(6)
      DYDX(6) =     FpotY-ADDRS(GAL)*Y(6) +ADD3RS(2,GAL)
*      z-Koordinate
      DYDX(9) =     Y(10)
      DYDX(10) =    FpotZ-ADDRS(GAL)*Y(10)+ADD3RS(3,GAL)
*      Diese werden nicht gebraucht:
      DYDX(3) =     0.
      DYDX(4) =     0.
      DYDX(7) =     0.
      DYDX(8) =     0.
      DYDX(11) =    0.
      DYDX(12) =    0.
      END

      SUBROUTINE MYSTOP
      close(UNIT=1,ERR=19,STATUS='UNKNOWN')
      close(UNIT=2,ERR=19,STATUS='UNKNOWN')
      close(UNIT=3,ERR=19,STATUS='UNKNOWN')
      close(UNIT=4,ERR=19,STATUS='UNKNOWN')
      close(UNIT=5,ERR=19,STATUS='UNKNOWN')
      Stop
19    Pause 'Das sollte wirklich nicht passieren !'
      END

      SUBROUTINE STORE(Y,Yold)
      implicit logical(A-Z)
      Integer NMAX,NVAR,MAXGAL,i
      Parameter(NVAR=12,NMAX=12,MAXGAL=1000)
      Real Y(NVAR), Yold(NVAR)
      Do 50 i=1,NVAR
            Yold(i)=Y(i)
50    Continue
      END

      SUBROUTINE WFRICT(Edis,Tdis,Y,Yold)
      implicit logical(A-Z)
      Integer NMAX,NVAR,MAXGAL,GAL,NGAL
      Parameter(NVAR=12,NMAX=12,MAXGAL=1000)
      Real Y(NVAR),Yold(NVAR),Pot(5), DeltaY, Edis, Tdis
      Real ADDRS(MAXGAL)
      COMMON /RS/ GAL,NGAL,Pot
      COMMON /FDIS/ ADDRS
      DeltaY=SQRT(
     * (Y(1)-Yold(1))*(Y(1)-Yold(1))+
     * (Y(5)-Yold(5))*(Y(5)-Yold(5))+
```

```
     *  (Y(9)-Yold(9))*(Y(9)-Yold(9)) )
        Edis=Edis+ DeltaY*ADDRS(GAL)
        Tdis=Tdis+ DeltaY*ADDRS(GAL)
        END

        SUBROUTINE IDEENS(Ystart,GAL)

*       - Applied each galaxy step
*       - identifiziert Ystart mit der GAL'ten Galaxie des Ensembles Yens

        implicit logical(A-Z)
        Integer NMAX,NVAR,MAXGAL,GAL, i
        Parameter(NVAR=12,NMAX=12,MAXGAL=1000)
        Real Yens(NVAR,MAXGAL), Ystart(NVAR)
        COMMON /POS/ Yens
        Do 50 i=1,NVAR
        Ystart(i)=Yens(i,GAL)
50      Continue
        END

        SUBROUTINE IDSTAR(Ystart,GAL)

*       - Applied each galaxy step
*       - identifiziert die GAL'ten Galaxie des Ensembles Yens mit Ystart

        implicit logical(A-Z)
        Integer NMAX,NVAR,MAXGAL,GAL, i
        Parameter(NVAR=12,NMAX=12,MAXGAL=1000)
        Real Yens(NVAR,MAXGAL), Ystart(NVAR)
        COMMON /POS/ Yens
        Do 50 i=1,NVAR
        Yens(i,GAL)=Ystart(i)
50      Continue
        END

        SUBROUTINE SETICD(Temp,Yens,IDUM,size,Icube,mGal,NGAL)

*        - Applied initially
*        - Setzt die Anfangsbedingungen entsprechend einer
*        kinetischen Temperatur der Galaxien.

        implicit logical(A-Z)
        Integer NMAX,NVAR,MAXGAL,IDUM,NGAL
        Parameter(NVAR=12,NMAX=12,MAXGAL=1000)
        Real Yens(NVAR,MAXGAL),Temp,mGal,size,Icube(3,4)
        Real RAN1
        External RAN1
        Integer I,J
        Real k,pi,Znor(7),scal,mSol
        Parameter(k=1.38066e-9,pi=3.1415926,mSol=1.)
        scal=SQRT(ABS(k*Temp*mSol/mGal))
        Do 30 J=1,NGAL
*        - Erzeuge 4 Gaussverteilte Zufallszahlen
*        und 3 Normalverteilte Zufallszahlen
        Do 20 I=1,7
         Znor(I)=RAN1(IDUM)
20      Continue
*        - Orte Normalverteilt in Icube und
*        Geschwindigkeitskomponenten Gaussverteilt (Box-Mueller)
        Yens(1,J) =Znor(1)*(Icube(1,2)-Icube(1,1))+Icube(1,1)
        Yens(2,J) =SQRT(-2.*ALOG(Znor(4)))*COS(2.*pi*Znor(5))*scal
        Yens(5,J) =Znor(2)*(Icube(2,3)-Icube(2,1))+Icube(2,1)
        Yens(6,J) =SQRT(-2.*ALOG(Znor(4)))*SIN(2.*pi*Znor(5))*scal
        Yens(9,J) =Znor(3)*(Icube(3,4)-Icube(3,1))+Icube(3,1)
        Yens(10,J)=SQRT(-2.*ALOG(Znor(6)))*COS(2.*pi*Znor(6))*scal
D       Print*, 'Initial values for galaxy ',J,'   are: '
D       Print*, '  x:',Yens(1,J),'  y: ',Yens(5,J),'  z: ',Yens(9,J)
D       Print*, ' vx:',Yens(2,J),' vy: ',Yens(6,J),' vz: ',Yens(10,J)
30      Continue
        END
```



```
        SUBROUTINE TIMEST(Delta,X1,X2)

*        - Applied each time sweep
*        - fuehrt einen Schritt in der unabhaengigen
*        Variablen x (der Zeit) aus
        implicit logical(A-Z)
        Real X1,X2,Delta
        X1=X2
        X2=X2+Delta
        END

        SUBROUTINE ICIN(icVal,NGAL)

*        - Applied on condition icVal.GE.0 initially
*        - reads from file <ic.par> the initial locations and
*        velocities of icVal galaxies
*        in format x,y,z,vx,vy,vz
        implicit logical(A-Z)
        Integer NMAX,NVAR,MAXGAL,NGAL,I,ios,icVal
        Parameter(NVAR=12,NMAX=12,MAXGAL=1000)
        Real Yens(NVAR,MAXGAL)
        COMMON /POS/ Yens
        open(UNIT=1,ERR=13,IOSTAT=ios,File='ic.par',STATUS='OLD')
*         Fehlerabfang:
        If (ios.GT.0) GOTO 13
        GOTO 23
13        Print*, 'Error while opening file ic.par'
          call MYSTOP
        GOTO 23
17        Print*, 'Bad parameterfile ic.par'
          call MYSTOP
        GOTO 23
19        Print*, 'Error while closing file ic.par'
          call MYSTOP
23      Continue
        Do 50 I=1,icVal
        READ(UNIT=1,'(6(G13.3))',ERR=17,END=17) Yens(1,I),
     *Yens(5,I),Yens(9,I),Yens(2,I),Yens(6,I),Yens(10,I)
50      Continue
        close(UNIT=1,ERR=19,STATUS='OLD')
        END

        SUBROUTINE BVK(size,Yens,NGAL)

*        - Applied each sweep
*        - Born von Karman Randbedingungen: Die Galaxien werden nach
*        jeweils einem sweep wieder in ihre 1.Brillouinzone gesetzt.
*        (von -size/2 bis +size/2)
*        Die Geschwindigkeit wird dabei beibehalten.
*        Anmerkung: zur Berechnung der Reibung muessen die periodischen
*        Bilder der Galaxien in den Nachbarzellen beruecksichtigt werden.

        implicit logical(A-Z)
        Integer NMAX,NVAR,MAXGAL,NGAL,I,J
        Real size, LBOUND,UBOUND
        Parameter(NVAR=12,NMAX=12,MAXGAL=1000)
        Real Yens(NVAR,MAXGAL)
        LBOUND = -size/2
        UBOUND =  size/2
        Do 60 J=1,NGAL
        Do 50 I=1,9,4
        If (Yens(I,J).LT.LBOUND) Yens(I,J)=Yens(I,J)+size
        If (Yens(I,J).GE.UBOUND) Yens(I,J)=Yens(I,J)-size
50      Continue
60      Continue
        END

        SUBROUTINE FRICT(SigmaG,DeltaG,mGal,Lambda,Rcutof,size)

*        - Applied each sweep
*        - Berechnet den Reibungsterm ADDRS in der rechten Seite der ODEqs
```

```
*       Dieser stellt bereits die Kraft dar, die die GAL'te Galaxie
*       im CM-frame zur Ruhe bringen moechte. Dies entspricht
*       daher detailliertem Gleichgewicht der Reibungskraefte.
*       Ohne detailliertes GG duerfte der Beitrag nicht proportional
*       (und damit parallel) der Geschwindigkeit addiert werden !
*       (ADDRS: append on right side)
*      - Vgl. Bemerkung in BVK
*      - Der Zugriff auf ADDRS erfolgt
*      ueber einen COMMON-Block, da ADDRS von ueber diesen Block an
*      DERIVS (vgl. Press et al.) weitergegeben wird.

      Implicit logical(A-Z)
      Integer NMAX,NVAR,MAXGAL,NGAL,GAL,I,J,K
      Parameter(NVAR=12,NMAX=12,MAXGAL=1000)
      Real Yens(NVAR,MAXGAL)
      Real SigmaG,DeltaG,Lambda,mGal,size,ADDRS(MAXGAL)
      Real Rcutof,mSol
      Real D2(NMAX),DD,pi,G,scal,term,term1,term2,h5tD,h5tS,h1tD,h1tS
      Parameter(pi=3.1415926,G=1.,mSol=1.)
      Real R,V,Rsq,Vsq,Pot(5)
      COMMON /POS/ Yens
      COMMON /FDIS/ ADDRS
      COMMON /RS/ GAL,NGAL,Pot
*         GAL wird hier nicht benoetigt (applied each sweep)
      Intrinsic AMIN1
*      Zunaechst einige Rechengroessen:
      scal=16./3.*pi*pi*ALOG(Lambda)*mGal*mGal
      h5tD= SQRT(2.)*DeltaG
      h1tD= 2.*DeltaG*DeltaG
      h5tS= SQRT(2.)*SigmaG
      h1tS= 2.*SigmaG*SigmaG
*      Initialisiere ADDRS:
      DO 50 I=1,NGAL
      ADDRS(I)=0
50    Continue
*      Berechne nun ADDRS fuer Paare von Galaxien:
       If (NGAL.LE.1) GOTO 90
      DO 80 I=1,NGAL-1
      DO 70 J=I+1,NGAL
      DO 60 K=1,9,4
*      Abstandsquadrat in einer Koordinate mit Bildern:
      D2(K)  =ABS(Yens(K,I)-Yens(K,J))
      DD     =ABS(D2(K)-size)
      D2(K)  =AMIN1(D2(K),DD)
      D2(K)  =D2(K)*D2(K)
*      Geschwindigkeitsdifferenzquadrat in einer Koordinate:
      D2(K+1)=ABS(Yens(K+1,I)-Yens(K+1,J))
      D2(K+1)=D2(K+1)*D2(K+1)
60    Continue
*      Abstand:
      R=SQRT(D2(1)+D2(5)+D2(9))
      Rsq=R*R
*      Geschwindigkeit
      V=SQRT(D2(2)+D2(6)+D2(10))
      Vsq=V*V
*      Falls der Abstand echt kleiner einem Cutoffabstand ist:
      If (R.LT.Rcutof) Then
        term1= 1/h1tD/h5tD * 1/h1tS/h5tS
        term2= EXP(-Rsq/h1tD - Vsq/h1tS)
        term = scal*term1*term2
        ADDRS(I)=ADDRS(I)+term
        ADDRS(J)=ADDRS(J)+term
      Endif
70    Continue
80    Continue
90    Continue
      END

      SUBROUTINE SELFGR(mGal,Rcut2,size,b2)

*      - Applied each sweep
```



```
*      - Berechnet den Term ADD3RS in der rechten Seite der ODEqs
*        Dieser stellt die Kraft dar, die die GAL'te Galaxie
*        von allen anderen Galaxien erfaehrt.
*      - Vgl. Bemerkung in BVK
*      - Der Zugriff auf ADD3RS erfolgt
*      ueber einen COMMON-Block, da ADD3RS von ueber diesen Block an
*      DERIVS (vgl. Press et al.) weitergegeben wird.
*      - evaluates EpotSG

      Implicit logical(A-Z)
      Integer NMAX,NVAR,MAXGAL,NGAL,GAL,I,J,K,L
      Parameter(NVAR=12,NMAX=12,MAXGAL=1000)
      Real Yens(NVAR,MAXGAL), EpotSG, LinMom, AngMom
      Real Lin(3),Ang(3)
      Real mGal,mSol,size,ADD3RS(3,MAXGAL)
     *,Rcut2
      Real D2(NMAX),VRZ(NMAX),DD,G,scal,term1,term2,term3
      Parameter(G=1.,mSol=1.)
      Real R,sR,sRsq,b2,Pot(5)
      Real x,y,z,vx,vy,vz
      COMMON /POS/ Yens
      COMMON /GRAV/ ADD3RS
      COMMON /RS/ GAL,NGAL,Pot
*         GAL wird hier nicht benoetigt (applied each sweep)
      COMMON /ESG/ EpotSG
      COMMON /MOM/ LinMom, AngMom
      Intrinsic AMIN1
*      Zunaechst einige Rechengroessen und Initialisierungen.:
      scal=G*mGal*mGal*mSol*mSol
      AngMom=0.
      LinMom=0.
      EpotSG=0.
*      Initialisiere ADD3RS:
      DO 52 L=1,3
       Lin(L)=0.
       Ang(L)=0.
      DO 50 I=1,NGAL
       ADD3RS(L,I)=0.
50    Continue
52    Continue
*      Berechne nun ADD3RS fuer Paare von Galaxien:
       If (NGAL.LE.1) GOTO 80
      DO 80 I=1,NGAL-1
      DO 70 J=I+1,NGAL
      DO 60 K=1,9,4
*      Abstandsquadrat in einer Koordinate mit Bildern:
      D2(K)  =ABS(Yens(K,I)-Yens(K,J))
      DD     =ABS(D2(K)-size)
      D2(K)  =AMIN1(D2(K),DD)
      D2(K)  =D2(K)*D2(K)
*      Vorzeichen der Anziehungskraft wechselt fuer Bilder:
      VRZ(K)  =1.
      IF (DD.LT.D2(K)) VRZ(K)= -1.
60    Continue
*      distance:
      R=SQRT(D2(1)+D2(5)+D2(9))
*      softened distance
      sR=SQRT(D2(1)+D2(5)+D2(9)+b2)
      sRsq=sR*sR
*      Falls der Abstand echt kleiner einem Cutoffabstand ist:
      If (R.LT.Rcut2) Then
        term1=scal*(Yens(1,I)-Yens(1,J))/sR/sRsq
        term2=scal*(Yens(5,I)-Yens(5,J))/sR/sRsq
        term3=scal*(Yens(9,I)-Yens(9,J))/sR/sRsq
        ADD3RS(1,I)=ADD3RS(1,I)-VRZ(1)*term1
        ADD3RS(1,J)=ADD3RS(1,J)+VRZ(1)*term1
        ADD3RS(2,I)=ADD3RS(2,I)-VRZ(5)*term2
        ADD3RS(2,J)=ADD3RS(2,J)+VRZ(5)*term2
        ADD3RS(3,I)=ADD3RS(3,I)-VRZ(9)*term3
        ADD3RS(3,J)=ADD3RS(3,J)+VRZ(9)*term3
        EpotSG=EpotSG-1/sR
```

```
      Endif
70    Continue
80    Continue
      Do 120 i=1,NGAL
      Lin(1)=Lin(1)+mGal*Yens(2,i)
      Lin(2)=Lin(2)+mGal*Yens(6,i)
      Lin(3)=Lin(3)+mGal*Yens(10,i)
      x=Yens(1,i)
      y=Yens(5,i)
      z=Yens(9,i)
      vx=Yens(2,i)
      vy=Yens(6,i)
      vz=Yens(10,i)
      Ang(1)=Ang(1)+mGal*(y*vz-z*vy)
      Ang(2)=Ang(2)+mGal*(z*vx-x*vz)
      Ang(3)=Ang(3)+mGal*(x*vy-y*vx)
120   Continue
      LinMom=SQRT(Lin(1)*Lin(1)+Lin(2)*Lin(2)+Lin(3)*Lin(3))
      AngMom=SQRT(Ang(1)*Ang(1)+Ang(2)*Ang(2)+Ang(3)*Ang(3))
      END

      SUBROUTINE ENBIL(MEpot,MEkin,mGal)

*      - Applied each sweep
*      - Berechnet den Mittelwert der kinetischen und potentiellen
*      Energie des Ensembles von Galaxien.
*      - Vorlaufig stehen die Formeln fuer die potentielle Energie
*      noch explizit in dieser Routine
*      - Die Energien fuer die einzelnen Galaxien werden ausgerechnet,
*      aber nicht zurueckgegeben (Zwischenrechnung)

      Implicit logical(A-Z)
      Integer NMAX,NVAR,MAXGAL,NGAL,GAL,I
      Parameter(NVAR=12,NMAX=12,MAXGAL=1000)
      Real Yens(NVAR,MAXGAL),mGal,mSol,G,Pot(5),b2(5),pi
      Parameter(mSol=1.,G=1.,pi=3.1415926)
      COMMON /POS/ Yens
      COMMON /RS/ GAL,NGAL,Pot
      COMMON /SOFT/ b2
      Real Epot(MAXGAL),Ekin(MAXGAL),MEpot,MEkin
*      kinetische und potentielle Energie fuer jede Galaxie einzeln:
      Do 50 I=1,NGAL
      Ekin(I) = 0.5*mGal*mSol*(Yens(2,I)*Yens(2,I)+
     *Yens(6,I)*Yens(6,I)+Yens(10,I)*Yens(10,I))
      Epot(I) = G*Pot(2)/2. *SQRT(Yens(1,I)*Yens(1,I)+b2(2))+
     *G/2/pi*Pot(3)*ALOG(Yens(1,I)*Yens(1,I)+Yens(5,I)*Yens(5,I)+
     *  Yens(9,I)*Yens(9,I)+b2(3))-
     *G/4/pi*Pot(4)/SQRT(Yens(1,I)*Yens(1,I)+Yens(5,I)*Yens(5,I)+
     *  Yens(9,I)*Yens(9,I)+b2(4))
50    Continue
      MEpot=0
      MEkin=0
*      Schaetzung des Mittelwerts fuer das Ensemble von Galaxien:
      Do 80 I=1,NGAL
      MEpot=MEpot+Epot(I)
      MEkin=MEkin+Ekin(I)
80    Continue
      MEkin=MEkin/ NGAL
      MEpot=MEpot/ NGAL
      END

      SUBROUTINE VELDIS(VDIS,Temp,mGal,canal)

*      - Applied each sweep
*      - Berechnet die Geschwindigkeitsverteilung des
*      Ensembles von Galaxien. Ermittelt ferner
*      aus dieser Verteilung eine kinetische Temperatur.

      implicit logical(A-Z)
      Integer NMAX,NVAR,MAXGAL,NGAL,GAL,I,J
      Integer canal
```



```
      Parameter(NVAR=12,NMAX=12,MAXGAL=1000)
      Real Yens(NVAR,MAXGAL),mSol,mGal,Temp
      Real VDIS(2,20),VA(MAXGAL),MaV,Pot(5)
      Real pi,k
      Parameter(k=1.38066e-9,pi=3.1415926,mSol=1.)
      COMMON /POS/ Yens
      COMMON /RS/ GAL,NGAL,Pot
      External SORT
*      Berechne den Geschwindigkeitsbetrag (VA) fuer alle Galaxien
      DO 50 I=1,NGAL
       VA(I)= SQRT(Yens(2,I)*Yens(2,I)+Yens(6,I)*Yens(6,I)
     * -Yens(10,I)*Yens(10,I))
50    Continue
*      Berechne die mittlere absolute Geschwindigkeit:
      MaV=0
      Do 80 I=1,NGAL
       MaV=MaV+VA(I)
80    Continue
      MaV=MaV/NGAL
*      Erzeuge die Abszisse von VDIS (absol.Geschwindigkeit)
*      und initialisiere die Ordinate (die Haeufigkeit)
      Do 120 I=1,canal
       VDIS(1,I)=I*MaV*2./real(canal)
       VDIS(2,I)=0.
120   Continue
*      Sortiere die Geschwindigkeiten aufsteigend
      If (NGAL.GT.1) call SORT(NGAL,VA)
*     Nun eine Mehrkanalgeschwindigkeitsspektroskopie:
*                                        Starte am Anfang der Abszisse:
      J=1
      Do 150 I=1,NGAL
*          Ist die Geschwindigkeit kleiner der Abszisse, inkrementiere:
        If (VA(I).LE.VDIS(1,J)) Then
           VDIS(2,J)=VDIS(2,J)+1.
*          Ansonsten inkrementiere die Abszisse, solange bis die Geschwindigkeit
*          der Galaxie kleiner als der Wert der Abszisse geworden ist oder
*          bis das Ende der Abszisse erreicht worden ist.
        Else
135       Continue
          WENDE=.FALSE.
          If (J.GT.canal) Then
           Write(5,*) 'Error in multi channel analysis !'
           call MYSTOP
          ENDIF
          If (J.LT.canal) Then
            J=J+1
            If (VA(I).GT.VDIS(1,J)) WENDE=.TRUE.
          ENDIF
          If (WENDE) GOTO 135
          If (VA(I).LE.VDIS(1,J)) VDIS(2,J)=VDIS(2,J)+1
        Endif
150   Continue
*       Berechne die Temperatur aus der mittleren absoluten Geschwindigkeit
*       unter Annahme einer Maxwellverteilung fuer das Ensemble.
      Temp=pi/8*mGal*mSol*MAV*MAV
      END

      SUBROUTINE PROPHS(PS2D,NGAL)

*      - Applied each sweep
*      - berechnet Orte und Geschwindigkeiten in der x-Koordinate
*      aller Galaxien des Ensembles. Dient zur Darstellung im Phasenraum.

      implicit logical(A-Z)
      Integer NMAX,NVAR,MAXGAL,NGAL,I
      Real Yens, PS2D
      Parameter(NVAR=12,NMAX=12,MAXGAL=1000)
      DIMENSION Yens(NVAR,MAXGAL), PS2D(4,MAXGAL)
      COMMON /POS/ Yens
*      Berechne den Ort                    in x,y fuer alle Galaxien
*      Berechne das Geschwindigkeitquadrat  in x,y fuer alle Galaxien
```

```
      DO 50 I=1,NGAL
*        Definiere den Schnitt im Phasenraum:
       PS2D(1,I)=Yens(1,I)
       PS2D(2,I)=Yens(2,I)*ABS(Yens(2,I))
       PS2D(3,I)=Yens(5,I)
       PS2D(4,I)=Yens(6,I)*ABS(Yens(6,I))
50    Continue
      END

      SUBROUTINE WROUT(Yens,PS2D,VDIS,canal,MEpot,MEkin,
     *Edis,Tdis,NOK,NBAD,Temp,sNr,NX2)

*      - Applied each sweep
*      - Schreibt die Daten in ASCII files und erzeugt eine grafische
*      Ausgabe fuer PS2D, VDIS und die Energie des Ensembles.
*      - Protokolliert die Effizienz des ODE Algorithmus
*      - Temp ist ueber VDIS definiert und ihre Zeitreihe
*      enthaelt daher die numerischen Momenterzeugungseffekte.

      implicit logical(A-Z)
      Integer NMAX,NVAR,MAXGAL,NGAL,GAL,NX2
      Parameter(NVAR=12,NMAX=12,MAXGAL=1000)
      Real Yens(NVAR,MAXGAL),PS2D(4,MAXGAL),VDIS(2,20),MEpot,MEkin
      Real ADDRS(MAXGAL),ADD3RS(3,MAXGAL),Temp, Pot(5), EpotSG
      Real LinMom, AngMom, Edis, Tdis
      Integer NOK(MAXGAL),NBAD(MAXGAL),I,sNr,canal
*                                       sNr denotes the sweep No.
      COMMON /FDIS/ ADDRS
      COMMON /RS/ GAL,NGAL,Pot
      COMMON /GRAV/ ADD3RS
*        GAL wird hier nicht benoetigt (applied each sweep)
      COMMON /ESG/ EpotSG
      COMMON /MOM/ LinMom, AngMom
*      Fehlerabfang:
      GOTO 27
21    Pause 'Error in writing data on Unit 1'
      GOTO 27
22    Pause 'Error in writing data on Unit 2'
      GOTO 27
23    Pause 'Error in writing data on Unit 3'
      GOTO 27
24    Pause 'Error in writing data on Unit 4'
      GOTO 27
25    Pause 'Error in writing data on Unit 5'
      GOTO 27
27    Continue
      IF (sNr.EQ.NX2) THEN
      Do 50 I=1,NGAL
      WRITE(1,'(3(G13.3),I8.1)',ERR=21) Yens(1,I),Yens(5,I),Yens(9,I),
     *sNr
      WRITE(2,'(4(G13.3))',ERR=22) PS2D(1,I),
     *PS2D(2,I),PS2D(3,I),PS2D(4,I)
      WRITE(5,'(2(I8.1),1(G13.3))',ERR=25) NOK(I),NBAD(I),ADDRS(I)
50    Continue
      ENDIF
      Do 80 I=1,canal
      WRITE(3,'((G13.3),2(I8.1))',ERR=23) VDIS(1,I),NINT(VDIS(2,I))
     * , sNr
80    Continue
      WRITE(4,'(8(G13.3))',ERR=24) MEkin, MEpot, EpotSG, Edis,
     * MEkin+MEpot+EpotSG+Tdis, Temp, LinMom, AngMom
      END

      SUBROUTINE RDIN(X1,X2,NX2,EPS,H1,HMIN,Tstart,SigmaG,DeltaG,
     *Lambda,mGal,Rcutof,Rcut2,IDUM,size,Icube,NGAL,icVal,Pot,b2,
     *canal)

*      - Applied initially
*      - liest ein Parameterfile ein
*      mit Schrittintervall (X1,X2)
*      Anzahl Zeitschritte NX2
```



```
*      Fehlerkontrollparametern EPS,H1,HMIN
*      Starttemperatur und Galaxieparametern fuer die Reibung

      implicit logical(A-Z)
      Real X1,X2,EPS,H1,HMIN,Tstart,SigmaG,DeltaG,Lambda,mGal,
     *Rcutof,Rcut2
      Integer IDUM,NX2,NGAL,icVal
      Real size,Icube(3,4),Pot(5)
      integer ios
      real b2(5)
      Integer canal
      CHARACTER *12 iFile,dummy
      CHARACTER *40 comm40
*      comm40 allows to make a comment of 40 Bytes on the top
*      of the parameterfile
      iFile = 'set.par'
D      print*, 'Read data from ',iFile
      open(UNIT=1,ERR=13,IOSTAT=ios,File=iFile,STATUS='OLD')
*        Fehlerabfang:
      If (ios.GT.0) GOTO 13
      GOTO 23
13      Print*, 'Error while opening parameterfile'
        call MYSTOP
      GOTO 23
17      Print*, 'Bad parameterfile'
        call MYSTOP
      GOTO 23
19      Print*, 'Error while closing file'
        call MYSTOP
23    Continue
      READ(UNIT=1,*,ERR=17,END=17) comm40,dummy,X1,dummy,X2,
     *dummy,NX2,dummy,EPS,dummy,H1,dummy,HMIN,dummy,Tstart,
     *dummy,SigmaG,dummy,DeltaG,dummy,Lambda,dummy,mGal,dummy,Rcutof,
     *dummy,Rcut2,dummy,IDUM,dummy,size,dummy,Icube,
     *dummy,NGAL,dummy,icVal,dummy,Pot(1),dummy,Pot(2),dummy,
     *Pot(3),dummy,Pot(4),dummy,Pot(5),dummy,b2(1),dummy,b2(2),
     *dummy,b2(3),dummy,b2(4),dummy,b2(5),dummy,canal
      close(UNIT=1,ERR=19,STATUS='OLD')
D      PRINT*, 'Comment of ',ifile,': ',comm40
      END

      SUBROUTINE ODEINT(YSTART,NVAR,X1,X2,EPS,H1,HMIN,NOK,NBAD,DERIVS,RK
     *QC)
      PARAMETER (MAXSTP=10000,NMAX=12,TWO=2.0,ZERO=0.0,TINY=1.E-30)
      COMMON /PATH/ KMAX,KOUNT,DXSAV,XP(200),YP(10,200)
      DIMENSION YSTART(NVAR),YSCAL(NMAX),DYDX(NMAX)
      DIMENSION Y(NMAX)
      X=X1
      H=SIGN(H1,X2-X1)
      NOK=0
      NBAD=0
      KOUNT=0
      DO 11 I=1,NVAR
        Y(I)=YSTART(I)
11    CONTINUE
      XSAV=X-DXSAV*TWO
      DO 16 NSTP=1,MAXSTP
        CALL DERIVS(X,Y,DYDX)
        DO 12 I=1,NVAR
          YSCAL(I)=ABS(Y(I))+ABS(H*DYDX(I))+TINY
12      CONTINUE
        IF(KMAX.GT.0)THEN
          IF(ABS(X-XSAV).GT.ABS(DXSAV)) THEN
            IF(KOUNT.LT.KMAX-1)THEN
              KOUNT=KOUNT+1
              XP(KOUNT)=X
              DO 13 I=1,NVAR
                YP(I,KOUNT)=Y(I)
13            CONTINUE
              XSAV=X
            ENDIF
```

```
          ENDIF
        ENDIF
        IF((X+H-X2)*(X+H-X1).GT.ZERO) H=X2-X
        CALL RKQC(Y,DYDX,NVAR,X,H,EPS,YSCAL,HDID,HNEXT,DERIVS)
        IF(HDID.EQ.H)THEN
          NOK=NOK+1
        ELSE
          NBAD=NBAD+1
        ENDIF
        IF((X-X2)*(X2-X1).GE.ZERO)THEN
          DO 14 I=1,NVAR
            YSTART(I)=Y(I)
14        CONTINUE
          IF(KMAX.NE.0)THEN
            KOUNT=KOUNT+1
            XP(KOUNT)=X
            DO 15 I=1,NVAR
              YP(I,KOUNT)=Y(I)
15          CONTINUE
          ENDIF
          RETURN
        ENDIF
        IF(ABS(HNEXT).LT.HMIN) then
             Write(5,*) 'Stepsize smaller than minimum.'
             call MYSTOP
        endif
        H=HNEXT
16    CONTINUE
      Write(5,*) 'Too many steps.'
      call MYSTOP
      RETURN
      END

      SUBROUTINE BSSTEP(Y,DYDX,NV,X,HTRY,EPS,YSCAL,HDID,HNEXT,DERIVS)
      PARAMETER (NMAX=12,IMAX=11,NUSE=7,ONE=1.E0,SHRINK=.95E0,GROW=1.2E0
     *)
      DIMENSION Y(NV),DYDX(NV),YSCAL(NV),YERR(NMAX),
     *    YSAV(NMAX),DYSAV(NMAX),YSEQ(NMAX),NSEQ(IMAX)
      DATA NSEQ /2,4,6,8,12,16,24,32,48,64,96/
      H=HTRY
      XSAV=X
      DO 11 I=1,NV
        YSAV(I)=Y(I)
        DYSAV(I)=DYDX(I)
11    CONTINUE
1     DO 10 I=1,IMAX
        CALL MMID(YSAV,DYSAV,NV,XSAV,H,NSEQ(I),YSEQ,DERIVS)
        XEST=(H/NSEQ(I))**2
        CALL RZEXTR(I,XEST,YSEQ,Y,YERR,NV,NUSE)
        ERRMAX=0.
        DO 12 J=1,NV
          ERRMAX=MAX(ERRMAX,ABS(YERR(J)/YSCAL(J)))
12      CONTINUE
        ERRMAX=ERRMAX/EPS
        IF(ERRMAX.LT.ONE) THEN
          X=X+H
          HDID=H
          IF(I.EQ.NUSE)THEN
            HNEXT=H*SHRINK
          ELSE IF(I.EQ.NUSE-1)THEN
            HNEXT=H*GROW
          ELSE
            HNEXT=(H*NSEQ(NUSE-1))/NSEQ(I)
          ENDIF
          RETURN
        ENDIF
10    CONTINUE
      H=0.25*H/2**((IMAX-NUSE)/2)
      IF(X+H.EQ.X) then
       Write(5,*) 'Step size underflow.'
       call MYSTOP
```



```
      endif
      GOTO 1
      END

      SUBROUTINE RZEXTR(IEST,XEST,YEST,YZ,DY,NV,NUSE)
      PARAMETER (IMAX=11,NMAX=12,NCOL=7)
      DIMENSION X(IMAX),YEST(NV),YZ(NV),DY(NV),D(NMAX,NCOL),FX(NCOL)
      X(IEST)=XEST
      IF(IEST.EQ.1) THEN
        DO 11 J=1,NV
          YZ(J)=YEST(J)
          D(J,1)=YEST(J)
          DY(J)=YEST(J)
11      CONTINUE
      ELSE
        M1=MIN(IEST,NUSE)
        DO 12 K=1,M1-1
          FX(K+1)=X(IEST-K)/XEST
12      CONTINUE
        DO 14 J=1,NV
          YY=YEST(J)
          V=D(J,1)
          C=YY
          D(J,1)=YY
          DO 13 K=2,M1
            B1=FX(K)*V
            B=B1-C
            IF(B.NE.0.) THEN
              B=(C-V)/B
              DDY=C*B
              C=B1*B
            ELSE
              DDY=V
            ENDIF
            V=D(J,K)
            D(J,K)=DDY
            YY=YY+DDY
13        CONTINUE
          DY(J)=DDY
          YZ(J)=YY
14      CONTINUE
      ENDIF
      RETURN
      END

      SUBROUTINE MMID(Y,DYDX,NVAR,XS,HTOT,NSTEP,YOUT,DERIVS)
      PARAMETER (NMAX=12)
      DIMENSION Y(NVAR),DYDX(NVAR),YOUT(NVAR),YM(NMAX),YN(NMAX)
      H=HTOT/NSTEP
      DO 11 I=1,NVAR
        YM(I)=Y(I)
        YN(I)=Y(I)+H*DYDX(I)
11    CONTINUE
      X=XS+H
      CALL DERIVS(X,YN,YOUT)
      H2=2.*H
      DO 13 N=2,NSTEP
        DO 12 I=1,NVAR
          SWAP=YM(I)+H2*YOUT(I)
          YM(I)=YN(I)
          YN(I)=SWAP
12      CONTINUE
        X=X+H
        CALL DERIVS(X,YN,YOUT)
13    CONTINUE
      DO 14 I=1,NVAR
        YOUT(I)=0.5*(YM(I)+YN(I)+H*YOUT(I))
14    CONTINUE
      RETURN
      END
```

```
      SUBROUTINE SORT(N,RA)
      DIMENSION RA(N)
      L=N/2+1
      IR=N
 10   CONTINUE
        IF(L.GT.1)THEN
          L=L-1
          RRA=RA(L)
        ELSE
          RRA=RA(IR)
          RA(IR)=RA(1)
          IR=IR-1
          IF(IR.EQ.1)THEN
            RA(1)=RRA
            RETURN
          ENDIF
        ENDIF
        I=L
        J=L+L
 20     IF(J.LE.IR)THEN
          IF(J.LT.IR)THEN
            IF(RA(J).LT.RA(J+1))J=J+1
          ENDIF
          IF(RRA.LT.RA(J))THEN
            RA(I)=RA(J)
            I=J
            J=J+J
          ELSE
            J=IR+1
          ENDIF
        GO TO 20
        ENDIF
        RA(I)=RRA
      GO TO 10
      END

      FUNCTION RAN1(IDUM)
      DIMENSION R(97)
      PARAMETER (M1=259200,IA1=7141,IC1=54773,RM1=3.8580247E-6)
      PARAMETER (M2=134456,IA2=8121,IC2=28411,RM2=7.4373773E-6)
      PARAMETER (M3=243000,IA3=4561,IC3=51349)
      DATA IFF /0/
      IF (IDUM.LT.0.OR.IFF.EQ.0) THEN
        IFF=1
        IX1=MOD(IC1-IDUM,M1)
        IX1=MOD(IA1*IX1+IC1,M1)
        IX2=MOD(IX1,M2)
        IX1=MOD(IA1*IX1+IC1,M1)
        IX3=MOD(IX1,M3)
        DO 11 J=1,97
          IX1=MOD(IA1*IX1+IC1,M1)
          IX2=MOD(IA2*IX2+IC2,M2)
          R(J)=(FLOAT(IX1)+FLOAT(IX2)*RM2)*RM1
 11     CONTINUE
        IDUM=1
      ENDIF
      IX1=MOD(IA1*IX1+IC1,M1)
      IX2=MOD(IA2*IX2+IC2,M2)
      IX3=MOD(IA3*IX3+IC3,M3)
      J=1+(97*IX3)/M3
      IF(J.GT.97.OR.J.LT.1) then
       Write(5,*) 'RAN1 hat Schwierigkeiten'
       call MYSTOP
      endif
      RAN1=R(J)
      R(J)=(FLOAT(IX1)+FLOAT(IX2)*RM2)*RM1
      RETURN
      END
```

```
Standardparameterfile
X1:          0.
X2:          1.0e-1
NX2:         40
EPS:         1.e-8
H1:          1.e-12
HMIN:        1.e-18
Tstart:      0.
SigmaG:     10.
DeltaG:      0.01
Lambda:     20.
mGal:        1.
Rcutof:    100.
Rcut2:     100.
IDUM:       -1
size:      100.
Icube:      -50. -50. -50.
             50.   0.   0.
              0.  50.   0.
              0.   0.  50.
NGAL:     1000
icVal:       0
PotNo1:      0.
wall:        0.
fila:        0.
node:        0.
PotNo5:      0.
b^2#1        0.0
b^2#2        0.0001
b^2#3        1.0
b^2#4        1.0
b^2#5        0.
canal:      10
```

A.3 Processing the Velocity Distribution

To create the velocity distribution plots in time, the multichannel-discretised data first had to be brought to a common velocity-scale, then it had to be processed for output. The interpolation of the data to a common axis has been done by a FORTRAN program. The processing and output of the data has been done by means of an interacting data language. In the following, both codes for the purpose of verifiability are presented:

```
      program vscal

*     reads from <ifile> the filename of a 10 channel sampled velocity
*     distribution over 40 timesteps and converts the file
*     to equal channel calibration to prepare output by IDL
*
      implicit logical(A-Z)

      Real V(400),DV(400),T(400),eps
      Real Vsc(10),DVsc(400),VscMax,VscMin
      Character*12 fname
      Character*14 ofname
      Integer i,j,k,index,arg,argi,argk

      open(UNIT=1,File= 'ifile' ,Err=13,STATUS='OLD')
      Read(1,*) fname
      goto 14
13    Pause ' File ifile not found'
14    Continue

      ofname = fname(6: )
      Write(*,*)'Convert velocity scale from '//fname
      open(UNIT=2,File= fname ,Err=15,STATUS='OLD')
      GO TO 16
15    Pause 'Error while opening parameterfile'
16    Continue

      Do 50 i= 1,400
      Read(2,*) V(i),DV(i),T(i)
D     Print*, V(i),DV(i),T(i)
50    Continue
      close(UNIT=1)
      Close(Unit=2)

      VscMin = 1.e9
      VscMax = 0.
      Do 500 k=1,400
        If (VscMin.GT.V(k)) VscMin = V(k)
        If (VscMax.LT.V(k)) VscMax = V(k)
500   Continue

      Do 550 j=1,10              ! for all times equal
        Vsc(j) = (VscMax-VscMin)/10.*real(j) +VscMin
550   Continue

      Do 1000 j=1,10             ! all channels
      Do  800 i=1,40             ! all times
         arg = 10*(i-1)+j
*        find the index for which ABS(Vsc(j)-V(argk)) becomes minimal

         eps = VscMax
         index = 0
         Do 600 k= 1,10
           argk = 10*(i-1)+k
           If (ABS(Vsc(j)-V(argk)).LT.eps) then
            eps = ABS(Vsc(j)-V(argk))
            index = k
           Endif
           If (index.EQ.0) pause 'Fehler'
600      Continue

         argi= 10*(i-1)+index
         DVsc(arg)=DV(argi)

800   Continue
1000  Continue

      print*,'Write scaled data to :', ofname
      open(UNIT=1,File=ofname)
      Do 2000 i=1,40
      Do 1800 j=1,10
```



```
         arg = 10*(i-1)+j
         Write(1,'(3(G13.3))') Vsc(j),DVsc(arg),T(arg)
1800  Continue
2000  Continue
      close(UNIT=1)

      END
```

```
; Makro fuer Geschwindigkeitverteilung

titstr='!17 Wall'
xaxstr='!17              time'
yaxstr='!17velocity'
y_max=500

A = fltarr(3,400) ; Einlesevariale
Z = fltarr(40,10) ; 2-D Verteilung
X = fltarr(40)
Y = fltarr(10)

openr,1,'w4Bm'
readf,1,A
close, 1

A = transpose(A)
ZR = A(*,1)  ; Verteilung dN/N
YR = A(*,0)  ; Geschwindigkeit
XR = A(*,2)  ; Zeit

; print, XR(0),YR(0),ZR(0)

for j= 0, 9  do begin
for i= 0, 39 do begin
index  = i*10 +j
Z(i,j) = ZR(index)
X(i)   = XR(i*10)
endfor
Y(j)   = YR(j+390) ; falsch
endfor
;                smooth 2 times:
ZS=smooth(Z ,3)
ZS=smooth(ZS,3)
data= replicate(-1.,42,12)
data(1,1)=ZS
xd=replicate(0.,42)
xd(41)=41.
xd(1)=X
yd=replicate(-1.,12)
yd(11)=510. ;      larger than any velocity
yd(1)=Y

clev=[0,30,60,90,120,150,180,210,240,270]
clab=[0,1,0,1,0,1,0,1,0,1]
!P.CHARSIZE  =1.25
; loadct, 0
cin =[240,112,128,144,160,176,192,208,224,240,240]

contour, LEVELS=clev, C_LABELS=clab, PATH_FILENAME='cpaths.dat', data, xd,yd, xrange=[1,40
], xstyle=1, yrange=[1,y_max], ystyle=1
print, 'Plot auf File ist fertig !'

;!P.BACKGROUND=255
;set_plot,'ps' ; Ausdruck zu postscript file
window
polycontour, 'cpaths.dat', color_index=cin
contour, LEVELS=clev,C_LABEL=clab,/NOERASE, data, xd,yd, xrange=[1,40], xstyle=1, yrange=[
1,y_max], ystyle=1

;device, /close
;spawn, 'lpr idl.ps'
;set_plot,'x'
;                    Ausdruck der Konturen alleine:
;set_plot,'ps' ; Ausdruck zu postscript file
;window
;contour, xtitle=xaxstr,ytitle=yaxstr,title=titstr,LEVELS=clev,C_LABEL=clab, data, xd,yd,x
range=[1,40], xstyle=1, yrange=[1,y_max], ystyle=1

;device, /close
;spawn, 'lpr idl.ps'
```



```
;set_plot,'x'
print, 'Alles Fertig !'

END
```

Appendix B

Tests of the N-body Code

B.1 Test of the Algorithms Accuracy

The first test presented concerns the question posed within the 10 particle experiments whether the appearent scatter pattern in velocity space were due to bad determination of the particles trajectories. The two experiments performed thereto are shown in in Figs. A1a. and b. for a low-mass wall potential (1 pmu, 10 particles). Fig. (a) is calculated with the Bulirsch-Stoer method applied for each particle individually; Therefore only the individual timestep of the particle has been error controlled. Fig. (b) shows the same calculation with the Bulirsch-Stoer method applied to the sample as a whole, where the error control was applied in regard to the worst-offender member of the sample. This in turn has slowed down the computing-time considerabely. The particles have been started from identical initial locations (for the controlled randomizing, cf. preceding Section) and show exactly the same trajectories in location space. I therefore assumed for all following experiments the application of Bulirsch-Stoer error criterion to the global timestep as sufficient.

Figs. A1: Test versus results expected from a tree code (cf. text)

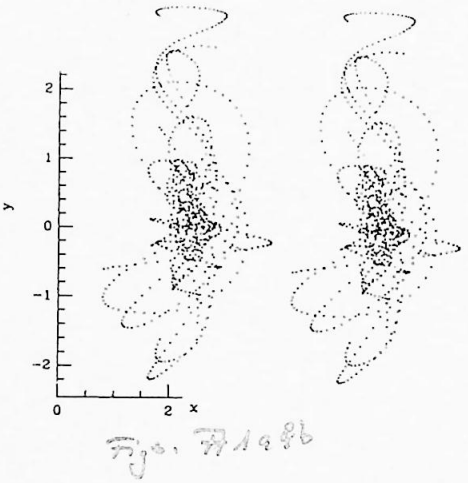

In the case of the application of the Bulirsch-Stoer error criterion to the worst-offender member of the sample, the algorithm has run with the same precision as a tree code in case of evaluating the particle interaction only all global time steps. The main difference to a tree code (for practical applications, the essential difference) is that a tree code would preselect all necessary calculations on the substep time-level (where the particles proceed fast in time) from the less necessary calculations (where the particles are almost static). This saves much computing time, but is still less fast than the application of the error criterion (which sets the substep-size) to the global timestep. Moreover, as it would be in principle possible but very time consuming within the actual strategie to apply the differential equation solver algorithm to each particle individually, within a tree code one could evaluate the interactions between the particles on the substep time level without running into arbitrary high total calculation times.

The result, that the trajectories are found to be equally well calculated as in case of applying the error criterion to the worst offender member of the sample of particles, exactly only holds for comparatively [1] low density particle flow. Moreover the question arises whether the estimate of the algorithm accuracy in determining the trajectories of the particles (solving the ordinary linear differential equations) which sets the substep-size does work well or whether the estimator to set the substep-size has set the substep partitioning same for both experiments.

[1] In comparison to high-density regions near potentials for large samples of particles or strongly attracting potentials, as in the case of the "high-attracting" experiments.

B.2 Algorithm-Effort Investigations for a Non-Softened Wall Potential

While softening the particle potentials, the algorithm showed difficulties in calculating the trajectories for a wall potential. Therefore it has been assumed that the non-smoothness of the wall potential at $x = 0$ may cause problems. This could be proven by comparing the algorithm effort indicated by the number of successive substeps (NOK) and the number of misguided substeps (NBAD) which was listed during this test: The Fig. A2a shows the breakdown of the algorithm while calculating the 15th global timestep for a sample of 100 particles. Both (NOK and NBAD) control variables scatter to values ~ 1000. Then the algorithm has stopped with the message: "step size smaller than minimum" (alternatively: "too many substeps", depending on HMIN). This is to be compared with the effort for the calculation in a smoothed wall potential shown in Fig. A2b: The number of sucessful steps slightly varies, indicating the actual effort to calculate the trajectories. Only a few times, a small amount of "bad steps" has to be accepted [2].

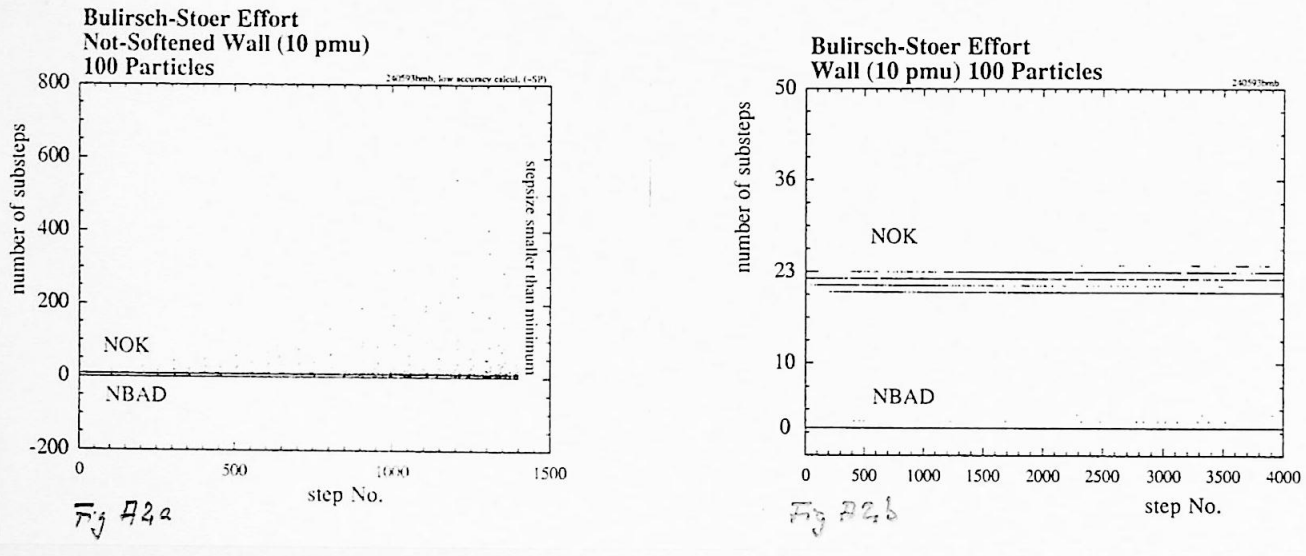

Figs. A2: Algoritm Effort for a Wall

[2]Those "bad steps" affect only the time which is necessary to do the calculations. For the corresponding computed results are thrown away by the algorithm, they do not affect the overall accuracy.

B.3 Collapse Experiments

Since momentum creation appears strongest for direct encounters whereas in a large sample of particles only few close encounters are attained, experiments to distinguish close fast encounters from far gravitational interaction have been disposed and carried out. To see the effects of close and fast interactions, particles were studied in direct collision in the so-called *Linear Collapse Experiments.* To study the effect of long-range interaction and comparatively slow approximations, particles were studied while giving them initial angular momentum to prevent fast approach in the so called *Circular Collapse Experiments.*

Imagine six particles placed on equal distances (1 dimensionless length unit) to the center, on a ring, forming a hexagon. With initially zero velocity (Linear Collision, Figs. A3 with dissipation, A4 without dissipation) the particles have been observed to escape very far (Fig. A4a.). Including dynamical friction the particles get stopped and return, but momentum creation still occurs (Figs. A3.). These experiments therefore have shown that dissipational loss of energy can be compensated by momentum creation effects. The corresponding diagrams in location-velocity space (Figs. A3b., A4b.) illustrate again the trajectories in the two different cases (with and without dissipation).

In the experiments with an initial velocity given to the particles less than the velocity to hold them in (unstable) mechanical equilibrium on a circle (Circular Collapse, Figs. A5 with dissipation, A6 without dissipation), a paradox effect occurs: Whereas the purely selfgravitating ring of particles first slightly collapses, then reexpands to some too large (for energy conservation) but still modest radius conserving angular momentum (Fig. A7b.), the ring of particles with dissipation collapses faster, then reexpands again to half its initial radius. The trajectories thereby form the flower-like pattern shown in Fig. A5a. In similar experiments with shorter softening lengths the reexpansion has been found even larger than the initial radius and even larger than the reexpansion found in the correponding case without dissipation (Figs. not shown here); Dissipation can lead to an energy gain due to momentum creation ! However, for the softening length in use ($b = 1$), the momentum gain still is modest. The particles recollapsed and in the following formed the pattern in the center of Fig. A5a. Again, the trajectories shown in location-velocity space (Figs. A5b. and A6b.) illustrate the trajectories for the two different cases.

The corresponding energy and momentum diagrams of the experiments (Figs. A7 to A10) show the creation of momentum respectively energy wich is suppressed by dissipation.

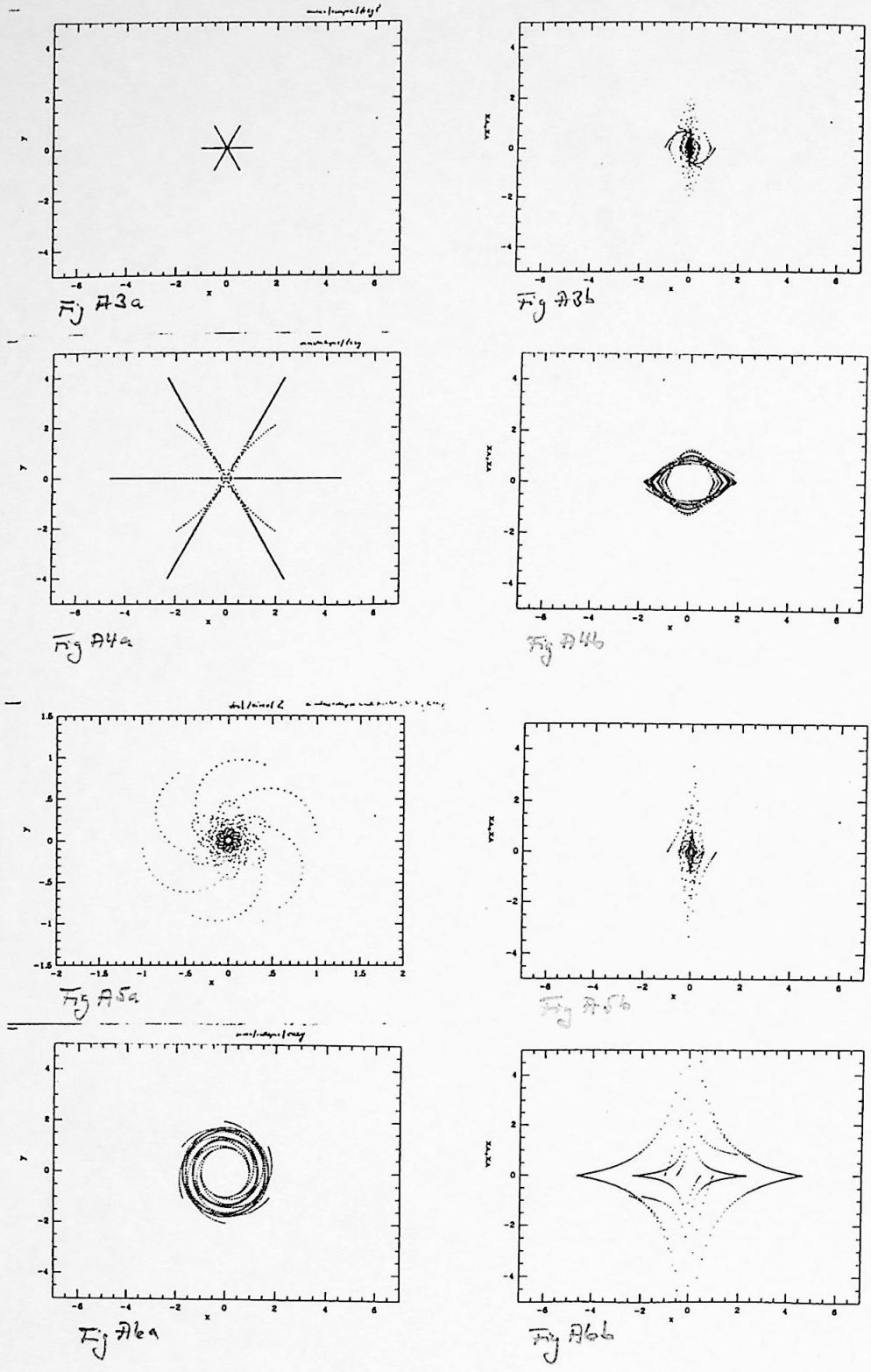

Fig. A3 to A6: Location space (to the left) and phase space diagrams (to the right) for "Collision Experiments" with and without dissipation.

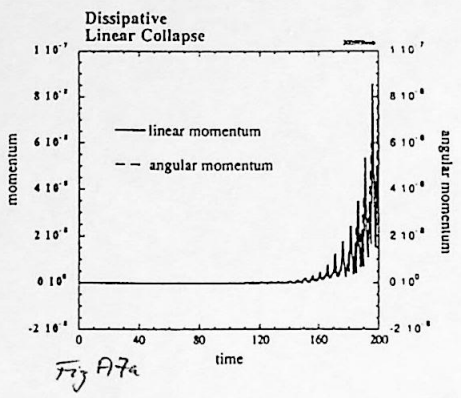

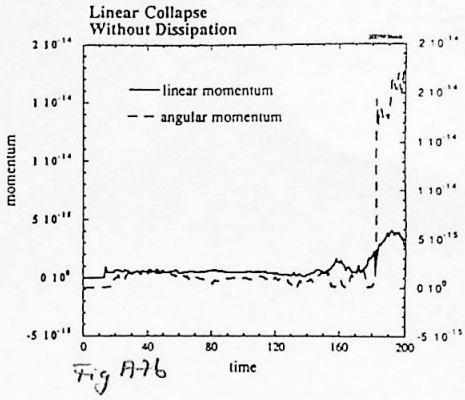

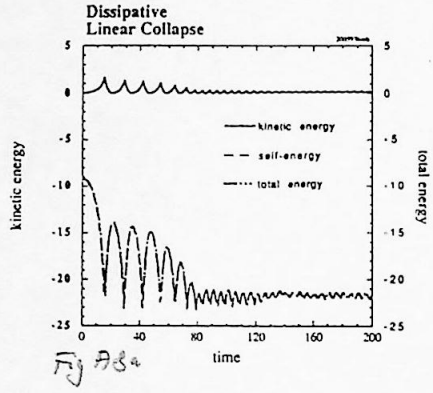

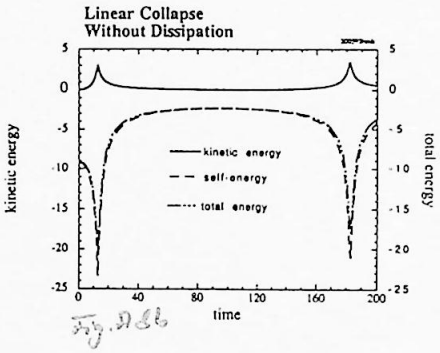

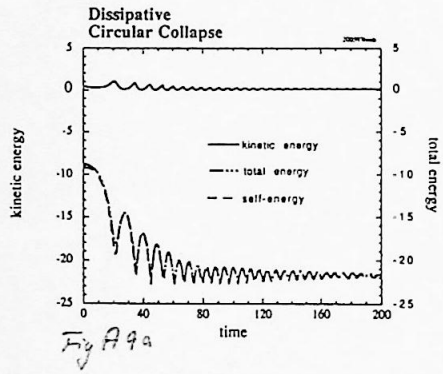

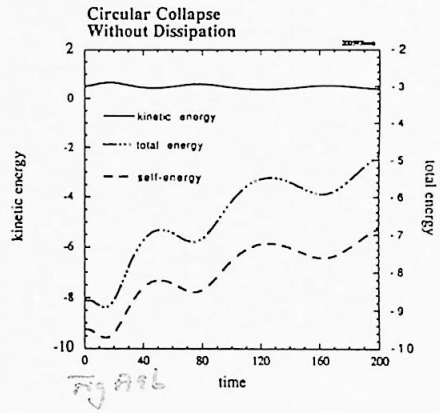

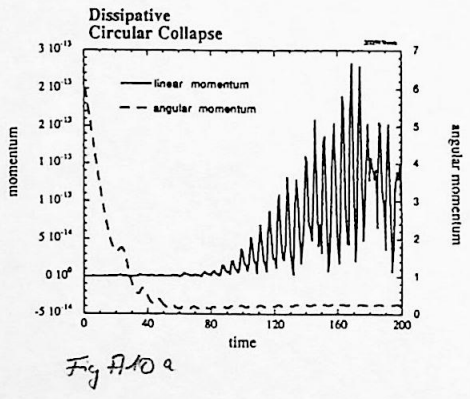

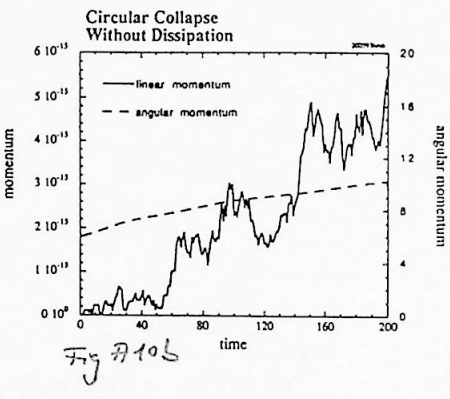

Fig. A3 to A6: Corresponding momentum (top and bottom) and energy (two rows in the center) diagrams for "Collision Experiments" with (to the left) and without (to the right) dissipation.

B.4 Planet Experiments

This experiment to test the algorithm far from singular situations (where the forces, without softening, would increase to infinity) reminders on the keplerian problem: One mass has been placed in the center (the potential of a node) and two partices have been started from $x = 1$ and $x = 0.5$ ($y = 0$) to turn around on different orbits. The potential strength has been set to the strength of 16 particles (16 pmu) to make the different effects of dynamical friction and gravitation visible. The result, as it can be seen from the trajectories in location space (Figs. A11 to A13), is as follows: Without friction, the inner planet gives a part of its energy to the outer one which orbit thereby becomes more and more elliptical (Fig. A12). Including friction, (Fig. A13); the inner planet thereby settles into a lower orbit. Both planets decrease their potential energy in respect to the motion following pure selfgravitation. The experiment also has been performed neglecting the selfgravitation acting between the two planets (Fig. A11).

On this problem, for the first time within this work a study on the energy and momentum has been made (Figs. A14 to A16): In the case of dynamical friction (Fig. A16a.), the self-energy of the system decreases, whereas the kinetic energy of the single planets slightly increases. This, according to the virial theorem 3.40, is consistent with keplerian motion, including adiabatic decrease of potential energy [3].

Most interesting for the purpose of the many particle experiments performed, from the momentum diagrams can be concluded (Fig. A15b.) that momentum creation occurs even in the case of far gravitational interaction (no need for close encounter of the particles).

[3] "A satellite becoming faster while getting decelerated."

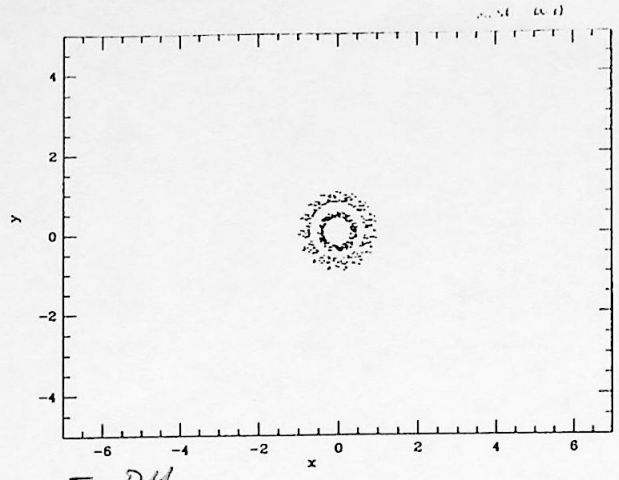

Fig A11

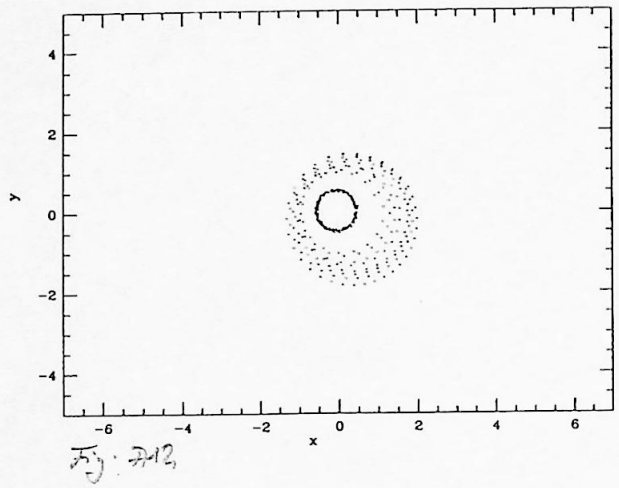

Fig. A12

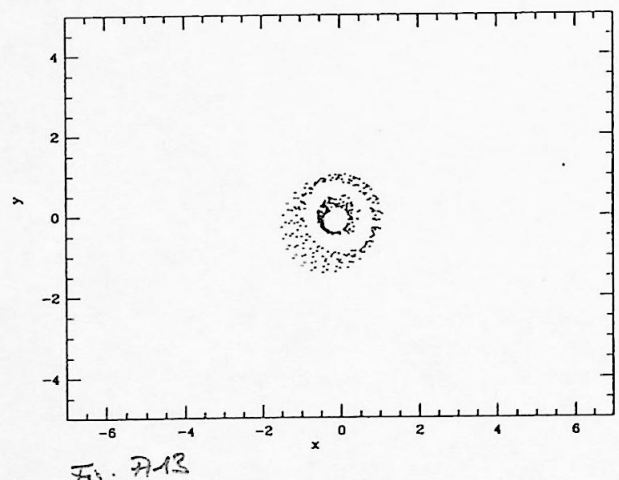

Fig. A13

Figs. A11 to A13: Trajectories in location space for the planet experiments with dynamical friction only (top), selfgravitation only (center) and selfgravitation including dynamical friction (bottom).

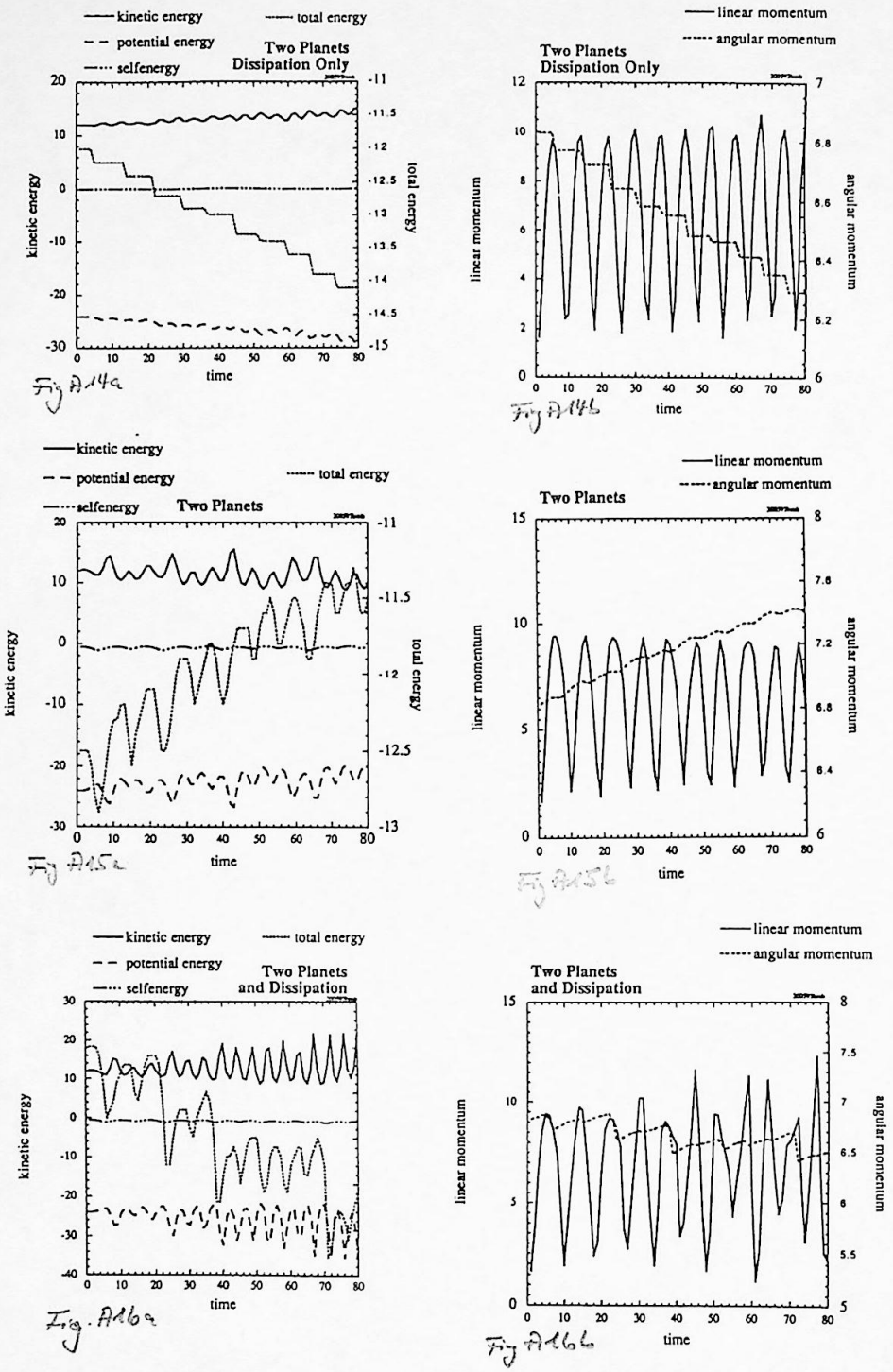

Figs. A14 to A16: Energy (to the left) and momentum (to the right) diagrams for the planet experiments with dynamical friction only (top), selfgravitation only (center) and selfgravitation including dynamical friction (bottom).

Appendix C

Modelling Filament Potentials

C.1 Modelling Filament Potentials

In a first approach, I have tried to develop the potential of filaments in Taylor series (Fig. A17). Those can be analytically transformed into Fourier space. However, even taking 12th order Fourier sums, the result not has been convincing: The retransformed functions did not end oscillating in the cube and were 5 magnitudes too high. The reason therefore is the bad convergence of the Fourier series via the logarithm. I have calculated in 5th. order in the Taylor serie and 12th. order in the Fourier series (Fig. A18). It cannot be expected that increasing order does change much of the result.

Afterwards, I have calculated the Fourier coefficients of the logarithm to higher order (up to 128) numerically. The results are shown in Figs. A19. The shape of the spectrum does not depend on the number of coefficients (Figs. A19b. and c.), but a reasonable approach of the logarithm has first been attained while using 128 coefficients (Fig. A19). Note that, in the case of the 12 coefficients used in Fig. A18, the Fourier sum at least should somehow represent the Taylor approximation shown in Fig. A17 (but it does not).

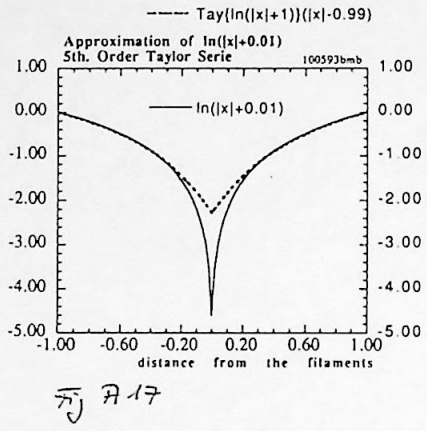

Fig A17

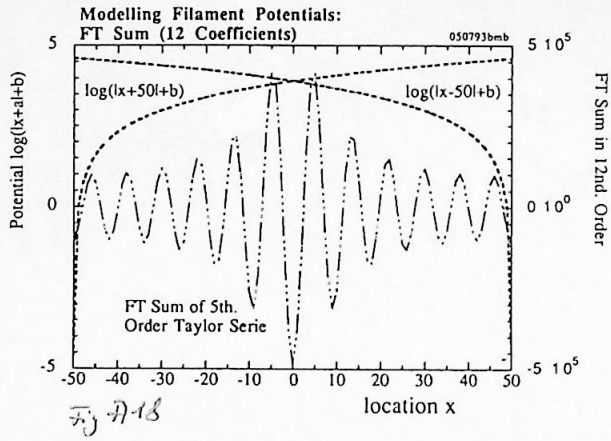

Fig A18

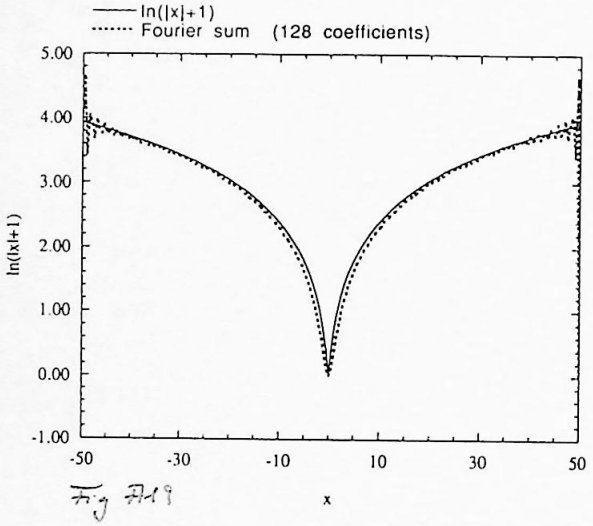

Fig A19

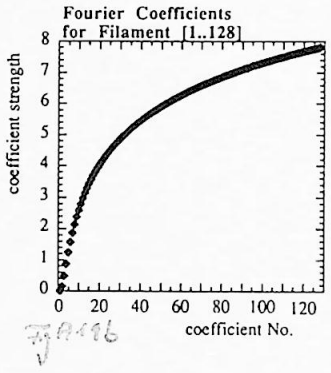

Fig A19b

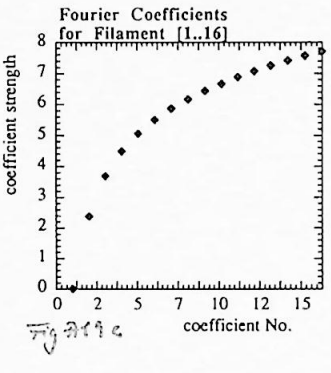

Fig A19c

Figs. A17 to A19: Miscellaneous approximations and calculations in Fourier space.

C.2 Numerical Fourier Analysis

In this Section, the formulae for calculating the Fourier coefficients for filaments as edges of a periodical cube structure of spatial period $2\,\ell$ are presented.

The filaments will be modelled by a superposition of softened potentials of infinite lines of equal homogeneous mass density along the edges of the cubes:

$$\Phi_f(\mathbf{x}) = \Phi_1(x_1) + \Phi_2(x_2) + \Phi_3(x_3) \tag{C.1}$$

where

$$\Phi_1(x_1) = \frac{G\Xi}{2\,\pi} \ln \sqrt{x_1^2 + b^2} \tag{C.2}$$

$$\Phi_2(x_2) = \frac{G\Xi}{2\,\pi} \ln \sqrt{x_2^2 + b^2} \tag{C.3}$$

$$\Phi_3(x_3) = \frac{G\Xi}{2\,\pi} \ln \sqrt{x_3^2 + b^2} \tag{C.4}$$

with the gravitational constant G, the line mass density Ξ and the softening length b. We suppose that the origin $(0, 0, 0)$ lies in the vertices of the periodic structure.

The dependency of the potentials $\Phi_{i=1\ldots3}$ only on one coordinate allows to do the Fourier transform for each direction separately. Periodicity is obtained by approximating Φ_f by the n'th partial sum $\Phi_f^{(n)}(x)$ of its Fourier serie. For we demand symmetry $\Phi(x) = \Phi(-x)$ this is

$$\Phi_f^{(n)}(x) = \frac{a_0}{2} + \sum_{k=1}^{n} a_k \cos \frac{k\pi x}{\ell} \tag{C.5}$$

with the Fourier coefficients

$$a_k = \frac{2}{\ell} \int_0^{\ell} \Phi_f(x) \cos \frac{k\pi x}{\ell} \mathrm{d}x \tag{C.6}$$

For convenience we have dropped the subscripts $i = 1\ldots3$ at x. We can calculate Eq. C.5 by the numerical approximation

$$\tilde{\Phi}_f^{(n)} = \frac{\tilde{a}_0}{2} + \sum_{k=1}^{N-1} \tilde{a}_k \cos \frac{k\pi x}{\ell} \tag{C.7}$$

with the coefficients

$$\tilde{a}_k = \frac{2}{N} \sum_{\mu=0}^{N-1} \Phi_\mu \cos \frac{\mu\pi k}{N} \tag{C.8}$$

evaluated at

$$\Phi_\mu = \Phi_f(x_\mu), \quad x_\mu = \mu \times \ell/N, \quad \mu = 1\ldots N-1 \tag{C.9}$$

Appendix D

The Two-Point Correlation Function

The two-point corralation function is, apart from the velocity fields, another important tool actually used to describe the distributions of galaxies on large scales. In principle it is easily to calculate for the numerical data which has been obtained. Because the limited time for this stage did not allow to do so, I would like to propose the method here in the Appendix:

The two-point correlation function $\xi(r)$ (cf. e.g. [Com91]) is defined to measure the deviation of the probability to find two particles in a volume V located at R and r from a Poisson distribution

$$\xi(r) \equiv \bar{n}^{-2} \langle n(\mathbf{R}+\mathbf{r}) n(\mathbf{R}) \rangle_{\mathbf{R} \in V} - 1 \tag{D.1}$$

where $\bar{n}$ denotes the mean density of particles and $\langle \ldots \rangle_{\mathbf{R} \in V}$ denotes the autocorrelation of the density distribution.

With $\xi(r)$ defined by D.1 we can write the probability

$$dP = \left(\frac{\bar{n}}{N}\right)^2 \langle n(\mathbf{R}+\mathbf{r}) n(\mathbf{R}) \rangle_{\mathbf{R} \in V} dV_1 dV_2 \tag{D.2}$$

to find two particles in the volumes dV_1 and dV_2 respectively, given by the autocorrelation of the density distribution and proportional to the volumes dV_1 and dV_2, as

$$dP = \left(\frac{\bar{n}}{N}\right)^2 (1 + \xi(r))_{\mathbf{R} \in V} dV_1 dV_2 \tag{D.3}$$

what alternatively to Eq. D.1 can be used to define $\xi(r)$. The factor $(\bar{n}/N)^2$ gives the correct normalization $P = 1$.

We can calculate $\xi(r)$ for the distribution of particles in the potentials of wall, filament and node numerically along the radial direction within a sphere $\{r : r \leq r_N\}$ by

$$\tilde{\xi}(r) = -1 + \frac{9}{32\,\pi}\,\frac{V^2}{N^2}\sum_{i=1}^{J-1}\frac{N(r_i, r_{i+1})}{r_{i+1}^2 - r_i^{\,2}}\,\frac{N(r + r_i, r + r_{i+1})}{(r + r_{i+1})^2 - (r + r_i)^2}\,(r_{i+1} + r_i) \quad \text{(D.4)}$$

evaluated at $r = r_1 \ldots J - 1$, where $N(r_i, r_{i+1})$ denotes the number of particles in between (r_i, r_{i+1}), N denotes the total number of particles and V denotes the volume of the sphere. We therefore use the separation

$$\{r_i : r_i = i \times \ell/J \mid i = 1 \ldots J - 1\} \quad \text{(D.5)}$$

where $2\,\ell$ is the size of the large scale structure.

We expect the error Err in evaluating ξ in the numerical model as long as the distribution does not differ to much from Poissonian ($\xi \ll 1$) as inversely proportional to the square root of the number of particles N found in a volume element dV:

$$\text{Err} \propto \frac{1}{\sqrt{N}} \quad \text{(D.6)}$$

On the other side, the accuracy Acc in determining ξ increases proportional to the square-root of the number of volume elements, hence:

$$\text{Acc} \propto \frac{1}{\sqrt{N}} \quad \text{(D.7)}$$

Therefore the accuracy in total Acc/Err is independent from the choice of the separation. We choose the equidistant separation D.5 to obtain uniform resolution.

Bibliography

[Aar62] Aarseth, S.J. , Mon. Not. R. astr. Soc. (1962) **126** 223-255

[Abe58] Abell, G.O. , Ap. J. Sup. , (1958), **3**, 211-288

[Bah88] Bahcall, N.A. , Ann. Rev. Astron. Astrophys. (1988) **26**, 631-686

[Ben92] Bennett, C.L. , Boggess, N.W. , Cheng, E.S. , Hauser, M.G. , Mather, J.C. , Smoot, G.F. , Wright, E.L. (1992) in *The Third Teton Summer School: The Evolution of Galaxies and Their Environment*, Thronson, H.A. & Shull, J.M. (Eds.), COBE Preprint

[Bha88] Bhavsar, S.P. & Ling , E.N. , The Astrophysical Journal, (1988) **331**, 63-68

[Bin87] Binney, J. & Tremaine, S. (1987) *Galactic Dynamics*, Princeton UP

[Com91] Combes, F. , Boissé, P. , Mazure, A. , Blanchard, A. , (1991) *Galaxies et cosmologie* InterEditions, Paris

[Dam90] Damour, T. (1990), in *New and Excotic Phenomena '90*, Proc. 25. Rencontre de Moriond, Fackler, O. & Tran Tan Van, J. (Eds.), Les Arcs (1990) pp. 285-290

[Egg62] Eggen, O.J. , Lynden-Bell, D. , Sandage, A.R. , The Astrophysical Journal, (1962) **136**, 748-766

[Gel89] Geller, M.J. & Huchra, J.P. , Science (1989) **246**, 897-903

[Gol87] Goldstein, H. (1987) *Klassische Mechanik*, AULA, Wiesbaden

[Hon90] Honerkamp, J. (1990) *Stochastische Dynamische Systeme*, VCH, Basel

[Huc83] Huchra, J. , Davis, M. , Latham, D. , Tonry, J. , Astrophys. J. Suppl. (1983) **52**, 89-119

[Ick84] Icke, V. , Mon. Not. R. astr. Soc. (1984) **206**, 1P-3P

[Ick91] Icke, V. & van de Weygaert, R. , Q. Jl. R. ast. Soc. (1991) **32**, 85-112

[Ick91b] Icke, V. (1991) in *Second European Conference on Astroparticle Physics*, Bosseti, P. (Ed.) Aachen

[Kel29] Kellog, O.D. (1929) *Foundations of Potential Theory*, Dover Public. Inc. New York

[Lac90] Lacoste, B. , *Europe: Stepping Stones To Space*, (1990) Bedforshire, UK

[Oor83] Oort, J.H. , Ann. Rev. Astron. Astrophys. (1983) **21**, 373-428

[Ost75] Ostriker, J.P. & Thuan, T.X. , The Astrophysical Journal, (1975) **202**, 353-364

[Ost88] Ostriker, J.P. & McKee, C.F. , Rev. of Modern Physics (1988) **60**, 1-68

[Pee80] Peebles, P.J.E. , *The Large-Scale Structure of the Universe*, (1980) Princeton UP

[Pre86] Press, W.H. , Flannery, B.P. , Teukolsky, S.A. , Veterling, W.T. (1986) *Numerical Recipes*, Cambridge UP

[Roo88] Rood, H.J. , Ann. Rev. of Astron. Astrophys. (1988) **26**, 245-294

[Sel87] Sellwood, J.A. , Ann. Rev. Astron. Astrophys. (1987) **25**, 151-186

[Sha89] Shandarin, S.F. & Zel'dovich, Ya.B. , Rev. of Modern Physics (1989) **61**, 185-220

[Thu75] Thuan, T.X. , Hart, M.H. , Ostriker, J.P. , The Astrophysical Journal, (1975) **201**, 756-772

[Tre84] Tremaine, S. & Weinberg, M.D. , Mon. Not. R. astr. Soc. (1984) **209**, 729-757

[Wey89] van de Weygaert, R. & Icke, V. , Astron. Astrophys. (1989) **213**, 1-9